Mohsen A. Irandoust[1,2*], Keith Priestley[2], Farhad Sobouti[1]

[1]Department of Earth Sciences, Institute for Advanced Studies in Basic Sciences (IASBS), Zanjan 45137-66731, Iran.

[2]Bullard Laboratories, University of Cambridge, Cambridge, U.K.

Corresponding author: Mohsen A. Irandoust (mai.gph@gmail.com)

Key Points:

- Inversion of Rayleigh wave dispersion and *P* receiver function data result in a shear-wave velocity model for the lithosphere of the Iranian Plateau.
- Thickest crust (>55 km) occurs below the collisional belts; regions of low deformation, or active subduction have thinner crust (<45 km).
- The crustal model reveals a low-velocity feature beneath the Zagros and central Iran indicating the Arabian crust underthrusts central Iran.

Abstract

From a joint analysis of fundamental mode Rayleigh wave group velocities and *P*-wave receiver functions, we derive a new, high-resolution 3D shear-wave velocity (*Vs*) model for the crust and uppermost mantle of the Iranian Plateau. The thickest crust (>55km) is located beneath the deforming belts of the Plateau (e.g., the Sanandaj-Sirjan Zone (SSZ) and Talesh-Alborz-Binalud Mountains), whereas regions of lower topography/deformation (e.g., central Iran and the Lut Block), and the regions of very younger deformation such as the Makran Accretionary Wedge and the Zagros Simply Folded Belt (SFB) have a thinner (<45km) crust. Our model reveals a low-*Vs* tongue-shaped feature, indicating the underthrusting of the Arabian crust beneath central Iran. In the central Zagros, underthrusting of the Arabian crust is steeper, resulting in a narrower (~150km) deforming zone with thicker (~60-65km) crust compared to the crust beneath the broader (~250km) deforming zone and somewhat thinner (~55-60km) crust below the Lorestan Arc. Regions of low-*Vs* in the upper crust correspond to regions of thick sediments (e.g., the South Caspian Basin, the SFB and foreland basin of the Zagros, and the Makran Subduction Wedge). The subcrustal Rayleigh wave azimuthal anisotropy of the Plateau shows a rather uniform and smoothly-varying pattern. In the NW Zagros the crustal and subcrustal pattern of anisotropy agrees with that previously estimated from the shear-wave core phases, implying that the whole lithosphere deforms coherently, but for other regions (e.g., the western Alborz and Kopet Dag), the anisotropic pattern does not support a coherent deformational fabric throughout the lithosphere.

Plain Language Summary

We use joint analyses of surface and body wave seismic data to investigate the crustal and uppermost mantle wave-speed structure of the Iranian Plateau, the region of relatively rapid deformation and high-topography resulting from

the collision of the Arabian and Eurasian Plates. The variations in the wave-speed and thickness of our crustal model reflect the main geological and physical features of the crust. In general, thicker crust (>55km) underlies the elevated, deforming zones (e.g., the Sanandaj-Sirjan Zone and the Talesh-Alborz-Binalud Mountains), while thinner crust (<45km) occurs under the lower elevation, more stable regions of the Plateau (e.g., central Iran and the Lut Block). In the Zagros region, our model reveals a low shear wave-speed, tongue-shaped feature extending beneath the central Plateau, indicating the underthrusting of the Arabian crust. The low wave-speed regions in the shallow crust correspond to the thick (~10-20km) sedimentary cover (e.g., the South Caspian Basin, the Simply Folded Belt and foreland basin of the Zagros Mountains, and the Makran Subduction).

1 Introduction

The Iranian Plateau, a broad zone of continental deformation, has formed as a result of the Arabia-Eurasia collision which initiated about 25 million years ago (e.g., Hatzfeld & Molnar, 2010; Agard et al., 2011). It is the site of one of the youngest collision zones in the world and the study of its structure can provide clues to understanding the younger stages of continental collision and plateau growth. The evolution of the Plateau is intimately associated with the opening and closing of the Paleo-Tethys and Neo-Tethys Oceans. Following the closure of the Paleo-Tethys in the Triassic (e.g., Stöklin 1974a; Berberian, 1981; Şengör et al., 1984), the landmass of the Iranian Plateau began to form with the coalescing of island arcs and dispersed continental fragments which had rifted from the northern margin of Gondwana during the Permian. These fragments accreted to the Turan Platform, the southern margin of Eurasia at that time (e.g., McElhinny et al., 1981; Besse et al., 1998). The initiation of subduction of the Neo-Tethys Ocean is a subject of debate as to whether it occurred in the Late Triassic or Late Jurassic (e.g., Berberian, 1981; Mohajjel et al., 2003; Arvin et al., 2007). The Arabian Plate was part of the Nubian Shield until 30–35 Ma when it began to rift from Africa (e.g., Martinez & Cochran, 1988; Omar & Steckler, 1995; Cochran, 2005). The closing of the northern portion of the Neo-Tethys Ocean and the collision of Arabia and Eurasia began in the early Miocene (various estimates between 16 and 27 Ma) (e.g., Robertson, 2000; Horton et al., 2008; Ballato et al., 2011; McQuarrie & van Hinsbergen, 2013; Pirouz et al., 2017). The last remnant of the Neo-Tethys is now subducting beneath the Makran Subduction Zone of southeastern Iran and southwestern Pakistan. The subsequent northward motion of the Arabian Plate following the final closure of the Neo-Tethys gave rise to the Zagros Mountains and the 1-2 km-high Iranian Plateau northeast of the Bitlis-Zagros Suture (see Agard et al., 2011 for a review) (Fig. 1). The ongoing convergence between Arabia and Eurasia is now accommodated by distributed shortening within the Zagros Mountains and the northern and eastern margins of the Iranian Plateau and the southern Caspian Sea.

The geometry and deformation of orogenic belts are often influenced by the

presence of rigid blocks within and around them. The Iranian Plateau contains, and is surrounded by, several such rigid blocks – the Arabian Plate (e.g., Sandvol et al., 1998; Gök et al., 2008), the South Caspian Basin (SCB) (e.g., Priestley et al., 1994; Jackson et al., 2002), the Great Kavir (e.g., Jackson & McKenzie, 1984; Jackson & McKenzie, 1988), the Lut Block (e.g., Jackson & McKenzie, 1984; Eshagh et al., 2020), the Turan Platform (e.g., Lyberis et al., 1998; Entezar-Saadat et al., 2017), and the Helmand Block (e.g., Jackson & McKenzie, 1984; Eshagh et al., 2020). These regions are separated by compressive orogenic belts – the Zagros, Talesh, Alborz , Kopet Dag Mountains, and the Sistan Suture Zone. The overall motion between these tectonic entities is known from global plate studies (e.g., DeMets et al., 1990; McQuarrie et al., 2003), space-based geodesy (e.g., Vernant et al., 2004a; Khorrami et al., 2019), and seismicity (e.g., Jackson & McKenzie, 1988; Engdahl et al., 2006). Iran has a long, well-documented earthquake history, (e.g., Ambraseys & Melville, 2005) and Jackson and McKenzie (1988) and Masson et al. (2005) concluded that earthquakes account for most of the shortening on the northern and eastern margins of the Iranian Plateau, but that aseismic creep is the dominant process responsible for shortening in the Zagros Mountains to the southwest.

Given the diverse features and tectonic history of the Iranian Plateau, it is not surprising that its crust and uppermost mantle have a variety of complex characteristics. In this paper, we present a structural model for the crust and uppermost mantle shear-wave velocity (V_s) and seismic anisotropy of the Plateau that is derived from large data sets of P receiver function and surface wave dispersion. In Section 2, we briefly summarize the active tectonics of the Plateau; in Section 3 we discuss the data and analysis techniques upon which the crust and uppermost mantle model is constructed; in Section 4 we describe the results of our model; and in Section 5 we discuss the significance of our crust and uppermost mantle model in terms of the tectonics of the Plateau. We address important questions as to whether or not shortening in the basement is accommodated, at least partially, by distributed thrusts as suggested by fault plane solutions (e.g., Talebian & Jackson, 2004; Tatar et al., 2004; Hollingsworth et al., 2010a), whether or not the deformation in the lower crust is continuous or localized (Jackson & Fitch, 1981), the geometry of the crustal underthrusting of the Arabian Plate beneath central Iran and its variation along the Zagros collision zone, and how anisotropy reflects the lithospheric deformation of the Iranian Plateau.

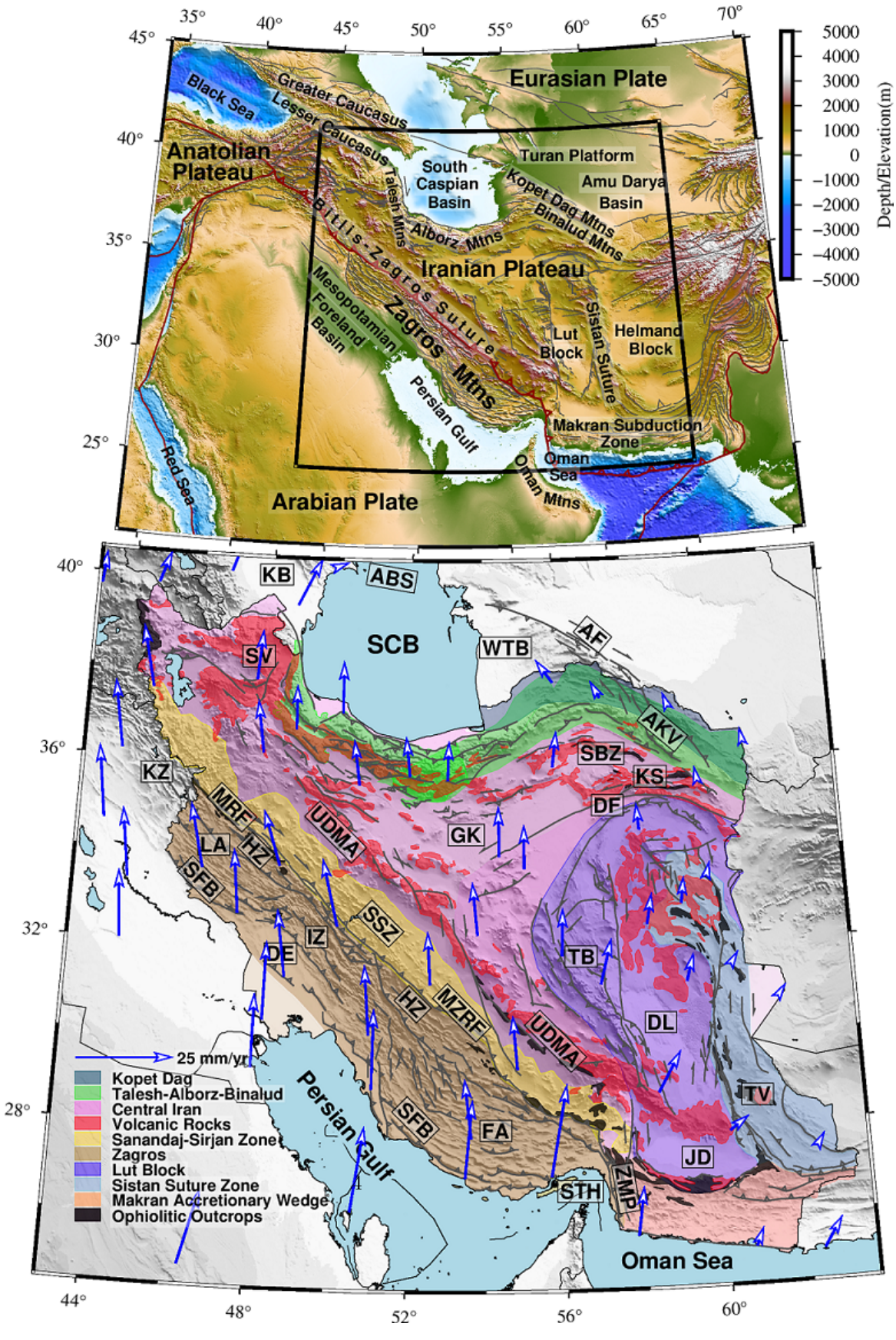
Eurasian Plate
Black Sea
Greater Caucasus
Lesser Caucasus
Anatolian Plateau
Turan Platform
South Caspian Basin
Amu Darya Basin
Kopet Dag Mtns
Binalud Mtns
Talesh Mtns
Alborz Mtns
Bitlis-Zagros Suture
Iranian Plateau
Mesopotamian Foreland Basin
Zagros Mtns
Sistan Suture
Lut Block
Helmand Block
Persian Gulf
Makran Subduction Zone
Oman Sea
Red Sea
Oman Mtns
Arabian Plate
Depth/Elevation(m)
5000
4000
3000
2000
1000
0
−1000
−2000
−3000
−4000
−5000
SCB
KB
ABS
AF
WTB
SV
AKV
SBZ
KS
KZ
DF
MRF
UDMA
GK
LA
HZ
SFB
SSZ
IZ
DE
TB
MZRF
DL
TV
JD
FA
STH
ZMP
25 mm/yr
Kopet Dag
Talesh-Alborz-Binalud
Central Iran
Volcanic Rocks
Sanandaj-Sirjan Zone
Zagros
Lut Block
Sistan Suture Zone
Makran Accretionary Wedge
Ophiolitic Outcrops
Persian Gulf
Oman Sea
35°
40°
45°
50°
55°
60°
65°
70°
25°
30°
36°
28°
32°
44°
48°
52°
56°

Figure 1. Upper panel: The main tectonic elements of the Arabia-Eurasia collision zone. Lower panel: The main geological features of the Iranian Plateau (the black box in the upper panel). Solid lines represent the active faults (Hessami et al., 2003). GPS velocity vectors are from Khorrami et al. (2019). Abbreviations are: Fars Arc (FA), Lorestan Arc (LA), Izeh Zone (IZ), Kirkuk Zone (KZ), Dezful Embayment (DE), Simply Folded Belt (SFB), High Zagros Thrust Belt (HZ), Main Recent Fault (MRF), Main Zagros Reverse Fault (MZRF), Sanandaj-Sirjan Zone (SSZ), Urumieh-Dokhtar Magmatic Assemblage (UDMA), Strait of Hormuz (STH), Zendan–Minab–Palami Fault System (ZMP), Jazmurian Depression (JD), Taftan Volcano (TV), Dasht-e Lut (DL), Tabas Block (TB), Great Kavir (GK), Doruneh Fault (DF), Kuh-e Sorkh (KS), Sabzevar Mountains (SBZ), Atrak-Kashafrud Valley (AKV), Sabalan Volcano (SV), South Caspian Basin (SCB), Apsheron-Balkhan Sill (ABS), Kura Basin (KB), West Turkmenistan Basin (WTB), and Ashgabat Fault (AF).

2 Active tectonics of the Iranian Plateau

The northward motion of Arabia relative to Eurasia at a rate of 22 mm yr^{-1} (Vernant et al., 2004a; Reilinger et al., 2006) is primarily accommodated across the Iranian Plateau (Fig, 1). The deforming zone is bound in the west by the Zagros Mountains, in the east by the stable Helmand Block, in the north along a 2000 km-long belt following the Kopet Dag Mountains, the Apsheron-Balkhan Sill in the central Caspian Sea and the Greater Caucasus Mountains, and in the south by the Makran Subduction Zone. The bulk of the deforming region consists of the Iranian Plateau whose northern border is formed by the Talesh, Alborz and Kopet Dag Mountains in the north and northeast, and merges into the Anatolian Plateau in the northwest. The Plateau contains a number of deforming zones surrounded by aseismic blocks which limit lateral motion away from the collision zone. This limitation, and the rigid blocks embedded within the Plateau, result in different styles of deformation in various parts of the collision zone. Uplift and crustal thickening occur in the Zagros, Talesh-Alborz-Binalud and Kopet Dag Mountains; N-S right-lateral faulting takes place in central and eastern Iran; and subduction occurs beneath the Makran. West of 57° E, about half of the shortening is being accommodated by the Zagros Mountains (e.g., Tatar et al., 2002), with the Alborz Mountains and subduction in the central Caspian Sea accommodating the remainder (Priestley et al., 1994; Jackson et al., 2002). East of 57° E, subduction beneath the Makran accommodates about half of the northward motion of Arabia with the remainder accommodated in the mountain belts of the northeast part of the Plateau (e.g., Vernant et al., 2004b).

The Zagros Mountains represent the deforming southwestern edge of the Arabian Plateau. This fold-and-thrust belt is composed of a 150–250 km-wide series of ranges extending 1500 km from the eastern Anatolian Plateau to the Strait of Hormuz (Fig, 1). The Zagros consist of two parallel zones, the southwestern Simply Folded Belt (SFB) composed of large, open, linear folds where the sedimentary cover of the Arabian Plate has detached from the Precambrian

basement by the Hormuz salt (e.g., Falcon, 1961; Nissen et al., 2011), and the northeastern High Zagros Thrust Belt (Fig. 1) consisting of a highly-deformed terrain composed of a pile of thrust sheets containing imbricated slices of Mesozoic and Paleozoic sediments as well as ophiolites emplaced onto the Arabian passive margin during the late Cretaceous (Stoneley, 1990; Agard et al., 2011; Monsef et al., 2018). Traditionally, the Zagros Fold-and-Thrust-Belt (ZFTB) is divided into three segments of differing width and morphology along the strike of the belt; the Lorestan Arc in the northwest, the Dezful Embayment and the Izeh Zone in the center, and the Fars Arc in the southeast.

To the southwest, the Zagros is bounded by the Mesopotamian Foreland Basin and the Persian Gulf where the Arabian Plate flexes down beneath the Zagros. To the northeast, the Zagros are bounded by the Main Zagros Reverse Fault (MZRF) and the Main Recent Fault (MRF) which separate the intense deformation of the Zagros from the almost aseismic central Iranian Plateau (e.g., Talebian & Jackson, 2004; Engdahl et al., 2006). Results of geological (e.g., Dewey & Grantz, 1973; Şengör et al., 1984) and geophysical (e.g., Paul et al., 2006; Shad Manaman & Shomali, 2010) studies suggest that the MZRF is deep-rooted and coincides with the Arabian/Iranian suture zone in the central and southern Zagros. The MZRF now appears to be inactive (e.g., Nissen et al., 2014). The MRF is a young, active fault that follows the trace of the MZRF from the northern-central Zagros to the eastern Anatolian Plateau. The MRF is thought to accommodate much of the right-lateral motion in the NW Zagros related to oblique convergence between Iran and Arabia at this longitude. Northeast of the MZRF is the Sanandaj–Sirjan Zone (SSZ) consisting of a 150–200 km-wide belt of sedimentary and metamorphic Paleozoic to Mesozoic rocks intruded by Jurassic to Early Eocene calc-alkaline magmatic rocks and Middle Eocene gabbros (e.g., Falcon, 1967; Stöcklin, 1968; Agard et al., 2011). As the southwestern margin of central Iran, the SSZ shows a lower level of seismicity and seismic wave attenuation in comparison with the ZFTB (Irandoust et al., 2016). Further to the northeast lies the 50–100 km-wide Urumieh–Dokhtar Magmatic Arc (UDMA) which has been interpreted as an Andean-type magmatic arc associated with the northward subduction of the Neo-Tethys Ocean (e.g., Dewey & Grantz, 1973; Alavi, 1980; Berberian, 1983; Şengör et al., 1984).

Approximately half of the present-day Arabia-Eurasia convergence (10 mm yr^{-1}) is accommodated by shortening in the Zagros Mountains, localized mostly over the SFB (e.g., Tatar et al., 2002; Walpersdorf et al., 2006; Khorrami et al., 2019) and is thought to be accomplished by a combination of folding in the sediments (e.g., Sattarzadeh et al., 1999), high-angle thrust faulting in the basement (e.g., Jackson, 1980; Talebian & Jackson, 2004; Nissen et al., 2011), and thickening of the lower crust (e.g., Hatzfeld et al., 2003; Paul et al., 2006). The attitude of the Zagros with respect to the direction of the Arabian Plate motion changes along the chain. In the southeast (east of 52 °E), the belt trends approximately east-west and is oriented perpendicular to the direction of Arabia-Eurasia convergence. In this part of the range, shortening of the crust occurs by high-angle (30 ° - 60 °) reverse faults. In the central and northern Zagros,

the Arabian Plate motion is oblique to the trend of the range and earthquake fault plane solutions show that the convergence is accommodated by a partitioning with orthogonal strike-slip and thrust faulting on separate parallel fault systems (Talebian & Jackson, 2004). Talebian and Jackson (2004) and Nissen et al. (2011) found no evidence for a seismically-active structural décollement beneath the Zagros. Seismicity in the Zagros is restricted to the region between the MZRF and the Persian Gulf and increases from northwest to southeast. The high level of seismicity observed in the Zagros shows that the belt continues to be active, but the lack of subcrustal seismicity (e.g., Maggi et al., 2000; Engdahl et al., 2006) indicates that subduction has ceased. The strain rates calculated from the historical and recent Zagros earthquakes are less than 10% of those predicted from the Arabia-Iran convergence rate (Shoja-Taheri & Niazi, 1981; Jackson & McKenzie, 1988; Masson et al., 2006).

The Alborz Mountains of northern Iran form a part of a sinuous, 1200 km long and 100 km wide, seismically-active fold-and-thrust belt that extends along the southern side of the SCB and eastward, where they are known as the Binalud Mountains, to near the Afghanistan border. In the west, the Alborz transitions into the N-S trending Talesh Mountains. About a quarter of the overall Arabian-Eurasian convergence south of the SCB (5 ± 2 mm yr^{-1}) is accommodated across the western and central Alborz Mountains (e.g., Vernant et al., 2004b; Djamour et al., 2010).

Faulting in the Alborz is the result of the combined effect of the Arabia-Eurasia convergence and the westward motion of the SCB (e.g., Priestley et al., 1994; Jackson et al., 2002; Allen et al., 2003). The Alborz are bounded by major thrust faults on both sides of the range. In the central Alborz, the reverse faults on the northern side of the range dip southwards, suggesting the underthrusting of the SCB (e.g., Tatar et al., 2007; Hollingsworth et al., 2008), whereas, on the southern side of the range, the reverse faults dip to the north (e.g., Jackson et al., 2002; Hollingsworth et al., 2010b). Deformation in the high Alborz is characterized by a combination of reverse and left-lateral strike-slip faults (e.g., Berberian et al., 1992; Tatar & Hatzfeld, 2009), indicating the partitioning of the oblique convergence between central Iran and the SCB.

Seismicity in the Alborz Mountains occurs primarily in the upper crust with only some infrequent events in the lower crust (e.g., Engdahl et al., 2006; Tatar et al., 2007; Nemati et al., 2011). Earthquake focal mechanisms (e.g., Priestley et al., 1994; Jackson et al., 2002) and Global Positioning System (GPS) observations (e.g., Vernant et al., 2004b; Djamour et al., 2010) show that the present-day N-S shortening is accommodated in the western and central Alborz between 49 °E and 57 °E, with the strike-slip component increasing as the strike of the range changes from E-W to NE-SW (e.g., Vernant et al., 2004b; Djamour et al., 2010; Mousavi et al., 2013; Mattei et al., 2017).

The Talesh Mountains are the westward continuation of the Alborz, and they wrap around the SW margin of the SCB. Teleseismic studies of the Talesh earthquakes show that they are quite distinct from the Alborz earthquakes.

The Talesh earthquakes have mechanisms that indicate thrusting on almost flat faults (such mechanisms are rare in the Alborz) and occur at depths of 15–45 km, deeper than in the Alborz (Priestley et al., 1994; Jackson et al., 2002; Aziz Zanjani et al., 2013). The deeper earthquakes of the Talesh occur close to the Caspian Sea coastline and have slip vectors directed towards the SCB, suggesting that the range is being thrust over the basin. Local seismicity studies (Aziz Zanjani et al., 2013) find that the deep seismicity is restricted to the eastern side of the range and does not continue beneath its western part. GPS observations show that the oblique convergence in the Talesh is accommodated by a combination of ~5 mm yr^{-1} strike-slip faulting in the central part of the range and 2-6 mm yr^{-1} thrust faulting in the northern and southern parts (Djamour et al., 2010).

In the northeast, the Arabia-Eurasia convergence is primarily accommodated by shortening in a series of approximately NW-SE-trending mountain ranges (Fig. 1). The northernmost of these ranges are the Kopet Dag Mountains, a 600-km-long active belt extending from the Caspian Sea to the Afghanistan border and separating the deforming Iranian Plateau to the south from the lowlands of the stable Turan Platform of the Eurasian Plate to the north. The northern limit of the Kopet Dag is marked by the Ashgabat Fault along an abrupt linear range front (Fig. 1). Seismicity and geodetic data mark the Kopet Dag as the northeastern limit of the Arabia-Eurasia deformation zone. The rocks of the Kopet Dag belong to the Turan Platform and represent the closing of the Paleo-Tethys Ocean Basin. They are distinct from the rocks of central Iran, which were part of Gondwana until the early Triassic (e.g., Stöcklin, 1974; Şengör & Kidd, 1979; Berberian & King, 1981). South of the Kopet Dag, N-S shortening is achieved on major thrust systems bounding the Binalud, Sabzevar (Siah Kuh), and Kuh-e Sorkh Mountain Ranges (Alavi, 1992; Shabanian et al., 2009, 2012). The NW-SE trending 130 km-long Binalud Range (Fig. 1), structurally and geologically the eastward continuation of the Alborz Mountains (Alavi, 1992), separates the Kopet Dag from central Iran. The two ranges are separated by the relatively narrow Atrak-Kashafrud Valley which Alavi (1992) suggests is the suture between the Iranian Plateau and Eurasian Plate. The ranges are bounded by active faults, mostly on their southern side, and associated with large historical earthquakes (Hollingsworth et al., 2006).

The Kopet Dag seismicity terminates north at the Ashgabat Fault (Tchalenko, 1975). All well-located earthquakes have focal depths shallower than 15 km (e.g., Priestley et al., 1994; Jackson et al., 2002; Hollingsworth et al., 2010a) and there is no evidence of subcrustal seismicity. Earthquake mechanisms have slip vectors that suggest shortening across the range is accommodated on thrust and right-lateral strike-slip fault systems in the western and central Kopet Dag (west of 59 ° E), and range-bounding thrust faults in the eastern Kopet Dag (east of 59 ° E) (Hollingsworth et al., 2006). GPS measurements (e.g., Vernant et al., 2004a; Masson et al., 2007; Khorrami et al., 2019) show that the northward Arabia-Eurasia convergence at the longitude of eastern Iran is 23 mm yr^{-1}. About 4 to 11 mm yr^{-1} of this motion is accommodated in the northeast of

the Plateau (e.g., Vernant et al., 2004a; Reilinger et al., 2006; Shabanian et al., 2009). The regional deformation field from GPS observations shows that distributed right-lateral shearing is accommodated across a wide part of eastern Iran (Masson et al., 2005; Khorrami et al., 2019). In the northeast, this right-lateral shear is converted into shortening across the Koh-e Sorkh, Binalud and Kopet Dag Ranges. At 58 ° E, the N-S shortening is occurring at a rate of 4.5±0.5 mm yr^{-1}, decreases eastward and dies out in the vicinity of the Afghanistan border (Walters et al., 2013).

The Iranian Plateau is bounded on the east by the Helmand Block, which is part of stable Eurasia (Jackson & McKenzie, 1984), and on the south by the Makran Subduction Zone. Plate reconstructions imply that the convergence rate increases from 37 mm yr^{-1} in the western Makran to 42 mm yr^{-1} in the eastern Makran (DeMets et al., 1990), but GPS measurements estimate the present convergence rate of the westernmost Makran to be only 20 mm yr^{-1} (Vernant et al., 2004a; Khorrami et al., 2019). The Makran is separated from the Arabia-Eurasia continental collision zone in the Zagros by the right-lateral Zendan-Minab-Palami (ZMP) fault system (Fig.1), assumed to be the tectonic boundary between the two zones (Vernant et al., 2004b; Molinaro et al., 2004; Regard et al., 2004, 2005; Bayer et al., 2006; Yamini-Fard et al., 2007). The ZMP fault zone experiences a low level of seismicity (Yamini-Fard et al., 2007) and does not appear to be a major throughgoing lithospheric fault system, but a localized transition zone accommodating the differential motion between the Zagros and Makran (Gholamzadeh et al., 2009). The western Makran experiences a lower level of seismicity compared to the eastern Makran (Byrne et al., 1992). A short-duration ocean bottom seismometers deployed offshore recorded no noticeable seismicity (Niazi et al., 1980).

Central Iran is a relatively flat, aseismic region composed of a number of rigid blocks trapped between the compressional belts of Zagros, Alborz, and Kopet Dag, the stable Helmand Block, and the Makran Subduction Zone. The part of shortening not taken up in the Zagros results in N-S right-lateral shear in the central Iranian Plateau south of 34 ° N and between 52 ° E and 61 ° E. This shear is accommodated on a number of strike-slip fault systems that trend approximately N-S, particularly those surrounding the Lut Block (e.g., Jackson & McKenzie, 1984; Jackson et al., 1995; Berberian & Yeats, 1999). North of 34 ° N, the right-lateral shear is accommodated by E-W left-lateral faults that rotate clockwise about the vertical axis (e.g., Jackson & McKenzie, 1984; Mattei et al., 2012). Seismicity, mountainous topography, and active faulting all terminate abruptly east of 62 ° E.

3 Data and methodology

A better understanding of the dynamics and evolution of the Iranian Plateau requires constraints on the lithospheric structure, including spatial and depth variations of V_s in the crust and uppermost mantle, changes in the nature and depth of the Mohorovičić discontinuity (Moho) and the crustal and uppermost mantle wave-speed and anisotropy variation. In this section, we describe the

data and the procedure by which such a model was derived. We achieved this with the analysis of large datasets of receiver functions and Rayleigh wave group dispersions.

3.1 Data

The seismograms we analyzed come primarily from permanent and temporary seismographs located within Iran (Fig. 2), and we supplemented the Iran recordings with some recordings at seismographs in the regions surrounding the Iranian Plateau. The permanent seismographs within Iran are operated by the Iranian National Seismic Network (INSN) and the Iranian Seismological Center (IRSC). In addition, we included recordings from the II, IU, KO, and KW permanent networks which we obtained from the Incorporated Research Institution for Seismology (IRIS) data center. Data from these permanent seismic networks are supplemented by seismograms from a number of temporary seismic networks within Iran operated by the Institute for Advanced Studies in Basic Sciences (IASBS), the University of Cambridge (UC), the Institut des Sciences de la Terre (LGIT), the International Institute for Seismology and Earthquake Engineering (IIEES), and the China-Iran Geological and Geophysical Survey in the Iranian Plateau (CIGSIP). We also added dispersion data crossing the Iranian Plateau from a dataset compiled by Gilligan and Priestley (2018) over a region extending from central Asia to 20 ° E west of Iran.

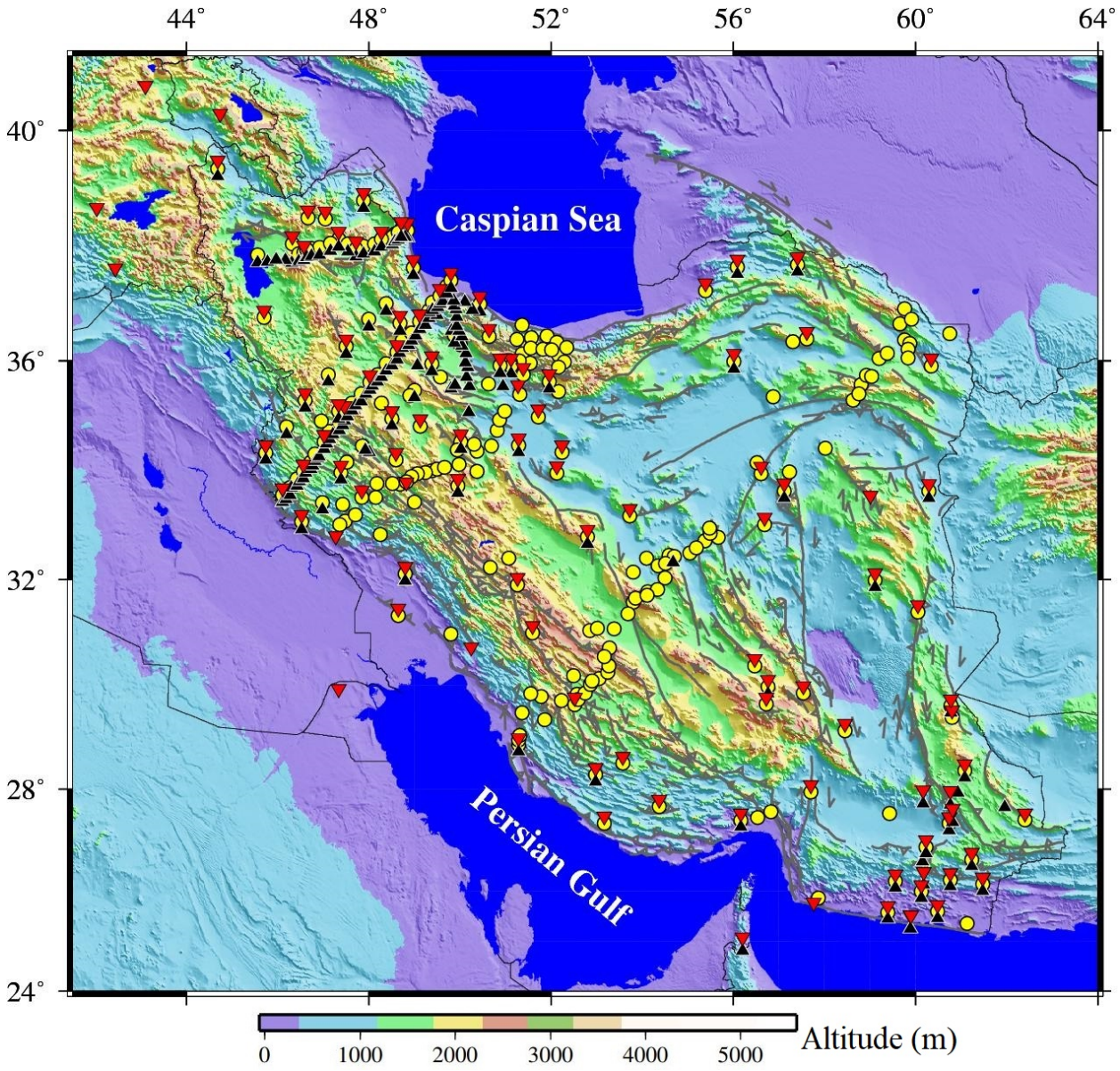

Figure 2. Distribution of the stations whose data were analyzed in this study. The reversed red triangles, the black triangles, and the yellow circles show the locations of stations used for analysis of ambient noise cross-correlations, regional earthquakes, and P receiver functions, respectively.

3.2 Analysis method

To derive a detailed image of the crust beneath the seismographs (Fig. 2), we

jointly inverted fundamental mode Rayleigh wave group velocities and teleseismic P receiver functions.

3.2.1 Surface wave analysis

We used the fundamental mode Rayleigh wave group velocity dispersion curves derived from regional earthquakes and interstation ambient noise cross-correlations. We extracted the shorter-period group velocities from the analysis of ambient noise measured from the continuous seismic data and the longer-period velocities from regional earthquakes. The long-period dispersion constrains the crust and the shallow mantle part of the lithosphere, while the short-period dispersion constrains the upper crust. Inverting the group velocity dispersion curves provides an absolute shear-wave velocity for the crust and the shallow mantle.

We employed a multiple-filter analysis (Dziewonski et al., 1969; Herrmann, 2013) to analyze more than 10455 vertical-component seismograms from magnitude 4 and greater earthquakes recorded at epicentral distances between 100 and 4500 km. From these seismograms, we could extract fundamental mode group velocity dispersion primarily in the 15 to 70 s period range. In addition, a number of shorter-period velocities were measured from a smaller group of earthquakes. The dispersion data were obtained from a total of 4303 events, although the number of observations at each period is smaller than this number. To this, we added the Rayleigh wave group velocity measurements of Gilligan and Priestley (2018) for events whose ray paths crossed the Iranian Plateau. Gilligan and Priestley (2018) measured dispersion using an identical procedure to that we have used.

We obtained the short-period group velocity dispersion (mostly 5 to 35 s) from ambient noise cross-correlation at the sites indicated in Figure 2. These stations were not all running concurrently. For the ambient noise analysis, we followed the steps outlined in Bensen et al. (2007). We: 1) decimated the vertical-component time series to 1 Hz; 2) cut the continuous time series into 1-day segments; 3) removed the instrument response, mean and trend; 4) band-pass filtered the time series from 0.01 to 0.5 Hz; 5) applied a running-absolute-mean (50 s window) as a time domain normalization to reduce the effect of earthquakes on the cross-correlations; and 6) spectrally whitened the time series. We then cross-correlated the day-long time series for each station pair and stacked the cross-correlation series to increase the signal-to-noise of the final cross-correlations. After rejecting the low-quality cross-correlations, we were able to extract 1567 dispersion curves using the same multiple-filter analysis method as applied to the regional earthquakes.

After combining dispersion curves of earthquakes and ambient noise, we found a considerable number of similar ray paths. To reduce redundant paths, remove outliers, and measure statistical errors, all the group dispersion curves for similar paths were clustered. For each period, paths with endpoints (stations and events) within 4% of the path length from one another were used to build sum-

mary rays. The mean and standard deviation of group velocity measurements in each cluster were calculated. Paths in a cluster where the group velocity measurement fell outside 1.5 times the standard deviations of the mean of the cluster were considered outliers and removed, and the mean and standard deviation were recalculated. In the following group velocity inversion, a cluster is considered to be a single measurement with the group velocity as the mean of the cluster, the error as the standard deviation of the cluster, and the start and end points are the mean location of the start and end points of paths in the cluster. Paths that could not be used to make summary rays were treated as single measurements with assigned an error equal to the mean standard deviation of all clusters at a given period. Figure 3a shows the number of paths before and after clustering at different periods. To retrieve the Rayleigh wave azimuthal anisotropy requires a good azimuthal distribution of propagation paths. Fig. 3b-g shows the path coverage in terms of path density and a Voronoi diagram. The sizes of the Voronoi cells indicate the length-scale of the local structure that can be resolved, while the shapes of the cells provide information on the variation of azimuthal resolution (Debayle & Sambridge, 2004).

We built tomographic dispersion maps at sixteen periods between 5 and 70 s for the fundamental mode group velocities and constructed a grid with a $1^\circ \times 1^\circ$ spacing for the whole region of the sources and receivers. Then we employed the method of Debayle and Sambridge (2004) to invert path-average surface wave measurements for both isotropic and anisotropic terms. This inversion method is based on continuous regionalization of Montagner (1986) in which physical properties of the model are considered as *a priori* information. The variation of Rayleigh wave velocity with propagation direction (Smith & Dahlen, 1973) involves one isotropic coefficient and two anisotropic coefficients associated with the 2θ terms. The Debayle and Sambridge (2004) inversion retrieves the three unknowns for each grid point of the two-dimensional model. For the source-receiver path j we have

$$\frac{1}{U_j(T)} = \frac{1}{_j} \int_j \frac{\mathrm{d}s_j}{U(T,\theta,\varphi)}$$

where $U_j(T)$ is the path-average group wave-speed at period T measured along the path, θ and φ are the coordinates of the geographical points along the great circle, and $_j$ is the source-receiver distance. $U(T,\theta,\varphi)$ is the local group velocity at the geographical point (θ,φ) and period T**.** Using the great circle approximation, the inverse problem can be written as a linear relationship between the data vector $\mathbf{d}$ containing the average group slowness $\frac{1}{U(T,\theta,\varphi)}$ along each path and a parameter vector $\mathbf{m}$ containing the local group slowness at each geographical point along the path. For the segmented path j^{th} s, we can write

$$\mathbf{d} = G\mathbf{m}$$

where the matrix G contains the partial derivatives $\frac{s}{j}$. A Gaussian *a priori* covariance function controls the horizontal degree of smoothing in the inverted model. While based on the continuous formulations of Montagner (1986), the Debayle and Sambridge (2004) scheme incorporates sophisticated geometrical algorithms which dramatically increase the computational efficiency of the inversion. Figure 4 shows tomographic group maps at six selected periods.

In addition to the Voronoi diagram tests (Fig. 3) used to assess the resolution and recovery of group velocity values in the tomographic maps, we performed checkerboard tests using synthetic input models with 2° and 1° square-shaped alternating patterns of high and low velocities as a pure isotropic medium. The velocity perturbations of the synthetic input (Fig. S1) for different periods are $\pm 15\%$ of the mean velocity of the input data. Synthetic data are then inverted with the aim of retrieving the initial checkerboard patterns. The inversion of synthetic data can reveal whether or not azimuthal anisotropy is introduced into the final result of an initially isotropic model. The results of the checkerboard tests (Fig. S1) indicate that both 2° and 1° checkers are mostly well resolved across the Iranian Plateau.

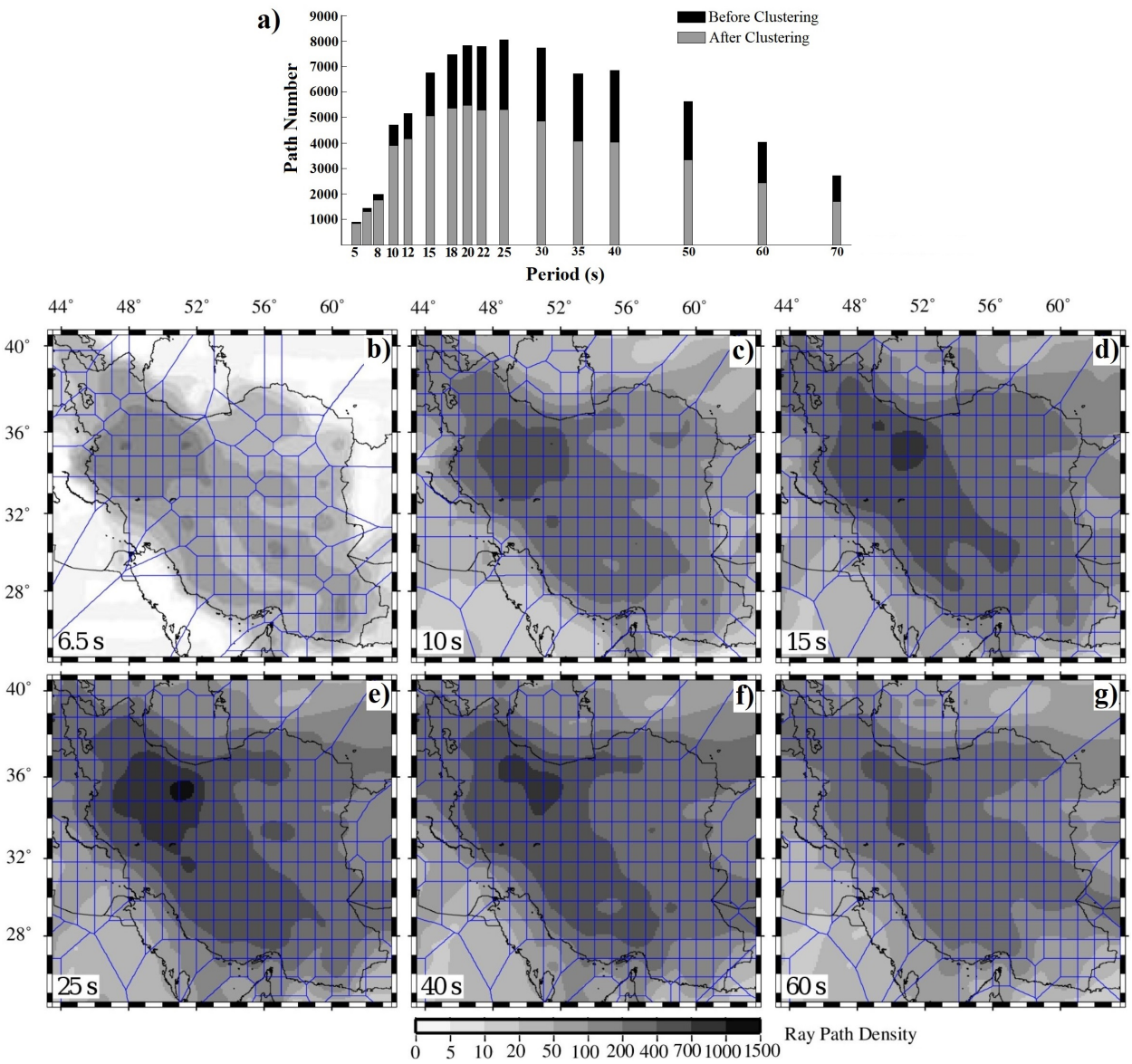

Figure 3. a) The number of paths before and after clustering that cross the Iranian Plateau region for each period fundamental mode Rayleigh wave group velocity. b-g) Optimized Voronoi diagram and ray path density at different periods. Over most of the Plateau the Voronoi cells remain at the starting value a $1^\circ \times 1^\circ$ and the path density exceeds 50 paths per cell. The size of the Voronoi cell indicates the scale of the surface wave resolution at which we can extract the *Vs* and anisotropy structure (Debayle & Sambridge, 2004).

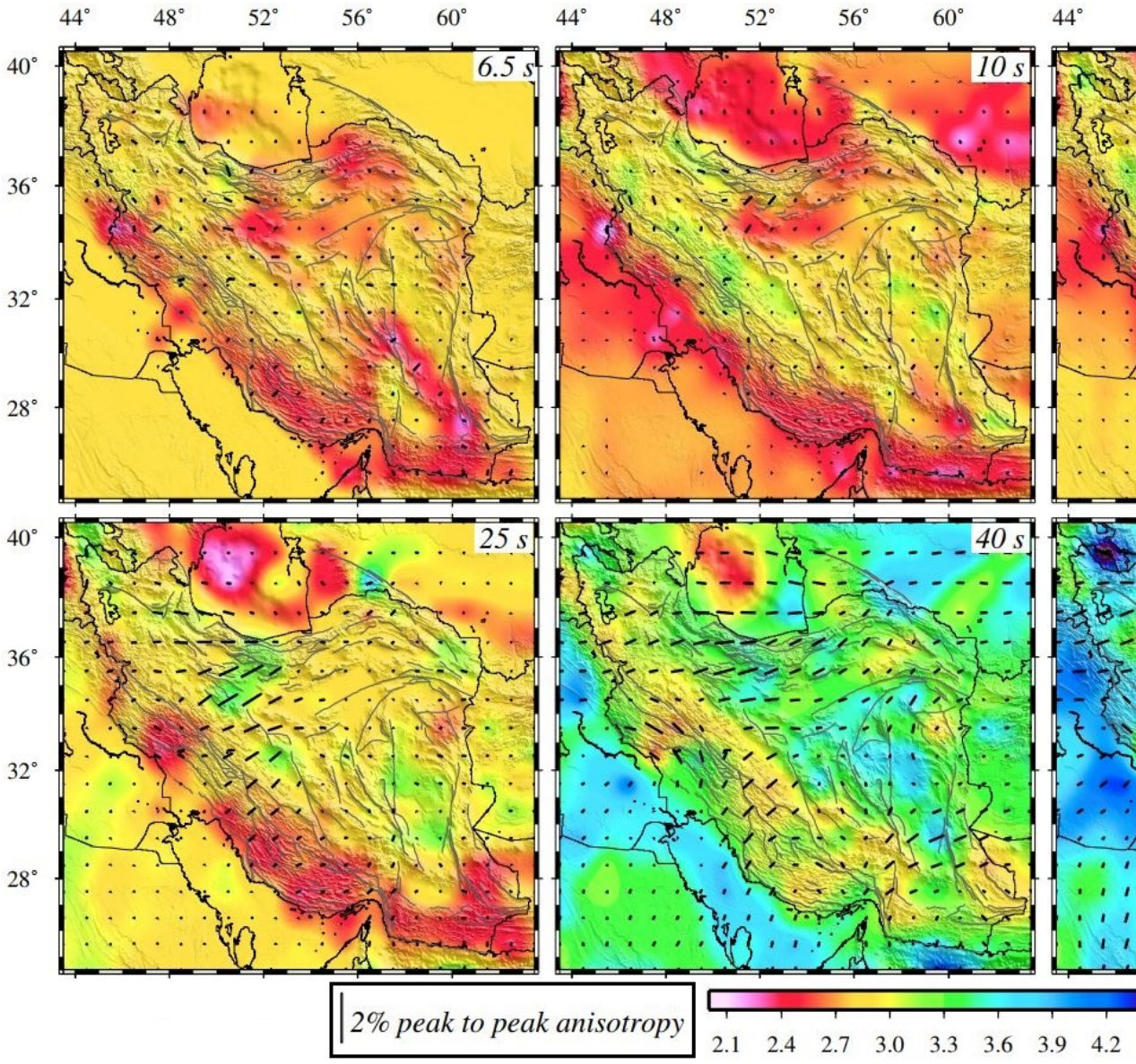

Figure 4. Representative results of fundamental mode Rayleigh wave group velocity tomography showing both isotropic and azimuthally anisotropic terms at representative periods.

3.2.2 Receiver function analysis and joint inversion

Inversion of the 5-70 s group velocities provides a "filtered" but absolute wave-speed image of the crust and uppermost mantle. To impose more high-wavenumber structure on this image, we employed a teleseismic *P*-wave

receiver function analysis of data from the seismographs in Fig. 2. This technique provides more details of features such as sharp velocity gradients and discontinuities (e.g., the Moho and sedimentary basement interface) which are not achievable from the analysis of the surface waves. Teleseismic receiver function analysis (Phinney, 1964; Burdick & Langston, 1977; Langston, 1977) is now an established seismological tool for investigating the wave-speed structure beneath a seismograph site.

For P receiver function calculations, we used teleseisms recorded by the permanent and temporary seismic networks within the Iranian Plateau. Our receiver function analysis methodology is summarized in Fig. 5. All teleseismic waveforms recorded at the seismograph sites (Fig. 2) from events greater than m_b 5 and in the distance range 30° to 90° were band-pass filtered between 0.05 and 2.0 Hz, rotated from NS and EW to radial and transverse with respect to the event-station great-circle path, and the receiver functions were computed using the iterative time-domain deconvolution method of Ligorria and Ammon (1999). To stabilize the deconvolution, we low-pass filtered the receiver function waveforms using a Gaussian width 1.6 (corner frequency 1.0 Hz). The receiver functions were next corrected for the Ps-P move-out to a common distance of 67°. Figure 5a shows the azimuthal distribution of the calculated receiver functions at one of the stations (ZNJK). Finally, we stacked all of the receiver functions for each station to obtain an average receiver function with lower and upper error bounds (Fig 5b). We did not consider stations for which there were fewer than three receiver functions or those showing noisy output. This resulted in mean receiver functions and error bounds for 236 stations.

We then interpolated the group velocity maps (Fig. 4) to create a pseudo-group velocity dispersion (Fig. 5c) curve for each site and simultaneously inverted receiver functions and pseudo-dispersion data using a finely parameterized starting structure defined by 2-km-thick flat-lying isotropic layers with constant V_s and V_p/V_s for each layer and extending to 280 km depth. The initial velocity model of the crust and upper mantle used in starting the inversion (e.g., Fig. 5d) is based on the AK135 global model (Kennett et al., 1995) but with the crustal velocities replaced with the uppermost mantle values of AK135 (4.48 km s^{-1} to 110 km depth). Thus, there is no *a priori* crustal model imposed on the joint inversion and the inversion procedure can introduce layering and a Moho as required by the data. Our underlying assumptions are: the structure beneath each receiver is close to one-dimensional (1D), can be approximated by plane isotropic layers, and the effect of side scattering from local crustal heterogeneity is minimal. Joint inversion was performed using the linearized least-squares inversion algorithm of Herrmann (2013).

We implemented an automated scheme for estimating the Moho depth. From the final inversion V_s model, we determined the Moho depth as where the velocity changes rapidly from V_s typical of the continental crust to that more typical of the mantle. For the Iranian region, we have found that the velocity of the shallowest mantle is mostly in the range of 4.0-4.3 km s^{-1}. Fig. 5b-d demon-

strates the joint inversion and Moho detection steps for one of the stations. An initial Moho was estimated as the point at which the V_s gradient between the above-mentioned velocities reaches the largest value within the depth range of 30 and 70 km. Next, a simple two-layer (crust-mantle) model was constructed from the average V_s in the layers above and beneath the estimated Moho (the dashed light blue line of Fig. 5d). We then inverted the receiver function and dispersion data with the two-layer initial model to attain a V_s model (the green line in Fig. 5d). Finally, a synthetic receiver function and dispersion curve were produced based on the V_s model of the previous step (the green line in Fig. 5b). When the Moho estimation is correct, the synthetic receiver function and dispersion curve calculated from the two-layer V_s model closely match the observations from the site.

The distribution of the seismic stations at which P receiver functions were calculated is not uniform over the Plateau. Following Chai et al. (2015), we divided the study region into $0.5^\circ \times 0.5^\circ$ cells (Fig. 6) and computed a weighted average of all the stacked and move-out corrected receiver functions within a 1° distance of each cell center. The receiver functions within 30 km of a cell center were given a weight of 1.0, and those located between 30 and 110 km had weights decreasing linearly with distance to 0.0 at 110 km distance from the cell center. For cells containing an interpolated receiver function (denoted by black stars in Fig. 6) we jointly inverted the two data to determine a V_s model of the crust and upper mantle and crustal thickness in the same manner as described above for individual stations. The influence of each data set (surface wave and receiver function) in the inversion is controlled by an *a priori* weighting parameter which varies between 0 and 100%. We assign the same weight (50%) to both the dispersion data and receiver functions for grid cells containing at least one station-centered receiver function within 30 km. For the grid cells whose contributed station-centered receiver functions lie in the distance range of 30-100 km, the interpolated receiver function's influence factor drops to 40%.

After the receiver function interpolation, some regions (for example, within the Great Kavir and Dasht-e Lut) were still left with no receiver functions (denoted by red stars in Fig. 6). Nevertheless, the dense surface wave path coverage for these regions (Fig. 3) enabled us to estimate a reliable crust and uppermost mantle velocity model through the inversion of dispersion data. To better constrain the crustal structure of these points, we introduced a mean V_s model of neighboring cells as the initial model of surface wave inversion. Since there were no receiver functions for these cells, we determined the depth of the Moho as the point where the velocity gradient typical of continental crust meets that which is typical of the uppermost mantle. Fig. 6 shows several examples of shear-wave velocity models obtained from the joint, as well as dispersion-only inversions.

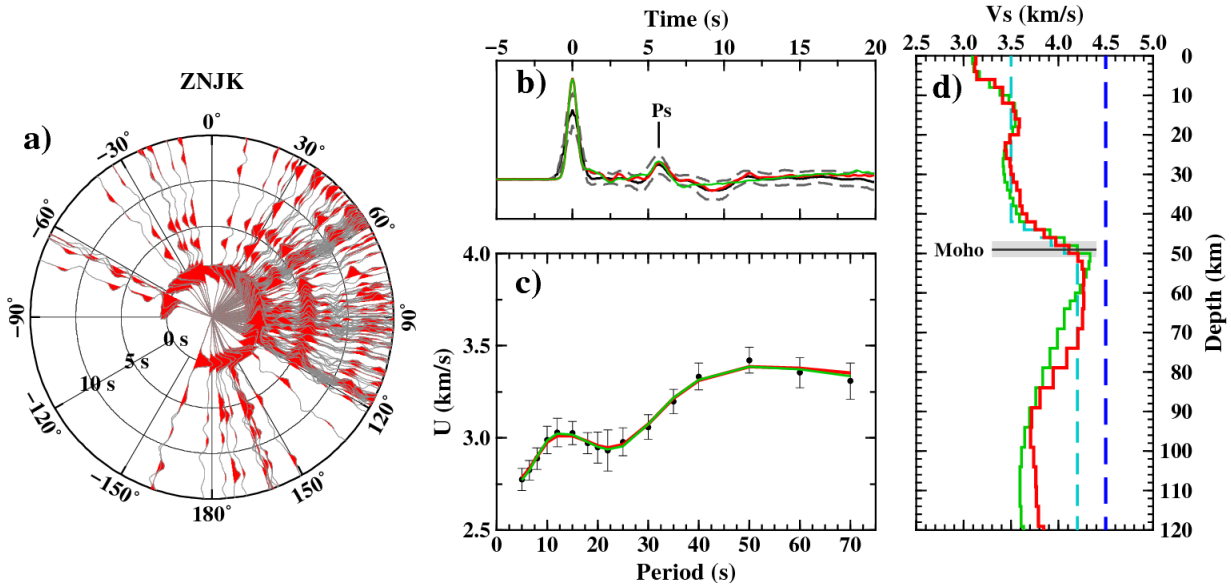

Figure 5. Steps of joint inversion of the P receiver function – surface wave dispersion data and the Moho detection for station ZNJK: a) Distribution of move-out corrected radial receiver functions with back azimuth; b) Mean receiver function (solid black line) with the corresponding error bands (dashed gray lines), the synthetic receiver function for the final crustal structure from the joint inversion (solid red line), and the synthetic receiver function for the two-layer initial model based on the estimated Moho depth (solid green line); c) Observed dispersion curve (black circles with error bars), the synthetic dispersion curve for the inversion velocity model (solid red line), and the synthetic dispersion curve for the two-layer initial model (solid green line); d) Starting wave-speed model for the joint inversion (dashed blue line), the inversion V_s model for the crust (solid red line), the two-layer initial model (dashed light-blue line), and the result of the observed dispersion curve inversion with the initial model (solid green line).

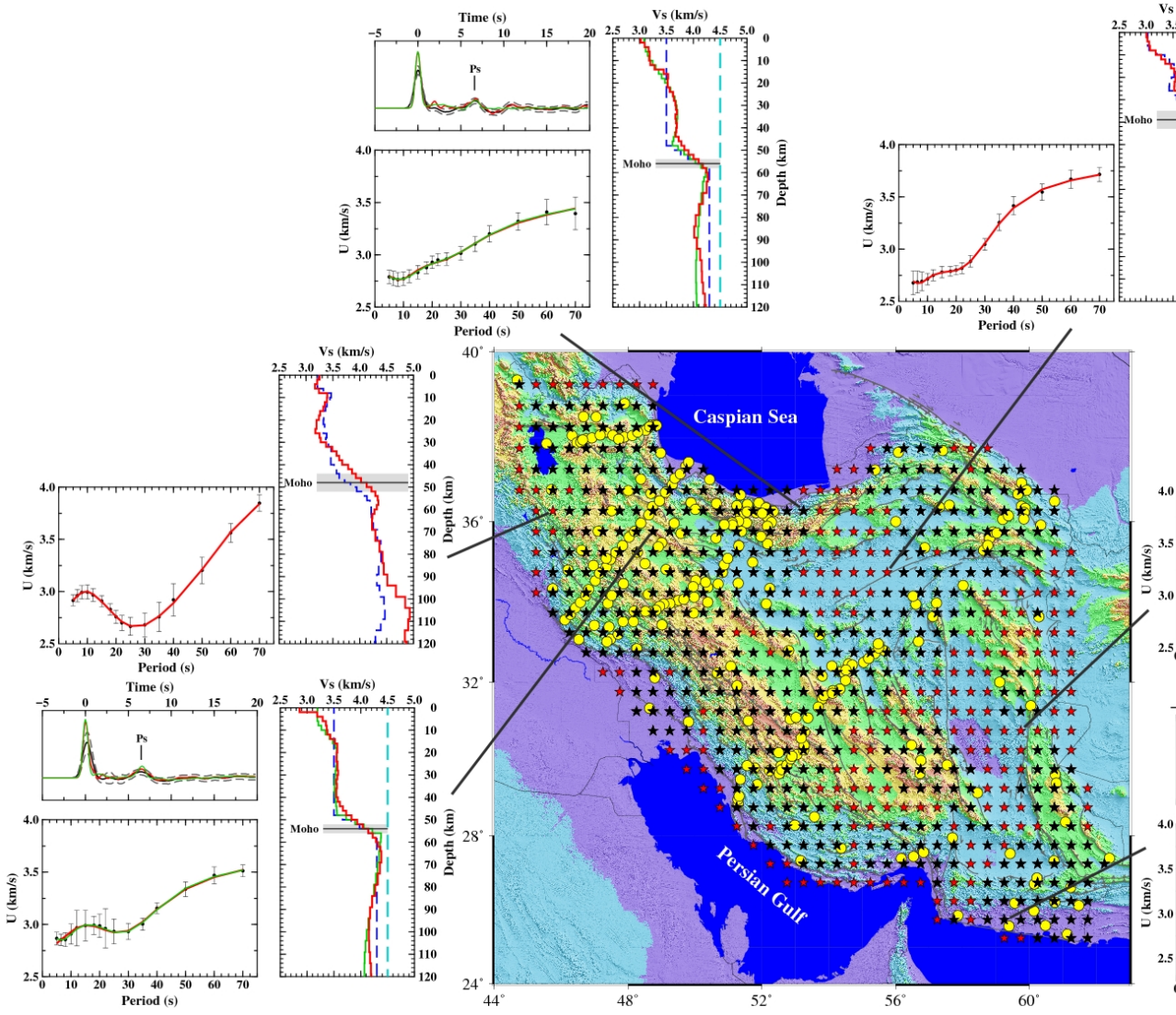

Figure 6. Map showing receiver function interpolation scheme and examples of the inversion results for crustal structure. Yellow circles denote locations of seismographs with receiver function inversion results, black stars denote cell centers with at least two observed receiver functions within 1° of the cell center and red stars denote cell centers with no interpolated receiver function. Format of the inversions is the same as that of Figure 5 except that the station receiver functions are replaced by the interpolated receiver functions (black stars). For locations with no interpolated receiver functions (red stars) the crustal structure is only constrained by the fundamental mode Rayleigh wave group velocity dispersion.

4.1 Fundamental mode Rayleigh wave group velocities

The isotropic and anisotropic maps of Rayleigh wave group velocities were obtained for 16 different periods between 5 and 70 s. Fig. 4 shows the group velocity maps for periods 6.5, 10, 15, 25, 40, and 60 s. Periods shorter than 25 s constrain the upper crust and show low group velocities in areas of known deep sediments; i.e. the SCB, the Zagros Foreland Basin and most of the fold-and-thrust belt, the Makran Accretionary Wedge, and the Great Kavir region. The volcanic belt of the Makran Subduction Zone (north of the Jazmurian Depression and in the southern Sistan Suture Zone) also has anomalously low velocities. The SSZ and UDMA, and central Iran have higher velocities for the same period range. In the north, the Alborz region does not show particularly low velocities at shallow depths, but the western Kopet Dag has relatively low velocities in the shortest periods. Mid-period group velocities (40-60 s) constrain the lower crust and Moho depth. The SCB is again dominated by low velocities, but now the SSZ has become a prominent low-velocity region. In the Zagros, the southern part of the Lorestan Arc in the northwest, and to some extent the Fars region in the south are underlain by low velocities. The southern Sistan Suture Zone is also a region of low velocity. The Alborz, most of central Iran, and the Makran region constitute the regions of high velocity. At the longest periods (60-70 s), the lesser Caucasus in the northwest, the central Alborz, and northeastern Iran show the highest velocities. In the ZFTB, except for two local low-velocity regions in the Lorestan and Fars regions, group velocities are generally high, as they are in the Makran. In the SSZ and central Iran, the group velocities are rather variable, but in general are low. For all of the periods shown in Figure 4, the Jazmurian Depression and the Lut Block further north consistently stand out as high-velocity regions.

4.2 Lateral and depth variations of V_s in the crust and uppermost mantle

Figures 7 and 8 (a-c) show maps of shear-wave velocity variations at different depths in the crust and uppermost mantle. Throughout the southern margin of the Zagros and in the Makran Accretionary Wedge region, very low V_s (<3.1 km s^{-1}) prevails down to about 12-18 km depth (Fig. 7a-b and Fig 8a), reflecting very thick sedimentary sequences. The same is true in the SCB where the low velocities continue down to a depth of about 20 km. Smaller internal basins such as the Jazmurian and the Great Kavir also show low V_s at shallow depths. In the Alborz, significant variations are seen between the western and eastern parts of the range. At mid-crustal depths (~20 km depth in Fig. 7c) the regions of central Iran, central Alborz, and eastern Kopet Dag stand out as generally high-V_s regions, while in the Zagros and Makran, low-V_s prevails. In the lower crust (40 km depth in Fig. 7d and 8b) the contrast between the interior of the high-V_s, low-topography central Iran, and the surrounding low-V_s mountain regions becomes sharper. In the same depth range in the Zagros collision zone, the low-velocity anomalies shift towards the High Zagros and the SSZ. The

Makran Subduction Front becomes a high-V_s region with velocity increasing from west to east, while its volcanic arc region shows anomalously low-V_s. The SCB continues to be a region of low-V_s well into mantle depths (Fig. 8c). Below the Moho depth range (i.e. 60-90 km) V_s higher than 4.8 km s^{-1} is only seen outside the margins of the Iranian Plateau (Fig. 7e-f and 8c), i.e., in the Arabian and Turan Platforms in the south and north, respectively, and in the Caucasus. In the interior of the Plateau, sub-Moho V_s rarely exceeds 4.3 km s^{-1} and is generally below global average values. The most significant upper-mantle low-V_s is observed under the volcanic arc of the Makran, and the southwestern margin of SCB in the western Alborz (Fig. 7f).

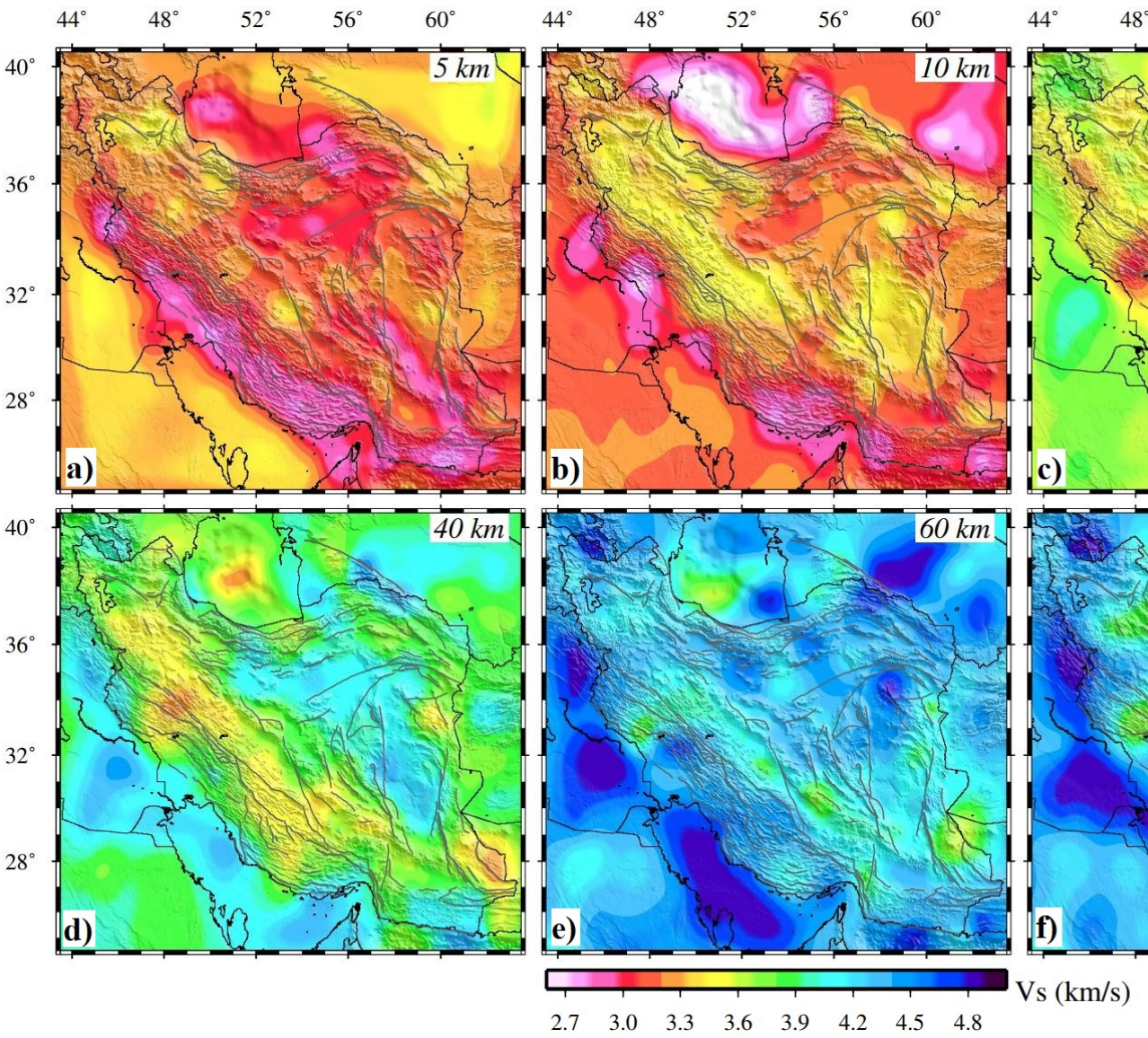

Figure 7. Variations of shear-wave velocity at representative depths.

4.3 Lateral variations of crustal thickness

Fig. 8d shows the lateral variations of Moho depth obtained from the inversion procedure. For grid cells where a receiver function estimate was available, the Moho depth was extracted from the output V_s model of the joint inversion. For grid cells without a receiver function, the Moho depth was estimated from the inversion of only the dispersion curves. For these cells the crustal thickness estimate could be less accurate. The crustal thicknesses of our model are tabulated

in Table S1. The region of thickest crust (~65 km) coincides with the SSZ on the NE margin of the Zagros. All of the compressional belts – the Zagros, Talesh, Alborz, Kopet Dag and Binalud Mountains – have a thicker-than-normal crust (>45 km). More normal continental crustal thickness (35-40 km) is observed beneath the low-deformation regions, i.e. the Great Kavir and the Lut Block. The thinnest crust (<35 km) is observed in the Makran Subduction Zone, and in the SW margin of the SCB. In NE Iran, the thickest crust is observed not in the Kopet Dag, but in the Kuh-e Sorkh and Binalud Mountains to its south (Fig. 8d).

To aid the discussion, we constructed nine profiles of the V_s and Moho variations across and along the major tectonic zones of the Iranian Plateau. The locations of the profiles are shown in Fig 8b and the profiles are displayed in Fig 9. Profiles A and B traverse the Lorestan Arc of the western Zagros and the Alborz Mountains. The low-velocity tongue extending from the upper crust of the Zagros to the lower crust of the SSZ and UDMA clearly shows the underthrusting of the Arabian Plate beneath central Iran. Profiles C-D and E-F extend across the central part of the Zagros and central-eastern Alborz. The crustal features in this part of the collision zone are similar to those in the previous profiles; that is, the crust attains its maximum thickness and lowest V_s north of the Zagros in the SSZ. The crust of the Alborz is somewhat higher velocity. Profiles G and I cross the southern Zagros range. Profile G corresponds to the broadest region of the Zagros in the Fars Arc. Along this profile, the underthrusting of the Zagros crust beneath SSZ and UDMA is not as apparent; nevertheless, the crust reaches its maximum thickness under UDMA. Profile J shows a cross-section of the Zagros along its strike. Except near the NW and SE terminations of the range, the Moho depth shows relative uniformity throughout the range, undulating around the 50 km depth. The velocity structure shows greater variations, with significant low-V_s reaching lower crustal depths in the Lorestan Arc (profile B). The part of the profile known as the Izeh Zone, shows high-V_s throughout the depth of the crust. This zone is the narrowest segment of the Zagros belt (see also profile C).

In NE Iran, the eastern part of the Dorouneh Fault (DF on profiles H, I, and K, and in Fig 8d), is located above a major gradient of Moho, separating a thinner crust to its south from a thicker one to its north. The profiles show a crustal thickness difference of about 10 km between the western and eastern Kopet Dag Mountains. Profile K traverses the Makran Subduction Zone, Jazmurian Depression, and Lut regions. It shows the subduction zone near its transition to the Zagros Mountains. The Makran Accretionary Wedge is present as a thick low-V_s zone extending to about 20-30 km depth. The Moho depths plotted under the wedge probably indicate the base of the subducting oceanic, or a very thinned continental crust in westernmost Makran where the subduction transitions to the Zagros continental collision. The subducting crust is delineated by the positions of subduction earthquakes. The crust of the Jazmurian has a relatively high-Vs with the Moho at 45-50 km depth. Further north, the Lut Block has a somewhat thinner crust with respect to its surroundings. It has

low-V_s near the top due to its thick sedimentary cover, but the basement is markedly higher V_s than its neighboring regions. Both the Jazmurian and Lut have high sub-Moho velocities. Profile L is a W-E section across southern Iran. Comparison with profile K, indicates that the sharpest Moho gradient around the Lut Block is under its western boundary with central Iran.

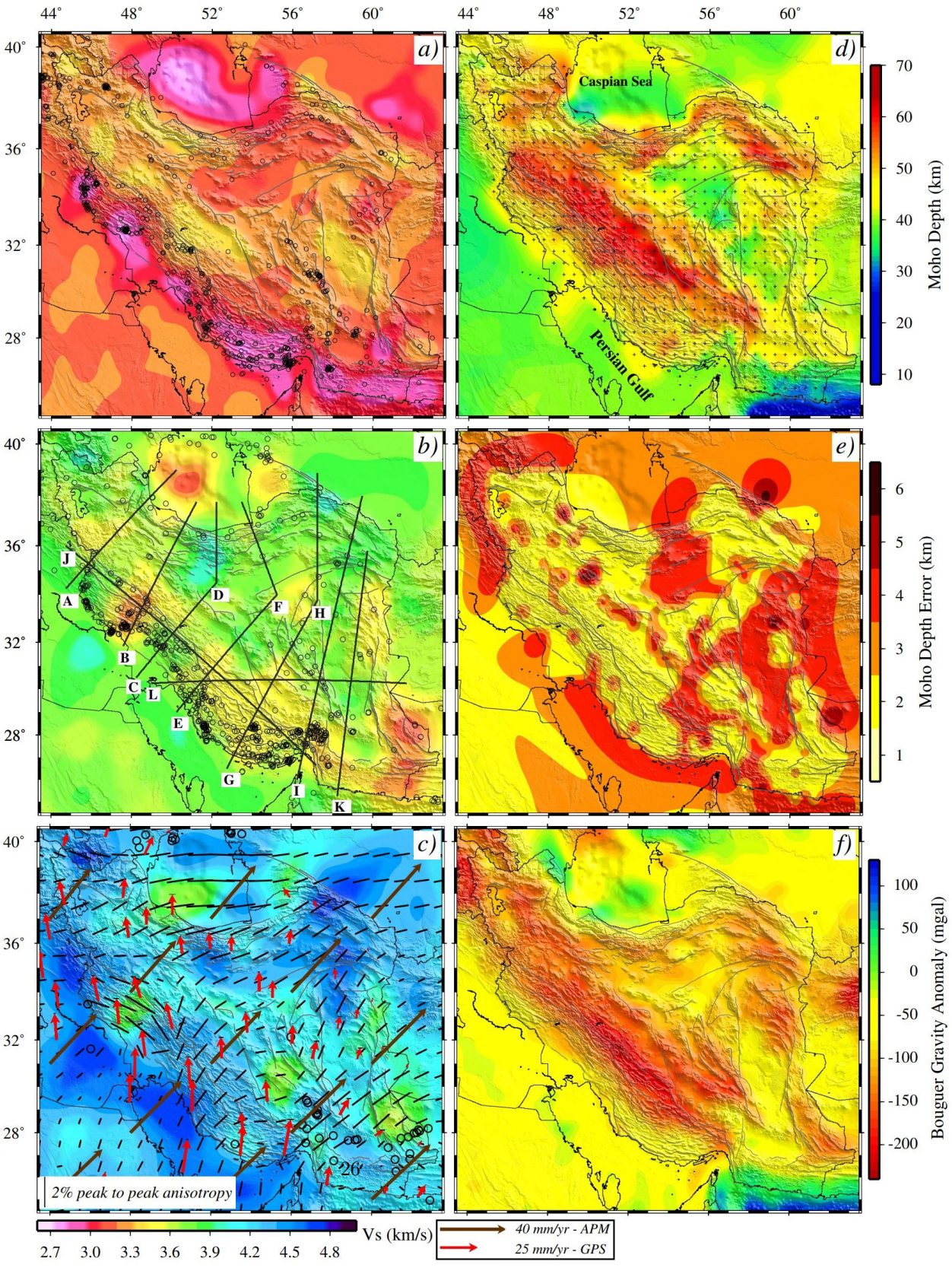
44°
48°
52°
56°
60°
40°
36°
32°
28°
a)
b)
c)
d)
e)
f)
Caspian Sea
Persian Gulf
A
B
C
D
E
F
G
H
I
J
K
L
26
2% peak to peak anisotropy
Vs (km/s)
2.7
3.0
3.3
3.6
3.9
4.2
4.5
4.8
40 mm/yr - APM
25 mm/yr - GPS
Moho Depth (km)
70
60
50
40
30
20
10
Moho Depth Error (km)
6
5
4
3
2
1
Bouguer Gravity Anomaly (mgal)
100
50
0
-50
-100
-150
-200

Figure 8. a-c) Lateral variations in the average V_s for a) the upper crust (<15 km-depth), b) the lower crust (>15 km-depth), and c) the sub-Moho mantle (<110 km) of the Iranian Plateau. Earthquakes with magnitude 5 and greater in the same depth range are plotted as circles in maps shown in panels a-c. The black lines over-plotted on the lower crustal V_s map show the locations of the crustal cross-sections shown in Figure 9. The lateral variation of sub-Moho V_s and azimuthal anisotropy (black bars) are shown in (c). Over-plotted on (c) are the variations in the GPS-observed deformation field (red arrows) (Khorrami et al., 2019) and APM field vectors (brown arrows) (Kreemer et al., 2014). d) The lateral variation in crustal thickness for the Iranian Plateau. The + symbols denote points at which the crustal thickness is calculated in this study (see Fig. 6 for the details). Note – Our model for the crustal thickness of the Plateau is merged with CRUST1.0 (Laske et al., 2013) in the surrounding region. e) Moho depth error map. f) Variation of Bouguer gravity anomaly (Zingerle et al., 2019). A shear-wave velocity scale for (a-c) is given under (c) and scales for Moho depth, Moho depth error, and Bouguer gravity anomaly are plotted besides (d-f), respectively.

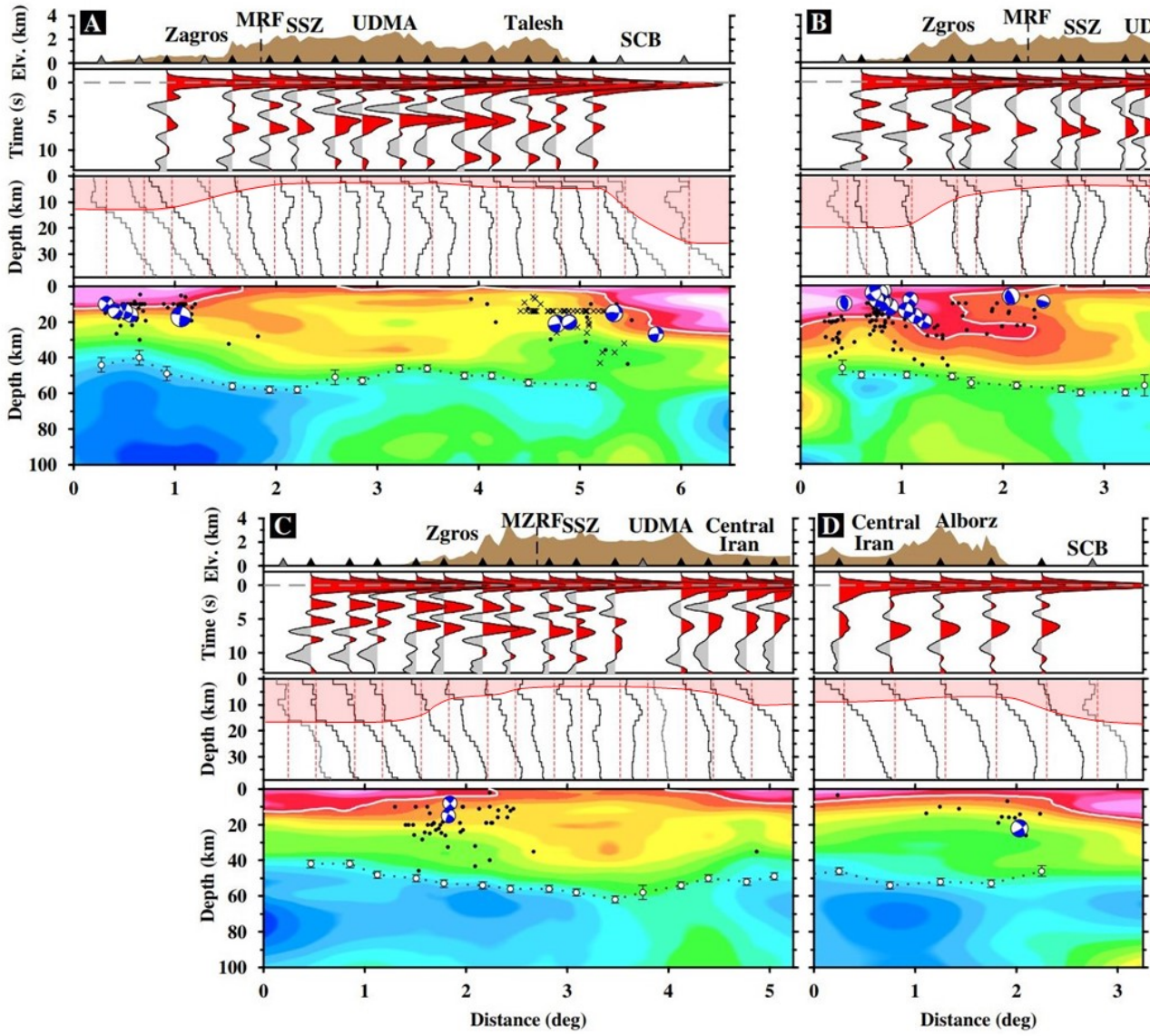

Figure 9. Cross-sections of profiles indicated in Figure. 8b. For each profile, the panels from top to bottom show topography with main geological features, interpolated receiver functions, the 1D V_s models variations with depth (black where derived from joint inversion, gray where derived from the Rayleigh wave inversion), and 2D image of shear-wave velocity cross-sections. The white circles with an error bar on the tomograms indicate the Moho depths and the solid

white line shows the 3.1 km s^{-1} contour. The 1D V_s models are plotted for depths down to 40 km to indicate the sedimentary cover (red transparent area) along different profiles. The focal mechanisms over-plotted on the cross-sections are from Karasözen et al. (2019) and Wimpenny and Watson (2021), and the black dots show earthquakes with magnitude 5 and greater occurred between 2000 and 2020 from the EHB catalog. Abbreviations are mentioned in Fig. 1.

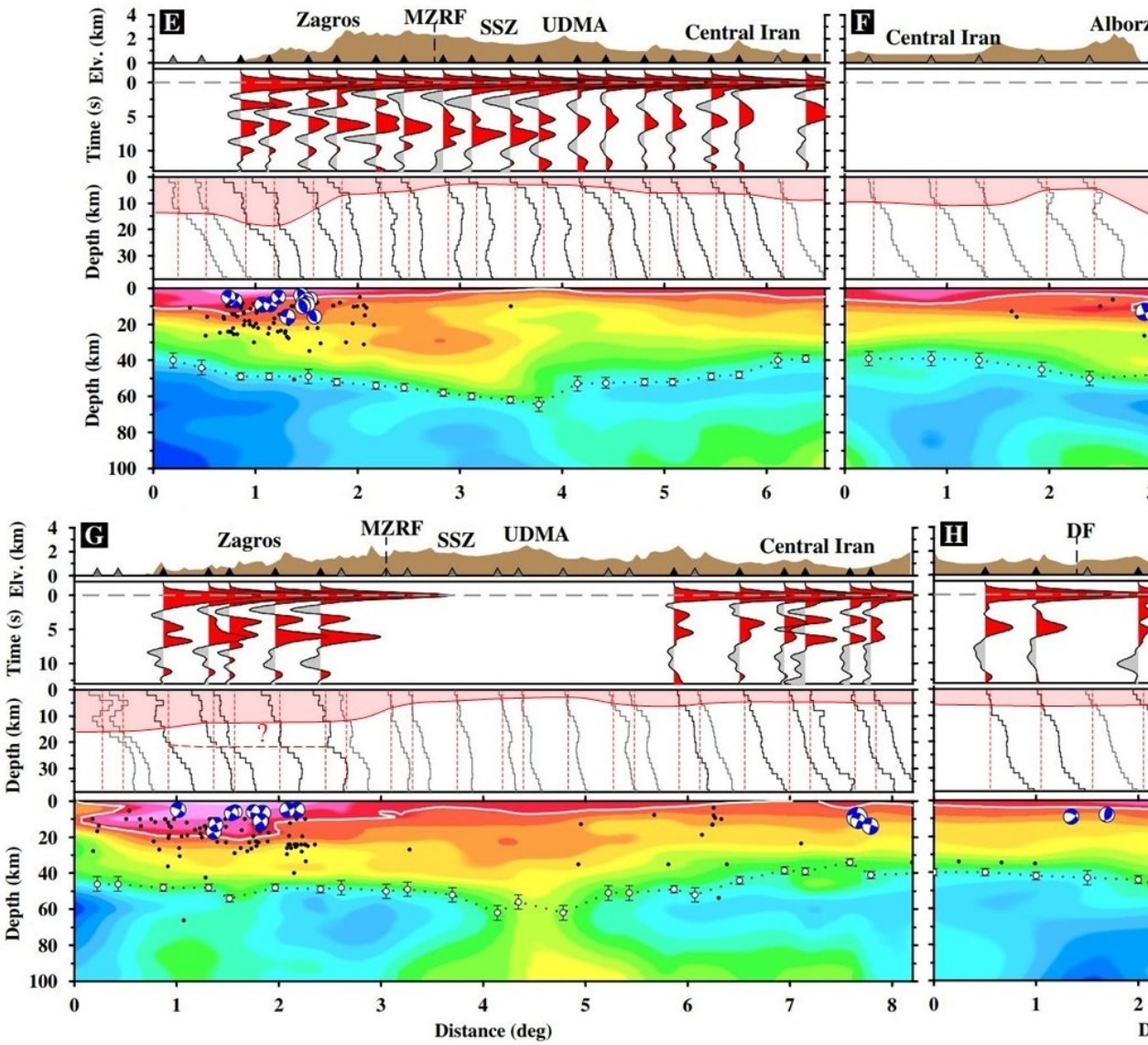

Figure 9. (Continued)

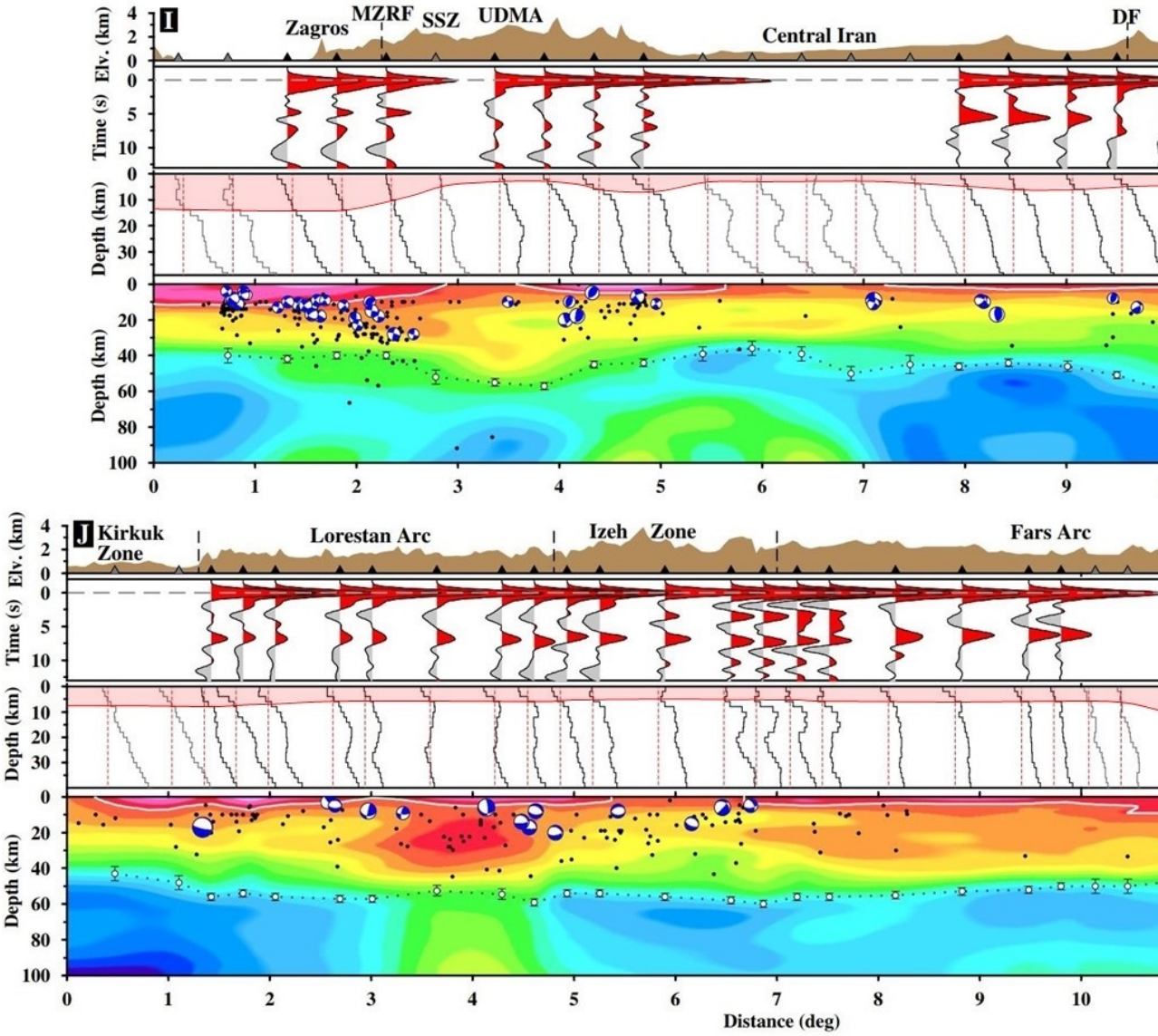

Figure 9. (Continued)

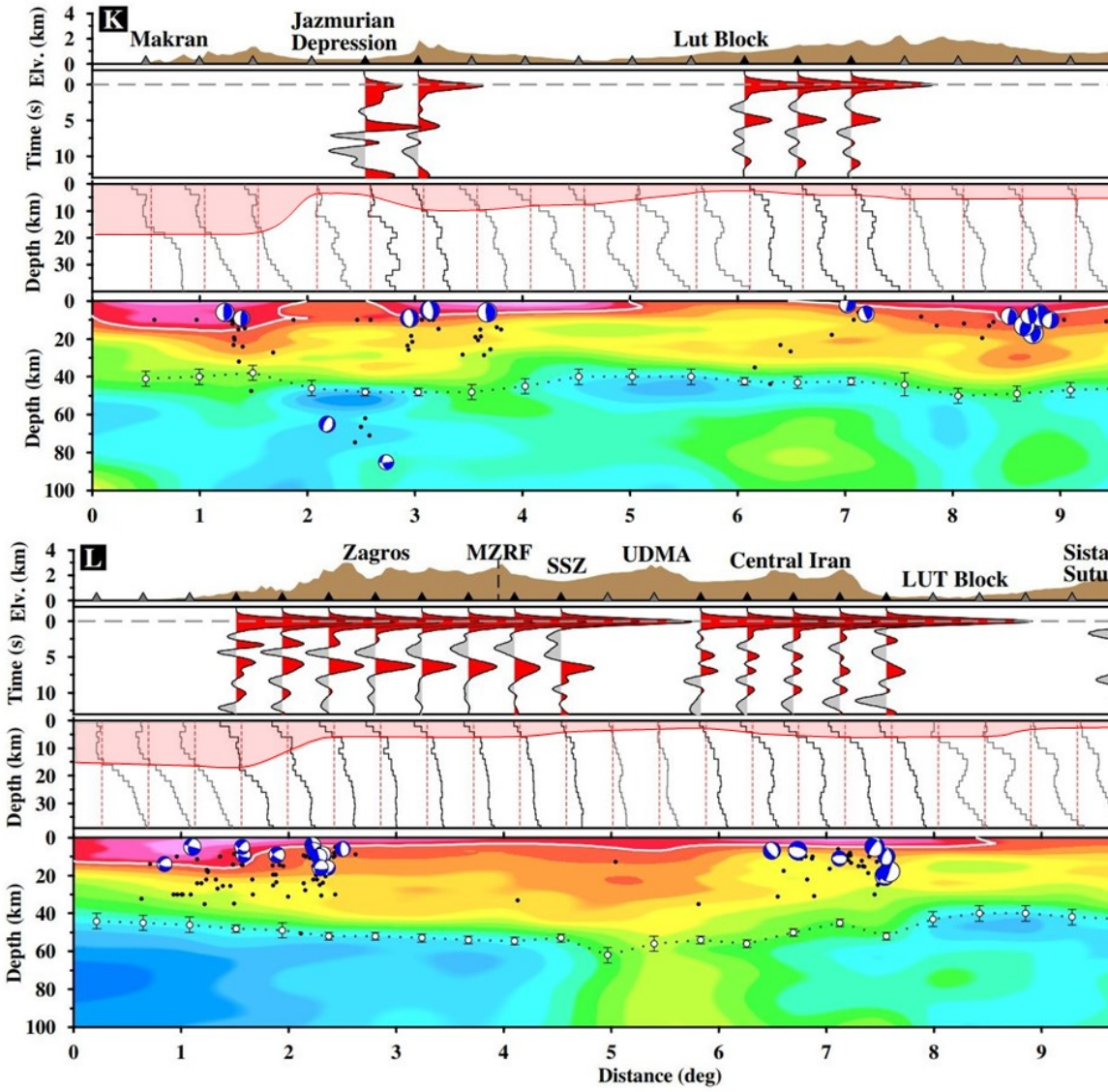

Figure 9. (Continued)

5 Discussion

We jointly inverted the *P*-wave receiver functions and Rayleigh wave group velocities to obtain an updated image of the crust and uppermost mantle V_s structure of the Iranian Plateau. Our high-resolution maps are a significant im-

provement over previous studies (e.g., Shad Manaman & Shomali, 2010; Shad Manaman et al., 2011; Mohammadi et al, 2013a, 2013b; Motaghi et al., 2015; Mortezanejad et al., 2018; Kaviani et al., 2020) revealing more structural detail. We used the 1D V_s velocity models along the profiles in Fig. 9 to estimate the thickness of the sediments in different parts of Iran. A detailed analysis of the velocity models for the thickness of sediments is beyond the scope of the current study. Instead, we used some simple criteria to obtain approximate values. In regions of sedimentary basins we looked for strong gradients of V_s from below 3.0 km s^{-1} to above 3.0 km s^{-1} to constrain the base of the cover. This pattern frequently occurs in the Zagros fordeep, the South Caspian and the Makran regions. In regions of more gradational velocity variation (such as in the Alborz), we chose the depth to V_s=3.1 km s^{-1} as the base of the sediments. In the magmatic regions of SSZ, UDMA and central Iran, the shallowest velocities are rarely less than 3.0 km s^{-1}. In those regions we assumed that the sediment thickness is very small (only a few kilometers at most). The middle panels of Fig. 9 show the variations of sediment thickness superimposed on the velocity models. In drawing the sediment profiles we tried to maintain consistency between neighboring stations and between intersecting profiles.

Below, we discuss some of the geophysical and geodynamic implications of our findings in different tectonic regions of the Iranian Plateau.

5.1 Crustal structure

5.1.1 The Zagros Collision Zone

Various geological and geophysical studies have shown thick sedimentary cover (maximum of 14 km) overlying the Precambrian basement of the foreland basin and the fold-and-thrust belt of the Zagros. One of the early estimates by Colman-Sadd (1978) puts the thickness of the Cambrian-to-Pliocene sedimentary succession of the SFB at 12 km. Blanc et al. (2003), through balanced cross-sections in the Lorestan and Dezful regions, determined basement depths of 12 and 10 km, respectively in the Zagros Foredeep. Sherkati et al. (2006) constructed several cross-sections from active seismic data and estimated a sedimentary cover of 10-12 km in the foreland of the central Zagros, decreasing to about 8 km towards the High Zagros. According to Alavi (2007), the sediment cover is 10 km in Lorestan and 7 km in Fars. Emami et al. (2010) and Verges et al. (2011) estimated the total stratigraphic column above the basement to be around 13 km in the Lorestan region. Hatzfeld et al. (2003), using receiver function analysis, found an 11-km thick sediment layer (V_p=~4.7 km s^{-1}) in the interior of the Zagros in the Fars region.

Our profiles across the Zagros (Fig. 9, profiles, A, B, C, E, G, and I) show very thick sediment cover in the southwestern margin, decreasing beneath the High Zagros, and thinning out beneath the SSZ and UDMA. The sediments of the Zagros reach their maximum thickness in the western and southern margins of the Lorestan Arc, the Dezful Embayment, and in the Fars Arc, exceeding 15 km in these areas, even reaching to about 20 km in the southern Zagros (Profile G).

Based on analysis of aeromagnetic data, Teknik and Ghods (2017) suggested a magnetic basement as deep as 16 km everywhere in the Loresten and Izeh zones. If the sedimentary cover does not contain volcanic lithology (which is the case in the Zagros), the depth of the magnetic basement can provide a lower-bound estimate for the depth of the igneous basement and constrain the thickness of the sedimentary cover. The estimated magnetic basement is 2-4 km deeper than the base of the sediment cover proposed by other studies. This could be due to errors in magnetic depth calculations. But, it is interesting to note that our shear wave velocity model also predicts sediments deeper than previously estimated in the southern margin of the Lorestan Arc. A recent study by Abdulnaby et al. (2020), used a joint inversion of Rayleigh group velocities and receiver functions to constrain the depth of Moho and sedimentary cover in the Mesopotamian Foredeep and the southwestern margin of Zagros in Iraq. They showed very thick sediments, 16-17 km deep in the foredeep region in southern Iraq very close to the endpoints of profiles B and C, where our estimates of the sediments are 18 and 16 km, respectively. The geodynamic model by Abdulnaby et al. (2020) presents an abnormal crustal root under the Mesopotamian Plain and the Zagros in SE Iraq, initiated by the repeated rifting of the NE margin of Arabia during the Mesozoic. The continued sedimentary loading and subsidence throughout the Cenozoic enhanced the sinking of the crust into the upper mantle and developed a thick sedimentary basin in front of the Zagros Foredeep.

In the NW and central Zagros (Fig.9, profiles A, B, C and E), the Moho (shown by white circles with error bars) starts at around 40-45 km in the SFB and increases gently by about 5-10 km towards the High Zagros. In the southern Zagros (profiles G and I) the Moho appears to be fairly flat at about 40 to 50 km under the entire fold-and-thrust belt. The deepest Moho is observed in the NW and central Zagros (profile J) where the width of the mountain range is narrower, while in the broader region of the belt in the south, the Moho is shallower by about 5-7 km. The Moho reaches its greatest depths of 55-65 km north of the MZRF beneath the SSZ in central Iran (Fig. 8d). Upon crossing into UDMA and the interior of central Iran, the Moho again shallows by about 10 to 20 km over a distance of 100 km or so. These results are in agreement with the reported Moho depths from P receiver function analyses by Paul et al. (2006, 2010) along two cross-sections near profiles B and E of our study. The pattern of V_s variations along the Zagros profiles reveals the internal structure of the crust in the collision zone. In the Lorestan Arc (profiles A and B), a tongue-shaped low-V_s feature (3.1-3.5 km s^{-1}) dips northeastward, starting at shallow depths south of the MRF and extending to lower-crustal depths beneath the SSZ and UDMA where the Moho reaches its greatest depth. This low-velocity zone is roughly parallel to the profile of the Moho beneath it. It is present in the Izeh Zone in the central Zagros (profile C), albeit with less clarity probably because it appears as a weaker, but steeper anomaly right beneath the SSZ. In the northern and southern Fars Arc (profiles E and I), the dipping structure has a clear expression beneath MZRF, but in central Fars

(profile G) it is very broad, extending far north well under UDMA. In places such as the NW Zagros, where the structure extends to a greater distance under central Iran, the advancing part of the structure flattens above the Moho. The presence of a low-V_s zone in between higher V_s zones at mid-crustal depths indicates a major low-strength shear interface whose asymmetrical geometry reveals the underthrusting of the crust of the Zagros beneath the crust of central Iran. The dipping high-to-low V_s interface can be taken as the depth expression of the MZRF. This configuration confirms that the MZRF is a major crustal-scale boundary separating the Arabian margin from central Iran. The 20-25-km crustal thickness difference between the SSZ and Zagros indicates that the crust of SSZ has almost doubled as a result of underthrusting. The common-conversion-point (CCP) depth-migrated cross-section calculated by Paul et al. (2010) in the NW Zagros (near profile B) shows a double polarity (a negative followed by a positive) wavelet that dips northeastward, crossing the crust from the surface trace of MZRF to Moho depth beneath the UDMA. This signal arises from a low-V_s layer overlying a higher V_s one, and is a clear indication of the trace of the MZRF at depth. Paul et al. (2010) did not observe an unambiguous expression of the same wavelet feature in the south-central Zagros, possibly due to insufficient data. Our shear-wave velocity maps, however, show that the low-V_s dipping feature is present everywhere in the Zagros, and that the MZRF plays a prominent role in the underthrusting of the Arabian crust beneath central Iran.

The Fars Arc with a comparable crustal shortening to that of the NW Zagros (50-65 km was estimated by Sherkati et al., 2006; 65-78 km by Mouthereau et al., 2007; 67 km by McQuarrie et al., 2003), and shows more extended thin-skinned deformation in the ZFTB. Although, from the V_s model of this region (profiles E and G), the dipping low-V_s anomaly is visibly similar to what we see in the NW Zagros; there are, however, some differences. In comparison with the NW Zagros, in the Fars it seems that the angle of Arabian underthrusting is steeper; the crust is thicker under the SSZ (65 km at maximum) and drops to 50 km and less under the UDMA and central Iran. The V_s model does not indicate a gently sloped underthrusting of the Arabian crust under central Iran, instead we observe a sharp bulge-shaped root of the Arabian Plate under the central SSZ, forming a Moho step (15 km).

The Bouguer gravity anomaly map of Iran (Fig. 8f) shows a 200 mgal minimum over the MZRF and High Zagros. Using gravity observations, Snyder and Barazangi (1986) found that the crustal thickness attains its maximum thickness under the High Zagros. Paul et al (2006, 2010) proposed a model of crustal-scale underthrusting of the Arabian crust under the SSZ to reconcile the Moho depths estimated from receiver functions with the gravity observations. This model proposes a doubling of the dense lower crust beneath the SSZ which compensates for the negative Bouguer anomaly and also shifts the anomaly southward over the High Zagros to match the observations.

A recent regional P and S waves tomography by Talebi et al. (2020) revealed an

elongated crustal low-velocity anomaly that slopes gently northeastward under the NW and central Zagros and SSZ. Talebi et al. (2020) proposed that this layer and the higher-velocity layer beneath it represent the felsic and mafic parts of the Arabian crust, and as the Arabian margin underthrusts central Iran, its felsic layer forms a lower-crustal channel beneath the Iranian crust. This crustal architecture bears similarities to the internal structure of the crust in our model. There are, however, differences between the two models. The low-velocity zone in the model of Talebi et al. (2020) is deeper by about 10-20 km than the corresponding structure in our model. Its base reaches to Moho depth as estimated by our model and other models available in the literature. In order to fit the lower high-velocity layer into the lower crust, Talebi et al. (2020) argued that the Moho under the Zagros should be at least 10 km deeper than previous estimates, e.g., close to 50-60 km. We disagree with their conclusion as our V_s models clearly put the Zagros Moho in the 45-50 km range and the low-V_s dipping layer in the 10-40 km depth range.

Pillia et al. (2020) used an inversion of seismic noise data in the 2-40 s period range image the V_s structure of the SE termination of the Zagros where continental collision transitions to subduction. Their geometry for the sedimentary cover of the ZFTB is very similar to what our model shows (Fig. 9, profile I), but due to poor raypath coverage, their model did not adequately resolve the crustal underthrusting beneath central Iran. The 2D V_s model along profile I clearly shows a low-V_s anomaly dipping at a shallow angle beneath central Iran, revealing the geometry and extent of the Arabian underthrusting. In the SE end of Zagros, unlike the other parts, seismicity does not die out under the High Zagros (compare profile I with other profiles), but in a deepening trend, diffuses further north under the SSZ (Engdahl et al., 2006; Yamini-Fard et al., 2007; Nissen et al., 2011, 2014). The locations of these deeper earthquakes match well with the low-velocity anomaly under the SSZ and UDMA. Our model is also consistent with the crustal model of Yamini-Fard and Hatzfeld (2008) in which the crust thickens from ~45 km in the SE Zagros to ~53 km under the MZRF. Considering the ~45 km long-term shortening in the SE Zagros (Molinaro et al., 2004), its younger collisional age, and the strong correlation between the dipping low-V_s structure and seismicity under the MZRF and SSZ, we conclude that the active underthrusting of the Arabian Plate under central Iran in the Zagros-Makran transition zone reflects the earlier phases of the northern-central Zagros collision.

The Moho depth map (Fig. 8d) indicates that the thickened crust along the SSZ and UDMA varies in thickness and width from NW to SE. In the center of the collision zone, the thickest crust (60-65 km) of the Iranian Plateau is predominantly localized under the SSZ (within ~150 km width), but in the NW part of the collision, the thickened crust (55-60 km) varies quite smoothly beneath the SSZ and UDMA (within ~250 km-width). Paul et al. (2010) found that the zone of crustal thickening under the SSZ is a wider region in the NW Zagros (320 km) than in the central Zagros (170 km). This difference in width is also visible in the Moho map of Kaviani et al. (2020) (Fig. 10c). Based on

the V_s structure of the collision zone in the Lorestan Arc (Fig. 9, profiles A and B) and in the central Zagros (profiles C and E), a summary schematic of the lithospheric structure for the Zagros collision is shown in Figure 11. It illustrates how the difference in the slope of underthrusting controls crustal thickening in central Iran in terms of width and depth.

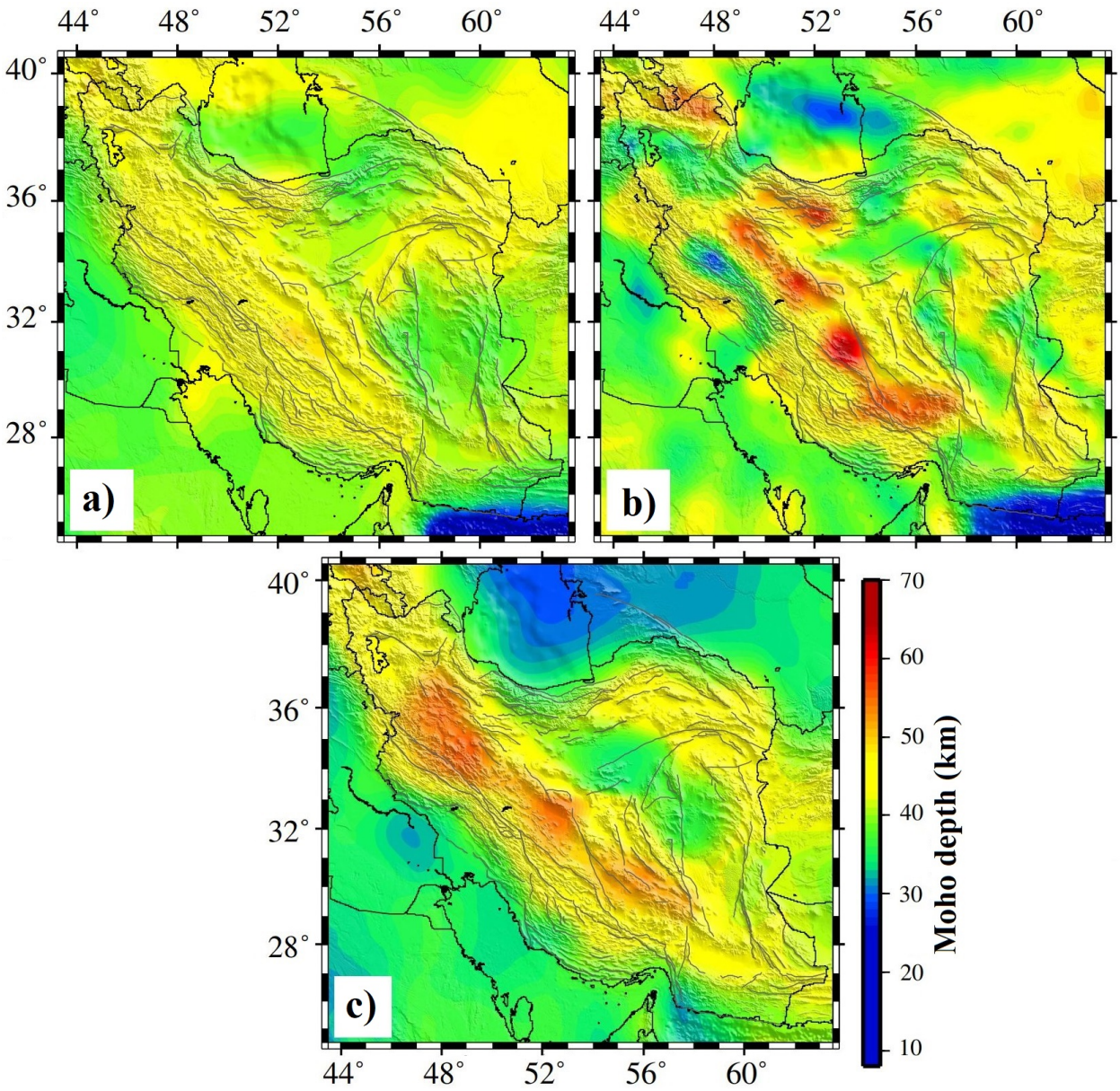

Figure 10. a) The Crust1.0 Moho map (Laske et al., 2013). b) The Moho

map presented by Shad Manaman et al. (2011). c) The Moho map presented by Kaviani et al. (2020).

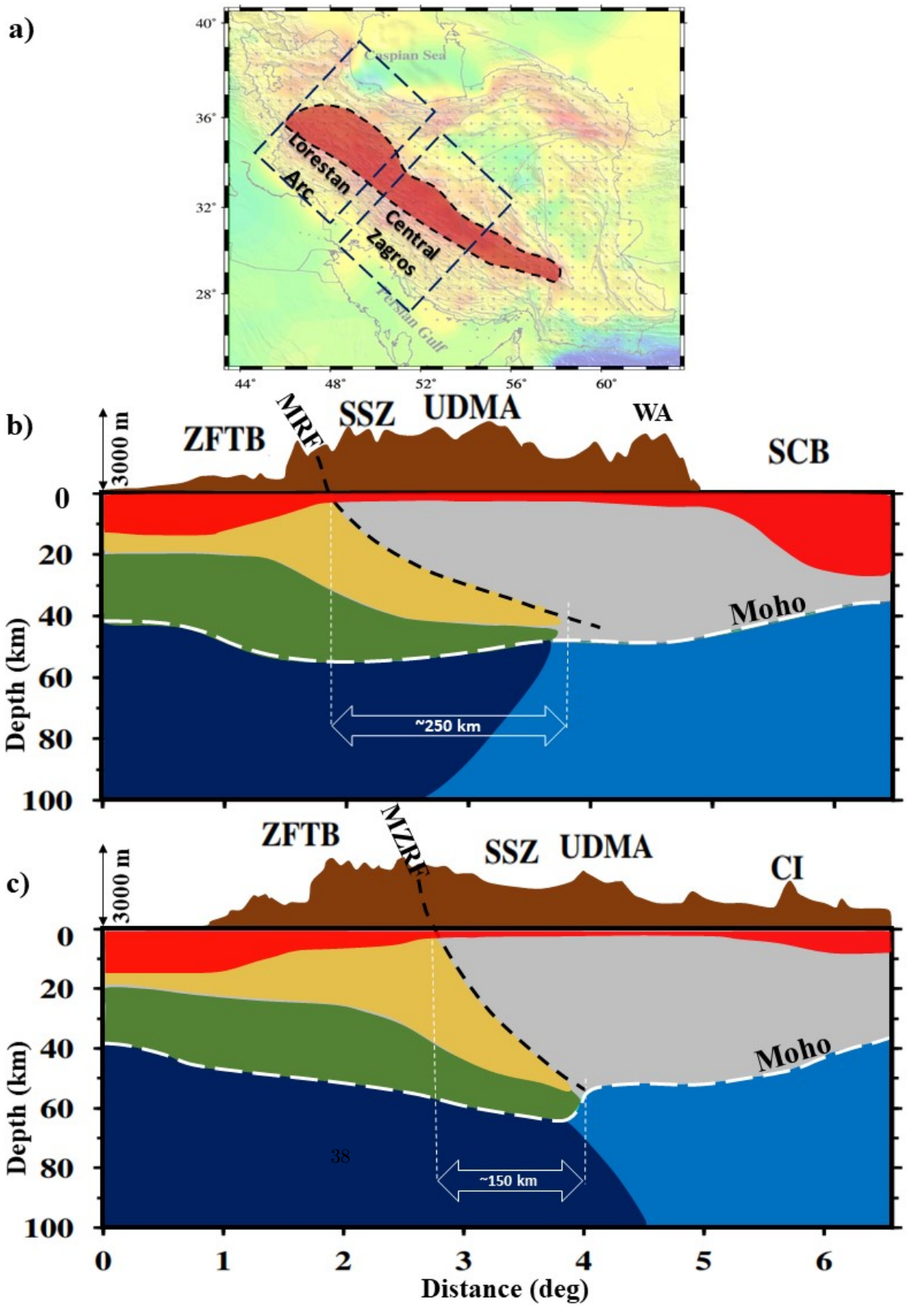
a)
40°
36°
32°
28°
44°
48°
52°
56°
60°
Caspian Sea
Lorestan
Arc
Central
Zagros
Persian Gulf
b)
3000 m
ZFTB
MRF
SSZ
UDMA
WA
SCB
Moho
~250 km
Depth (km)
0
20
40
60
80
100
c)
3000 m
ZFTB
MZRF
SSZ
UDMA
CI
Moho
~150 km
Depth (km)
0
20
40
60
80
100
0
1
2
3
4
5
6
Distance (deg)

Figure 11. a) Variation in the width of the thickened crust along the SSZ and UDMA (the red colored area surrounded by a dashed line). The boxes indicate the Zagros collision zone in the Lorestan Arc and central Zagros. b-c) Summary schematics of the lithospheric structure for the Zagros collision in the Lorestan Arc (b) and central Zagros (c) (vertical exaggeration: 2x). Note – the topography and main structural features of the schematics for the Lorestan Arc and central Zagros are according to profiles A and C (Fig. 8b and fig. 9), respectively. Colors are: brown (topography), red (sedimentary cover), yellow (Arabian upper crust), green (Arabian lower crust), gray (central Iran crust), dark blue (Arabian uppermost mantle), and light blue (central Iran uppermost mantle).

5.1.2 The Makran Subduction Zone

One of the significant features of the Makran Subduction Zone is its vast and thick accretionary wedge, that stands out from typical subduction zones of the world (e.g., White & Louden, 1982; Kopp et al., 2000; Shahabpour, 2010). The deformation front of the subduction is located in the Oman Sea (at about latitude 24° N). Our V_s model covers the western Makran, between the ZMP fault system and the Iran-Pakistan border (Fig. 1). Profile K of Fig. 9 crossing near the western end of the subduction zone reveals the large-scale geometry of the accretionary wedge characterized by a low-V_s feature (~<3.3 km s^{-1}) gently dipping north to about 25-30 km depth just under the south of the Jazmurian Depression. Underneath the sedimentary wedge a flat Moho at 40 km depth extends to the southern edge of Jazmurian. A recent receiver function/surface wave analysis by Priestley et al. (2022) along a south-north transect in the region of Chabahar (longitude of 60.5°E) revealed a very similar structure as well. Their study shows that the coastal region is underlain by a very thick low-V_s (<3.2 km s^{-1}) sedimentary cover in excess of 22 km, and a 6-8 km-thick gradient zone above a 100 km-thick high-velocity upper mantle. The base of the gradient zone (corresponding to the oceanic Moho) has a shallow 4±2° northward dip. Offshore, south of the shelf, the accretionary prism is observed to be 7 km or more thick (e.g., White & Louden 1982; Kopp et al. 2000). In the coastal Makran, Motaghi et al. (2020) suggested that the base of the accretionary wedge is gently deepening from 9 to 15 km within a 60 km distance of the shoreline. Penney et al. (2017) found the sedimentary section to be ~26 km thick in the same region. An active-source seismic survey from the coastline to the southern Jazmurian Depression by Haberland et al. (2020) estimated a maximum thickness of ~35 km for the accretionary wedge.

Previous studies suggest a crustal thickness of ~20-33 km for the coastal Makran (Abdetedal et al., 2015; Abdollahi et al., 2018). Our Moho map shows that in the coastal Makran, the Moho exhibits considerable undulations (Fig 8d). Near the Zagros-Makran boundary, where the transition from continental Zagros to oceanic Makran occurs, the Moho is at >40 km depth. Towards the east, the Moho gently shallows to about 35 km before abruptly decreasing to 30 km in the region of Chabahar, in agreement with Priestley et al. (2022). Further east,

the Moho again deepens to about 35 km. The gentle northward Moho variation seen under the coastal Makran is in agreement with the low-angle dip of the Arabian Sea Plate below the accretionary complex (for the seaside: White and Louden, 1982: $<2^\circ$, Kopp et al., 2000: 3°; for the coastal side: Motaghi et al., 2020: $<2^\circ$, Haberland et al., 2020: $\sim 8^\circ$; Priestley et al., 2022: $\sim 4^\circ$).

The Jazmurian Depression is a fore-arc compressive basin sitting above the subduction zone (Farhoudi & Karig, 1997; McCall, 1997) and is probably a remnant of the older Nain-Baft back-arc basin in the eastern Iranian Plateau (Burg, 2018). The basin is positioned between the volcanic arc of the subduction zone in the north and the accretionary prism in the south. The low relief of the basin suggests it has undergone thermal subsidence in the latter stages of its development, as evidenced by shallow marine sedimentation in the Eocene (Burg, 2018). The older sedimentary rocks are now capped by unconsolidated Quaternary deposits (McCall, 1997; Burg, 2018). Our understanding of the subsidence history of the basin is quite preliminary, but it seems that a significant part of its development has taken place since the Pliocene (McCall & Kidd, 1982; McCall, 1997). According to recent geodynamic reconstructions, it is suggested that the depression is floored by oceanic crust and uppermost mantle (Burg, 2018; Monsef et al., 2019).

The V_s structure of the depression in Fig. 8 and profile K of Fig. 9 shows velocities higher than the neighboring regions to the south and north. The shallowest V_s are 3.3 km s^{-1}, which indicates that the sediment cover of the basin is rather thin (a few kilometers at most). This implies that the basin has witnessed a prolonged period of low deposition prior to the Quaternary influx of unconsolidated sediments. Based on our knowledge of slab geometry east of the Jazmurian (Priestley et al., 2022), we expect the subducting plate to have a shallow dip beneath the Jazmurian as well, and we interpret the interface shown between 40-47 km in profile K to be the base of the subducting oceanic crust. The base of the Jazmurian Block above the subducting plate is hard to recognize in the profile, but it might be denoted by the narrow high-V_s zone around the depth of 30-35 km. Shad Manaman et al. (2011) and Abdollahi et al. (2019) estimated a Moho depth of 37, and 40 km beneath the Jazmurian Depression, respectively. Neither study, however, specified whether the inferred Moho is oceanic or continental.

Below the volcanic arc in the mantle wedge of the subduction zone, we observe anomalously low-V_s from upper-crustal to sub-Moho depths (Figs. 7 and 8). In this region Priestley et al. (2022) found a sub-Moho V_s of 3.75 km s^{-1} in the 50-80 km depth range. They suggested that their observed S-wave velocity and the P-wave velocity of ~7.75 km s^{-1} (Al-lazki et al., 2014) gives about 20% serpentinisation of the mantle wedge, which is typical of other subduction zones (e.g., Hyndman & Peacock, 2003) and implies ~1-2% partial melt in the depth range where the arc magmas are generated in the mantle wedge. The magmas then percolate towards the surface into the overlying crust and lower the seismic velocity as seen in our models (Figs. 7 and 8).

5.1.3 Central Iran and the Lut Block

Central Iran's stable and relatively aseismic blocks are surrounded by active strike-slip fault systems (Berberian et al., 1999; Walker et al., 2003, 2004; Walpersdorf et al., 2014) (Fig. 1). These blocks are relatively flat terrains with altitudes mostly less than ~1000 m. Our station coverage in eastern Iran is sparser than in other regions (Fig. 2). Nevertheless, dense surface wave path crossings over the region (Fig. 3) enabled us to achieve a reliable velocity model and constrain the subsurface structure.

Given the direct relationship between the lowest shear velocities in the upper crust with sedimentary basins, the V_s maps show regions of thick sediments in central Iran and the Lut Block. Profiles A and B of Fig. 9 traverse the northwestern margins of central Iran. The contrasting low-V_s (~3.1-3.3 km) anomaly in the upper crust of the northwest UDMA extending towards the Talesh Mountains (profile A) overlies the high-velocity mid-crust. Further to the east, along profile B, a lower V_s feature extends to the middle crust (~30 km) under the UDMA. Motaghi et al. (2018) used teleseismic P and S waves to study the lithospheric velocity structure in the western Alborz (between profiles A and B of this study). They observed a shallow low-velocity feature under the northern edge of central Iran, implying a sedimentary cover. Sedimentary basins, mostly ranging between 10 and 15 km thick, occur in the north of the SSZ-UDMA (Teknik & Ghods, 2017).

The sedimentary basins of the Great Kavir and the southern Lut Block reach a maximum depth of ~10 km (Fig. 9, profiles D and F). Tekink and Ghods (2017) estimated the deepest basins of central Iran to be around 15 km, but other studies found them to be not more than 10 km thick (e.g., Soffel & Forster, 1984; Morley et al., 2009; Mousavi & Ebbing, 2018). There is a band of low-velocity anomaly extending from the southern Lut Block to the Tabas Block (Fig. 7a) This thin strip of sediments is also detected in the recent potential field data analyses on the Iranian Plateau (Tekink & Ghods, 2017; Mousavi & Ebbing, 2018).

At depths of 40-50 km, there is a sharp shear wave velocity contrast (Fig. 7) between central Iran and the surrounding orogenic belts. At these depths, the regions of low-topography in central Iran show V_s>4 km s^{-1}, representing the sub-Moho structure, while the high-topography mountain regions show lower V_s values representative of the lower crust at the same depth. Other evidence also suggest that the crust of the central Plateau is thinner (e.g., Sodoudi et al., 2009; Motaghi et al., 2012) compared to the deforming belts (e.g., Paul et al., 2006, 2010; Radjaee et al., 2010; Motaghi et al., 2012; Wu et al., 2021). The crustal thickness of the interior of central Iran and the Lut Block varies mainly between ~34 and ~45 km (Fig. 8d and Fig. 9, profiles E-F, G-H, I, and K). Within the Lut Block, the crustal thickness varies smoothly from ~37 km in the central part (profile I) to ~45 km in the northern and southern ends of the microplate. A recent S-wave receiver function study by Wu et al. (2021) in eastern Iran revealed a shallow Moho of 35-40 km beneath the central and northern parts of

the Lut and a slightly deeper Moho 40-45 km beneath the Sistan Suture Zone. The Moho depth in the margins of central Iran in our model reaches ~50 km. The previous Moho depth measurements based on receiver function analysis in central Iran are in agreement with the results of our study (Sodoudi et al., 2009; Motaghi et al., 2012).

Fig. 8d and profile K of Fig. 9 indicate that the greatest Moho depth (51 km) in the Lut Block vicinity occurs under the northern end of the Sistan Suture Zone, a seismically active orogenic belt (~700 km long) in eastern Iran. The Sistan Zone, now trapped between the Lut and Helmand Blocks, was once a back-arc domain of the Neo-Tethys that closed off in the early Cenozoic during an east-directed subduction (Tirrul et al., 1983; Fotoohi Rad et al., 2005; Angiboust et al., 201). It was formed during an accretionary process in the subduction zone and contains several disrupted ophiolitic belts (Tirrul et al., 1983)). In our V_s maps, the Sistan Zone appears mostly as a relatively low-velocity region at crustal and sub-crustal depths. Its southern end shows more pronounced low velocities because here the zone is situated on top of the mantle wedge region of the Makran Subduction. The somewhat thicker crust of the northern Sistan Zone may be a consequence of its convergent regime; Jentzer et al. (2017) suggested, based on inversion of fault kinematic data, that the stress field of the region (Neogene to present) has been compressional with a $>60^{o}$ counterclockwise rotation, from 90^{o} N during the Middle-Late Miocene to 25^{o} N during the Plio-Quaternary. This long-term compressional regime, from the closure of a N-S extension of the Neo-Tethys to the present day, results in shortening/thickening of the northern Sistan Zone, where its topography and Moho depth exceed 2000 m and 50 km, respectively.

The increasing shortening ratio from the NW Zagros to Makran leads to a significant N-S shear between central Iran, the Lut Block, and the Helmand Block (Berberian et al., 1999; Vernant et al., 2004a; Khorrami et al., 2019). This shear convergence, and consequently the seismicity, is mostly accommodated by strike-slip faults between the blocks of eastern Iran (Berberian et al., 1999; Walker et al., 2004; Engdahl et al., 2006; Walpersdorf et al., 2014; Khorrami et al., 2019). The velocity model of central Iran is laterally more or less constant, especially in the mid-to-lower crustal medium where V_s gradually changes from ~3.6 to 4 km s^{-1} (Fig. 9, profiles E-F, G-H, I, K, and L). The less deformed microplates forming central Iran and the Lut Block, and the mostly localized seismicity on the strike-slip faults of the region, imply that a rigid block model is capable of explaining the deformation in eastern Iran (Walpersdorf et al., 2014).

5.1.4 Northern Iran

During the process of Arabia-Eurasia convergence, the rigid SCB has played a significant role in the formation and orientation of the surrounding seismically-active orogenic belts of the Caucasus, Talesh, Alborz, and Kopet Dag (e.g., Berberian, 1983; Priestley et al., 1994; Jackson et al., 2002; Brunet et al., 2003; Hollingsworth et al., 2008; Aziz Zanjani et al., 2013). The Alborz region trapped between the southern Caspian and central Iran accommodates roughly a quarter

of ~20 mm yr^{-1} N-S convergence between Arabia and Eurasia (Vernant et al., 2004b; Djamour et al., 2010).

5.1.4.1 NW Iran

In NW Iran, the V_s model of the upper crust (Fig. 8a) does not show V_s anomalies as low as in the surrounding areas such as the Kura Basin (Fig. 1) in the north, the SCB in the east, and the SFB and Zagros Foreland Basin in the south. The Kura Basin shows a significantly low V_s (2.7-3 km s^{-1}) structure implying a sedimentary cover of more than 15 km thickness. The shallow crust of the N-S tending Talesh changes laterally from the north to the south (Fig. 7a-b, 8a). The northern Talesh is a lower V_s (~3.2 km s^{-1}) region than the southern part (~3.5 km s^{-1}). Therefore, thicker sediments characterize the northern Talesh. However, the deeper levels of the crust under the Talesh have a uniformly high wave-speed (V_s =~4 km s^{-1}, Fig 7c-d). The high-velocity anomaly extending from the lower crust of western SCB to under the Talesh Mountains (at about 30-40 km depth in Fig. 9 profile A) was already reported by Bavali et al. (2016) and Mortezanejad et al. (2018). Given the westward motion of the SCB (e.g., Priestley et al., 1994; Jackson et al., 2002), the high V_s in the lower crust indicates underthrusting of the basement slab of the basin beneath the Talesh. Aziz Zanjani et al., (2013) revealed an active seismicity pattern in the Talesh with hypocentral depths between 20 and 40 km (the cross symbols in profile A). Their results showed a limited amount of underthrusting. The high-V_s anomaly correlates well with the lower crustal boundary between the SCB and the Talesh and it shows that the underthrusting under the Talesh is indeed not extensive.

The crustal thickness in NW Iran does not show great variations (Fig. 8d). The Moho depth in the western part (eastern Anatolia) is a little less than in the eastern regions (Sabalan and Talesh), varying between ~45 and 53 km. Taghizadeh-Farahmand et al. (2010) also reported the same eastward deepening of the Moho in the central part of NW Iran, but with a steeper slope (38.5 to 53 km). Based on V_s changes with depth, Mortezanejad et al. (2018) calculated a deeper Moho in the Talesh (53 km) than in NW Iran and SCB (~46 km).

5.1.4.2 The Alborz

The central-western Alborz Mountains are a higher V_s region compared to the eastern Alborz. The area covering the eastern end of the Alborz, Binalud, and the western Kopet Dag, shows low-V_s in the shallow upper crust (Fig. 8a and Fig. 9, profiles F and H), which can be attributed to sedimentary covers of about 7-10 km. Tekink and Ghods (2017) identified a number of basins along the eastern Alborz-western Binalud Ranges, but did not show any extensive basins in the western Alborz.

At both the western and eastern ends of the Alborz Mountains, where the range transitions into the Talesh and Binalud Mountains, respectively, the crustal thickness is about 45 km, which is the thinnest under the whole range (Fig. 8d). This thickness is in the range of the central Iran Moho depths. In comparison, the crustal thickness is more than 50 km under most parts of the range and

reaches a maximum of 58 km under the central Alborz just east of the Damavand volcano. This result implies that, despite the belief that there is not a sufficiently thick crustal root beneath the Alborz (e.g., Dehghani & Makris, 1984; Kaviai et al., 2020), this orogenic belt definitely has a thicker crust than the non-deforming surroundings, i.e., central Iran and the SCB. Radjaee et al. (2010) employed a joint inversion of P receiver function and Rayleigh wave group velocity over the west-central Alborz. They obtained Moho depths ranging from 55 to 58 km, consistent with the depths we have estimated for the same region. Sodoudi et al. (2009), using P receiver function analysis, reported a crustal thickness of 51-54 km in the southern flank of the central Alborz. They estimated the Moho depth below the Damavand volcano to be ~67.5 km, whereas Abbassi et al. (2009) found the crust beneath the Damavand to be ~58 km thick.

One of the major points in the tectonics of northern Iran is the hypothesis of underthrusting of the SCB beneath the mountain ranges of northern Iran (e.g., Berberian, 1983; Priestley et al., 1994; Jackson et al., 2002; Allen et al., 2003; Tatar et al., 2007). According to this hypothesis, the South Caspian, being a low-relief rigid block (and probably of oceanic affinity), is trapped in the Arabia-Eurasia convergence zone and is overthrown from all sides. Profiles B, D, and F (Fig. 9) from west to east, transect the Alborz Mountains. On all three profiles the low-V_s sediment layer of the SCB appears to protrude beneath the coastal region almost horizontally. However, it does not show any indication of extending far under the mountain ranges. It is not clear if this geometry constitutes an underthrusting of the Caspian basement beneath the Alborz, especially since it is not associated with any deep southward-dipping seismicity beneath the Alborz, such as that observed in the Talesh region. It is possible that the structure merely reveals the flexure of the basement of the sedimentary basin under the load of the mountain range. Earlier, we showed stronger evidence for underthrusting of the South Caspian basement beneath the Talesh Mountains, but even there the extent of underthrusting is small. We infer from our velocity profiles that the current interaction between the SCB and the mountain ranges of northern Iran is too low to be a significant contributor to the overall convergence rate for the Iran region, a conclusion also reached by Guest et al. (2006).

A thick (~30 km) high-V_s (3.8-4.1 km s^{-1}) material characterizes the lower crust of the Alborz (Fig. 8b). This feature highlights the crustal structure in the central Alborz, but at the eastern end (Fig. 9, profile F), the crust/lower-crust becomes thinner and exhibits lower V_s. Figure 8b shows that the anomalously high-V_s lower crust appears beneath central-western Alborz. Hence, the thickened lower crust (thickened crust) in the central-western Alborz can imply two different accommodation systems of N-S convergence between central Iran and the SCB in the western and eastern Alborz. Given the V-shaped border of the South Caspian-Alborz, the GPS data analysis (Djamour et al., 2010) indicates that the eastern Alborz principally accommodates strike-slip deformation, while the western Alborz localizes compressional deformation by thrust faulting and shortening (Shabanian et al., 2012). In the western and central Alborz, the con-

vergence rate is about 5 mm yr^{-1} (Vernant et al., 2004b; Djamour et al., 2010), equivalent to a quarter of the overall Arabia-Eurasia convergence. Therefore, the shortening/thickening process in the central-western Alborz takes place by thrust faulting systems (Tatar et al., 2007) in the brittle upper crust and the ductile deformation (thickening) in the lower crust.

5.1.4.3 The Kopet Dag and Binalud Mountains

The NW-SE trending seismically-active orogenic belts of Kopet Dag and Binalud are separated from eastern Iran and the Lut Block by the E-W Doruneh Fault (DF) (Engdahl et al., 2006; Shabanian et al., 2009; Aflaki et al., 2019). The northern and southern sides of the DF show a remarkable difference in their V_s structure (Fig. 9, profiles H, and I). The uppermost crustal low-V_s anomaly (~<3.2 km s^{-1}) in the south of the DF is limited to ~5-10 km depths. In the Binalud and Kopet Dag, the low-V_s feature becomes more profound, and further to the north, beneath the southern Turan Platform (Fig. 1) characterized by the Amu Darya Basin, it reaches a maximum depth of ~15 km (Fig. 8a, and profile I). The thick (~10 km) sedimentary basins (Afshar-Harb, 1979; Lyberis & Manby, 1999; Robert et al., 2014; Teknik & Ghods, 2017), and the dense seismically-active faulting system of NE Iran (e.g., Hollingsworth et al., 2010b; Shabanian et al., 2012; Aflaki et al., 2019) characterize the low-V_s upper crust in NE Iran. This region accommodates ~5 mm yr^{-1} of the Arabia-Eurasia convergence, which is about 90% of the N-S motion of the Lut Block (5.7 mm yr^{-1}) towards Eurasia (Walpersdorf et al., 2014; Khorrami et al., 2019; Baniadam et al., 2019).

The DF is also a sharp boundary between central Iran and the northern orogenic belts in the lower crustal structure. Figure 8b shows that the mean lower crust of NE Iran is relatively high-V_s (3.8-4.0 km s^{-1}) and does not show noticeable lateral variations. However, the crustal thickness varies significantly, indicating a ~13 km variation within the distance between the DF and the Main Kopet Dag Fault. The Moho depth in central Iran and the Lut Block does not exceed 50 km, whereas it deepens to ~58 km in the north of the DF (under the Kuh-e Sorkh) and then drops to around 50-52 km and 45-48 km under the Binalud and eastern Kopet Dag , respectively. Along a seismic array, Motaghi et al. (2012) reported a crustal thickness of 55.5 km to the south of Binalud and 40.5-45 km in the Binalud and Kopet Dag. The S receiver function study of Wu et al. (2021) also showed that northward of the DF, the Moho progressivey deepens, reaching to 50-55 km under the Binalud-Kopet Dag system.

The thickened crust of NE Iran (Fig. 8d) is centered in an NW-SE band, parallel with and between the eastern DF and the Binalud Mountains but not beneath the eastern Kopet Dag, which is assumed to be the deformation front of central Iran-Eurasia convergence. To understand the crustal deformation process in NE Iran requires taking into account the present-day tectonic regime and the convergence accommodation mechanism of the Lut-Kopet Dag interactive complex (Mousavi et al., 2013; Walpersdorf et al., 2014; Khorrami et al., 2019; Aflaki et al., 2019; Baniadam et al., 2019). Baniadam et al. (2019) used inversion analysis of fault kinematics data to study the modern Plio-Quaternary stress field.

They suggest that, given the Lut Block's northward motion, the region between the Lut and Kopet Dag Mountains is divided into two main tectonic domains by the DF. The northern part, that is the NW-SE oriented Binalud and Kopet Dag, is characterized by the extrusion of fault-bounded blocks towards N-NW (Mousavi et al., 2013; Walpersdorf et al., 2014; Khorrami et al., 2019). In the southern part, between the NW-SE trending eastern DF and southern Kopet Dag, the stress field is NE-SW, and the Doruneh Fault acts as a reverse fault. Hence, the convergence is accommodated internally, leading to a crustal root in the ductile lower crust.

5.2 Moho depth variations across the Iranian Plateau

One of the principal results we have extracted from our inversion model is the crustal thickness variations across the region (Fig. 8d) derived from the sharp V_s changes at the crust-mantle transition depth. Here, the Moho map of this study is compared to the previous maps derived from V_s models of the Iranian Plateau (e.g., Shad Manaman et al., 2011; Kaviani et al., 2020) and the global crustal thickness map, CRUST1.0 (Laske et al., 2013).

In a general sense, there are strong correlations between the variations of topography (Fig. 1), crustal thickness (Fig. 8-d), Bouguer gravity anomaly (Fig. 8-f), and the distribution of the major fault systems (Fig. 1) across the Iranian Plateau. For the most part, the distribution of the negative Bouguer anomaly ranging between 150 and 220 mgal coincides with thick crust (~>50 km) throughout the Plateau. The low-anomaly (i.e. thick crust) regions, including the High Zagros, the SSZ and UDMA, and the Alborz-Binalud-Kuh-e Sorkh Ranges, surround the low-topography and thin crust (30-45 km) regions of central Iran and the Lut Block with anomalies in the a range of 25 to 100 mgal. This broad correlation indicates that the crustal thickness variation is the dominant geological feature associated with the Plateau's gravity observation.

The CRUST1.0 model (Fig. 10a) does not show significant variations in the crustal thickness of Iran and the changes are very smooth and have a long-wavelength variation. According to this model, the Moho depth in the Great Kavir, the Lut Block, and eastern Alborz is ~ 35-40 km and in the rest of the Plateau it is ~45-50 km. Our results and previous work (e.g., Paul et al., 2006, 2010; Radjaee et al., 2010; Motaghi et al., 2012; Kaviani et al., 2020), show that the range of Moho depth variation in Iran is ~30-65 km, significantly greater than what the global model estimates.

Shad Manaman et al. (2011) calculated a Moho map based on V_s structure using the partitioned waveform inversion. Their map (Fig. 10b), constrained with additional information from previous receiver function and refraction measurements, shows maximum crustal thickness (60-65 km) in a few local patches along the SSZ. In the Lorestan Arc of the Zagros they report an unrealistically thin crust of 30-35 km. In the eastern SCB, NW Iran, eastern Alborz, central Iran, Lut and Makran Subduction Zone they report crustal thicknesses less than 40 km, although in the Caspian region they have sparse coverage. Their model

underestimates the Moho depth in the NW Zagros, NW Iran, and eastern SCB. This model also does not show an along-strike continuous thickened crust under the SSZ and UDMA, whereas our model clearly shows that the thickened crust northeast of the Zagros Suture is a ubiquitous feature of the collisional front.

More recently, Kaviani et al. (2020) derived a Middle East Moho map from a 3D shear-wave velocity model from Rayleigh waves (Fig. 10c). In general, their map shows good agreement with our map with regards to large-scale structures in the Iranian Plateau. Both maps have the same $0.5^\circ \times 0.5^\circ$ resolution, but the map by Kaviani et al. (2020), being based on surface wave alone, produced a smoother crustal structure. For example, beneath the Zagros Suture zone, the Alborz and Kopet Dag, they estimated a thinner crust. On the other hand, in the Makran region and in the southwest coastal Caspian, where our model shows a thin crust in the order of 30-35 km, they obtained a thicker crust of ~40-45 km. The major discrepancy between our Moho map and that of Kaviani et al. (2020) is in the central Alborz and the SCB. Kaviani et al. (2020) estimated a shallow Moho of <40 km in the central Alborz, which is at least 10 km thinner compared to other studies that employed joint inversion methods (e.g., Radjaee et al., 2010; Rastgoo et al., 2018).

Another example of fine-scale structure captured by our map is in eastern Iran; our results suggest that the Doruneh Fault is a major fault zone separating two different crustal architectures on its opposite sides. The same is true in the Makran Subduction Zone, where our map has succeeded in revealing unprecedented detail of the crustal structure.

5.3 Sub-Moho structure of the Iranian Plateau

The period range of the surface wave used in this study provided the opportunity for investigating the sub-Moho structure (down to ~100 km) in the Iranian Plateau. The V_s of the uppermost mantle beneath the Iranian Plateau is mostly in the range of 4-4.3 km s^{-1} (Fig. 8c), which is similar to other comparable deforming regions such as the Anatolian Plateau (e.g., Maggi & Priestley, 2005; Koulakov, 2011; Salaün et al., 2012; Kaviani et al., 2020). The margins of the surrounding stable Arabian Plate and Turan Platform are characterized by significantly higher V_s of 4.5-4.9 km s^{-1}. In the Zagros, the subcrustal V_s values are generally high (V_s>4.2 km s^{-1}), implying a high-V_s uppermost mantle beneath the Zagros system (Koulakov, 2011; Priestley et al., 2012; Rahimi et al., 2014; Motaghi et al., 2015, 2017; Rahmani et al., 2019; Mahmoodabadi et al., 2019, 2020; Veisi et al., 2021). A low-V_s zone under the southern Lorestan Arc (Fig. 9, profile C) separates the central Zagros upper mantle from the northernmost Zagros. This anomaly is overlain by the low-V_s underthrusting Arabian crust under central Iran.

In eastern Iran, under the northern end of the Sistan Zone, both the crust and the uppermost mantle show low-V_s (Fig. 9, profile L). Based on S receiver function measurements and waveform modeling along a seismic array in eastern Iran, Wu et al. (2021) estimated more than 4% shear-wave velocity drop across

the lithosphere-asthenosphere boundary (LAB) at the north end of the Sistan Suture which possibly reflects the presence of partial melting in the mantle and melt migration upwards into the crust, thereby decreasing crustal V_s, comparable to the crustal/uppermost-mantle V_s in the Makran Volcanic Belt (Priestley et al., 2022).

Another large low-V_s anomaly in the uppermost mantle is observed in the southwestern part of the SCB, western Alborz, and NW of UDMA. Motaghi et al. (2018) observed low V_p and V_s anomalies beneath the Alborz-Talesh transition zone and interpreted it as the lithospheric boundary between the SW margin of SCB and southern Talesh Mountains. Rastgoo et al. (2018) investigated the uppermost mantle structure of the Alborz Mountains using recordings from seismic stations along the southern flank of the range. They reported the same low-V_s anomaly under western Alborz at a depth range of 50-100 km. They interpreted it as the result of post-collisional delamination of the lower part of the western Alborz lithosphere. Our results show that the extent of this low-velocity anomaly is much larger than the western Alborz region.

5.4 The Anisotropic patterns in the Iranian Plateau

Fig.4 shows projections of the fast axes of Rayleigh wave azimuthal anisotropy on the horizontal plane. The tomography results for the shortest periods sampling the uppermost few kilometers of the crust did not produce a measurable azimuthal anisotropy anywhere over the Plateau (Fig. 4). In the period range of 10-20 s, constraining the upper crust, the strength of anisotropy is generally low. The strongest and most coherent anisotropy is observed in the western Alborz, the NW Zagros, and north central Iran. It dies out towards the eastern Alborz and Kopet Dag. The eastern half of the Plateau and most of the Zagros region also shows a negligible anisotropy. In the NW Zagros and western Alborz, the fast directions are oriented NW-SE, perpendicular to the direction of shortening, and almost parallel to the major shear zones in that part of Iran. This is where the width of the collision zone is the narrowest and it is possible that the fabric of crustal anisotropy is governed by the oblique-shear regime, giving it a range-parallel direction. Djamour et al. (2010), through the analysis of GPS data, showed that the western Alborz Mountains are currently accommodating significant range-normal shortening, while in the eastern Alborz Mountains, the deformation is dominated by left-lateral motion. This contrast in deformational style between the western and eastern Alborz could explain the lack of noticeable anisotropy in the eastern Alborz. In the NW Zagros, Dashti et al. (2020) employed receiver function harmonics and determined a NE-SW-oriented *slow* axis of anisotropy in the upper crustal shear zone across the Zagros Suture. Their result is consistent with the NW-SE fast axes we observe for the surface wave anisotropy.

South of the Alborz in north central Iran, the trend of anisotropy changes to NE-SW with no obvious relation to the GPS vectors (Fig. 8c) or surface geology. In the longer period range of 25-60 s (corresponding to the lower crust and the uppermost mantle) the strength of anisotropy significantly increases over the

entire Plateau and a more coherent pattern is established. The N-S direction of anisotropy of the Arabian Plate in the southwest gradually changes to a NE-SW direction in the Zagros and eastern Iran, and then to a more E-W direction in the northern part of the Plateau and the region beyond in the Turan Platform. The major exception to this overall trend is the Lorestan Arc, where the anisotropic directions remain in the NW-SE orientation throughout the entire thickness of the crust and into the uppermost mantle. Interestingly, the Lorestan Arc has the lowest V_s lower crust throughout the Zagros. The rigid continental blocks making up the interior of central Iran (Lut and Great Kavir) exhibit little measurable anisotropy throughout the crust, which correlates well with their low level of seismicity and internal deformation. The Makran Subduction Zone is the only tectonic region that shows very weak anisotropy for periods sensitive to crustal depths. This result is surprising since one would expect to see measurable anisotropy in a highly-deforming accretionary wedge and an actively-subducting slab.

The additional data on the anisotropic structure in the uppermost mantle of Iran comes from the *Pn* tomography. The *Pn* anisotropy maps by Lu et al. (2012) and Al-Lazki et al. (2014), who both used catalog arrival times, show a highly-variable field and in many places uncorrelated with surface geology. Our anisotropy maps at 40-60 s, comparable to the *Pn* maps, although much smoother and more uniform, show little correspondence with the boundaries of the major tectonic domains of Iran. There are some major differences between our map and the *Pn* maps. For example, the *Pn* anisotropy does not show the same overall NE-SW trend dominant over the Plateau. Also, in the South Caspian, the *Pn* anisotropy shows a N-S orientation at least in its eastern part, whereas our map shows a dominant E-W trend. Lu et al. (2012) attributed this pattern to a frozen anisotropy inherited from the previous N-S spreading of the oceanic lithosphere of the South Caspian. In contrast, our anisotropy map shows an E-W trend in the South Caspian as part of a larger regional pattern. Our alternative interpretation is that the sub-Moho anisotropy of the SCB correlates with the Absolute Plate Motion (APM) vectors (Kreemer et al., 2014) (Fig. 8c), and is under the influence of the present-day mantle flow field. There are also regions where the surface wave and the *Pn*-wave show similar anisotropic patterns; both show low level of anisotropy in the rigid blocks of central Iran, and in the Makran Subduction Zone. The study by Lu et al. (2012) shows insignificant *Pn* anisotropy, which is in accordance with our results. However, the study by Al-Lazki et al. (2014) shows strong anisotropy around the subduction zone and in the eastern part of the Arabian Peninsula, although the amplitudes are unrealistically high.

A final word can be said about the vertical variation of anisotropy in different parts of Iran. The pattern of surface wave anisotropic orientations at the longest periods (50-70 s) as described above is in agreement with the APM vectors in the Middle East region (Kreemer et al., 2014) (Fig. 8c). Given that the lithosphere beneath Iran is rarely thinner than 100 km (e.g., Priestley et al., 2012), the Rayleigh waves between 50 and 70 s sample the lithospheric structure in the

Iranian Plateau. On the other hand, the APM vectors represent the large-scale asthenospheric flow field under the tectonic plates. A strong correlation between the fast directions of Rayleigh wave sampling the Iranian lithosphere and the APM vectors could suggest a coherent anisotropic structure between the mantle lithosphere and the sub-lithospheric medium. The picture in the Iranian Plateau, however, is more complex as significant anisotropy can be frozen in the lithosphere.

The SKS fast directions calculated over the Plateau show variable patterns (Kaviani et al., 2009; Sadeghi-Bagherabadi et al., 2018; Kaviani et al., 2021; Arvin et al., 2021; Gao et al., 2022). Beneath the NW Iran and western Alborz where the lithosphere is not very thick, the SKS fast axes broadly trend NE-SW, subparallel with APM vetores (Sadeghi-Bagherabadi et al., 2018; Kaviani et al., 2021; Arvin et al., 2021). Over vast regions in central, eastern, and northeastern Iran, the SKS fast directions show complex and variable patterns, in many places unrelated to APM vectors (Kaviani et al., 2021; Gao et al., 2022), and in the Zagros they change from range-parallel to range-perpendicular over short distances (Priestley et al, 2012; Sadeghi-Bagherabadi et al., 2018; Kaviani et al., 2020). Because of these complexities, there is a debate as to whether the SKS directions are dominated by the deformation of the mantle lithosphere or the shear flow in the asthenosphere. In this regard, the relative uniformity of the Rayleigh wave anisotropy at subcrustal depths observed in our model and the fact that it fits so well with the APM vectors is puzzling. A comparison of surface wave anisotropy with the SKS measurements reveals that in many places the crust, the mantle lithosphere, and the sub-lithosphere do not form a coherent set of layers. For example, in the eastern Kopet Dag, the SKS fast directions are parallel to the strike of the range (Gao et al., 2022) which suggests that they are controlled by the deformation of the deeper part of the lithosphere. On the other hand, our results show that the anisotropy of the shallower mantle is perpendicular to the range. This suggests that the mantle lithosphere of the Kopet Dag does not act coherently throughout its depth. In contrast, in the NW Zagros and western Kopet Dag, the direction of anisotropy remains unchanged for the entire depth of crust and also at subcrustal depths. This indicates that the crust and mantle of these two mountain ranges deform coherently.

Interestingly, Sadeghi-Bagherabadi et al. (2018) calculated range-parallel SKS fast orientations in the NW Zagros, and they attributed their observed anisotropy to the deformation of the mantle part of a very thick lithosphere in that section of the Zagros. Therefore, it may be that the entire lithosphere of the NW Zagros deforms coherently, although its pattern might be different from other parts of the range. The same thing cannot be said about the Alborz Mountains and the SCB. In the western Alborz, the orientation of anisotropy changes from NW-SE at shallow depths to NE-SW near the crust-mantle boundary. In the mantle lithosphere and the sub-lithosphere, the rocks have a consistent NE-SW oriented anisotropy throughout, as the agreement between the SKS directions (Arvin et al., 2021) and the Rayleigh wave directions suggest. Likewise, the SCB also has a variable fabric of deformation inside its

crust since a significant variation of anisotropy with depth is observed.

5 Conclusions

We present a 3D V_s model of the crust and uppermost mantle for the Iranian Plateau derived from the joint inversion of fundamental mode Rayleigh wave group velocities in the period range 5-70 s and P receiver functions. The presented model has the advantage of being derived from a large datasets of dispersion measurements from both ambient noise and earthquakes and receiver functions. As a result, the shear-wave velocity model reveals more structural details for the region compared to the previous studies. The main conclusions are as follows:

1) The short-period dispersion curves constrain the upper crustal structure. The low-V_s anomalies of the shallow upper crust represent regions of thick sediment across the Iranian Plateau. The SFB, the Zagros Foreland, and the Makran Accretionary Wedge together form extensive zones of thick sedimentary basins reaching to more than 20 km thick in some regions. The SCB is also a very deep sedimentary basin exceeding 20 km. The inland basins of central Iran, such as the Lut Block, the Jazmurian Depression, the Great Kavir, the northern part of SSZ-UDMA, and the region including the eastern Alborz and Kopet Dag Mountains are characterized by low velocities to ~10 km depth.

2) Based on the rapid change in the shear-wave velocity at the crust-mantle transition boundary, we built a higher resolution Moho depth map for the Iranian Plateau. There are strong correlations between the variations of topography, crustal thickness, Bouguer gravity anomaly, and the distribution of the major fault systems across the Iranian Plateau. The regions of low deformation such as central Iran and the Lut Block, have a crustal thickness mostly less than 45 km which is typical of normal continental crust (Laske et al., 2013). The regions of younger and active deformation such as the Makran Subduction Wedge and the SFB of Zagros have crustal thickness values 30-40 and 40-45 km, respectively. In contrast, the collisional belts of the High Zagros, SSZ-UDMA, Talesh-Alborz-Binalud, and Kopet Dag Mountains have a thicker crust (>55 km). The thickest crust beneath the SSZ reaches ~65 km depth.

3) The shear-wave velocity cross-sections traversing different parts of the Zagros collision (from the Kirkuk Zone in the NW to the Zagros-Makran transition zone in the SE) reveal a clear tongue-shaped low-V_s structure, suggesting that the Arabian crust is underthrusting central Iran. The angle of the underthrusting Arabian crust in the central Zagros is steeper than that below the Lorestan Arc, resulting in a narrower (~150 km width) deformation zone but thicker crust (~60-65 km depth) in the central SSZ as opposed to a wider (~250 km) deformation zone but somewhat thinner crust (~55-60 km) beneath the northwestern SSZ.

4) The stable lithospheric regions of the Arabian and Turan Platforms on the opposite sides of the collision zone show the highest V_s values (>4.8 km s^{-1}) in the uppermost mantle, but the sub-Moho V_s of the deforming lithosphere of the Iranian Plateau is mostly less than 4.3 km s^{-1}, similar to the Anatolian Plateau

(Koulakov, 2011). The low-V_s mantle of the Makran Volcanic Belt, and the northern end of the Sistan Suture Zone coincide with a potential lithospheric partial melting (Wu et al., 2021; Priestley et al., 2022), while the low-velocity zones in the western Alborz Mountains may originate from mantle delamination (Rastgoo et al., 2018).

5) In the upper crustal level, the Rayleigh wave azimuthal anisotropy is fairly weak and limited to a few regions in the NW Zagros and north-central Iran. At lower-crustal and sub-crustal depths azimuthal anisotropy significantly increases over the Plateau, except in the Makran Subduction Zone. The sub-crustal anisotropy is in broad agreement with the absolute plate motion vectors, suggesting that the lithosphere-asthenosphere mantle of the Plateau might have a coherent anisotropic structure. Comparison between the depth variations of Rayleigh wave anisotropy with the SKS splitting measurements over different regions of the Plateau reveals however, that the true situation is more complicated. In the NW Zagros, it appears that the entire lithosphere deforms coherently. In other regions such as the western Alborz and Kopet Dag Mountains, the evidence does not support a coherent deformational fabric throughout the depth of the lithosphere.

Data and software availability

The Rayleigh wave dispersion curves and P receiver functions data can be downloaded at https://data.mendeley.com/datasets/9xzgrgbsr4/1. Data analysis was performed primarily using Seismic Analysis Code (http://ds.iris.edu/ds/nodes/dmc/forms/sac/) (Goldstein et al., 2003) and Computer programs in seismology (http://www.eas.slu.edu/eqc/eqccps.html) (Herrmann, 2013), and plots were made using the Generic Mapping Tools (https://www.generic-mapping-tools.org/) (Wessel et al., 2019).

Acknowledgements

We would like to thank Mohammad Tatar and Ali Moradi for seismic recordings from the INSN and IRSC seismic networks, respectively, and Esmaeil Shabanian for helpful discussions. This research was supported by several IASBS internal grants, and the following NERC grants to Cambridge: NERC (Grant Ref: NE/J019895/1), IOF award NE/M017559/1, and RG73719–IAA award NE/L012936/1. MAI is grateful to the Bullard Laboratories, Department of Earth Sciences, University of Cambridge for a one year visit and computational facilities.

References

Abbassi, A., Nasrabadi, A., Tatar, M., Yaminifard, F., Abbassi, M. R., Hatzfeld, D., & Priestley, K. (2010). Crustal velocity structure in the southern edge of the Central Alborz (Iran). *Journal of Geodynamics*, *49*(2), 68-78. doi:10.1016/j.jog.2009.09.044

Abdetedal, M., Shomali, Z. H., & Gheitanchi, M. R. (2015). Ambient noise surface wave tomography of the Makran subduction zone, south-east Iran: Impli-

cations for crustal and uppermost mantle structures. *Earthquake Science*, *28*(4), 235-251. doi:10.1007/s11589-015-0132-1

Abdollahi, S., Ardestani, V. E., Zeyen, H., & Shomali, Z. H. (2018). Crustal and upper mantle structures of Makran subduction zone, SE Iran by combined surface wave velocity analysis and gravity modeling. *Tectonophysics*, *747*, 191-210. doi:10.1016/j.tecto.2018.10.005

Abdollahi, S., Zeyen, H., Ardestani, V. E., & Shomali, Z. H. (2019). 3D joint inversion of gravity data and Rayleigh wave group velocities to resolve shear-wave velocity and density structure in the Makran subduction zone, south-east Iran. *Journal of Asian Earth Sciences*, *173*, 275-290. doi:10.1016/j.jseaes.2019.01.029

Abdulnaby, W., Motaghi, K., Shabanian, E., Mahdi, H., Al-Shukri, H., & Gök, R. (2020). Crustal structure of the Mesopotamian Plain, east of Iraq. *Tectonics*, *39*(11), e2020TC006225. doi:10.1029/2020TC006225

Aflaki, M., Mousavi, Z., Ghods, A., Shabanian, E., Vajedian, S., & Akbarzadeh, M. (2019). The 2017 M w 6 Sefid Sang earthquake and its implication for the geodynamics of NE Iran. *Geophysical Journal International*, *218*(2), 1227-1245. doi:10.1093/gji/ggz172

Afshar-Harb, A., (1979). The stratigraphy, tectonics and petroleum geology of the Kopet Dagh region, northeastern Iran, *PhD thesis*, *Petroleum Geology Section, Royal School of Mines,* Imperial College of Science and Technology, London.

Agard, P., Omrani, J., Jolivet, L., Whitechurch, H., Vrielynck, B., Spakman, W., et al. (2011). Zagros orogeny: a subduction-dominated process. *Geological Magazine*, *148*(5-6), 692-725. doi:10.1017/S001675681100046X

Alavi, M. (1980). Tectonostratigraphic evolution of the Zagrosides of Iran. *Geology*, *8*(3), 144-149. doi:10.1130/0091-7613(1980)8%3C144:TEOTZO%3E2.0.CO;2

Alavi, M. (1992). Thrust tectonics of the Binalood region, NE Iran. *Tectonics*, *11*(2), 360-370. doi:10.1029/91TC02217

Alavi, M. (2007). Structures of the Zagros fold-thrust belt in Iran, *American Journal of Science*, *307*(9), 1064–1095. doi:10.2475/09.2007.02

Al-Lazki, A. I., Al-Damegh, K. S., El-Hadidy, S. Y., Ghods, A., & Tatar, M. (2014). Pn-velocity structure beneath Arabia–Eurasia Zagros collision and Makran subduction zones. *Geological Society, London, Special Publications*, *392*(1), 45-60. doi:10.1144/SP392.3

Allen, M. B., Ghassemi, M. R., Shahrabi, M., & Qorashi, M. (2003). Accommodation of late Cenozoic oblique shortening in the Alborz range, northern Iran. *Journal of structural geology*, *25*(5), 659-672. doi:10.1016/S0191-8141(02)00064-0

Ambraseys, N. N., & Melville, C. P. (2005). *A history of Persian earthquakes*. Cambridge university press.

Angiboust, S., Agard, P., De Hoog, J. C. M., Omrani, J., & Plunder, A. (2013). Insights on deep, accretionary subduction processes from the Sistan ophiolitic "mélange"(Eastern Iran). *Lithos*, *156*, 139-158. doi:10.1016/j.lithos.2012.11.007

Arvin, M., Pan, Y., Dargahi, S., Malekizadeh, A., & Babaei, A. (2007). Petrochemistry of the Siah-Kuh granitoid stock southwest of Kerman, Iran: Implications for initiation of Neotethys subduction. *Journal of Asian Earth Sciences*, *30*(3-4), 474-489. doi:10.1016/j.jseaes.2007.01.001

Arvin, S., Sobouti, F., Priestley, K., Ghods, A., Motaghi, K., Tilmann, F., & Eken, T. (2021). Seismic anisotropy and mantle deformation in NW Iran inferred from splitting measurements of SK (K) S and direct S phases. *Geophysical Journal International*, *226*(2), 1417-1431. doi:10.1093/gji/ggab181

Aziz Zanjani, A., Ghods, A., Sobouti, F., Bergman, E., Mortezanejad, G., Priestley, K., et al. (2013). Seismicity in the western coast of the South Caspian Basin and the Talesh Mountains. *Geophysical Journal International*, *195*(2), 799-814. doi:10.1093/gji/ggt299

Ballato, P., Uba, C. E., Landgraf, A., Strecker, M. R., Sudo, M., Stockli, D. F., et al. (2011). Arabia-Eurasia continental collision: Insights from late Tertiary foreland-basin evolution in the Alborz Mountains, northern Iran. *Bulletin*, *123*(1-2), 106-131. doi:10.1130/B30091.1

Baniadam, F., Shabanian, E., & Bellier, O. (2019). The kinematics of the Dasht-e Bayaz earthquake fault during Pliocene-Quaternary: implications for the tectonics of eastern Central Iran. *Tectonophysics*, *772*, 228218. doi:10.1016/j.tecto.2019.228218

Bavali, K., Motaghi, K., Sobouti, F., Ghods, A., Abbasi, M., Priestley, K., Mortezanejad, G., & Rezaeian, M. (2016). Lithospheric structure beneath NW Iran using regional and teleseismic travel-time tomography. *Physics of the Earth and Planetary Interiors*, *253*, 97-107. doi:10.1016/j.pepi.2016.02.006

Bayer, R., Chery, J., Tatar, M., Vernant, P., Abbassi, M., Masson, F., et al. (2006). Active deformation in Zagros—Makran transition zone inferred from GPS measurements. *Geophysical Journal International*, *165*(1), 373-381. doi:10.1111/j.1365-246X.2006.02879.x

Bensen, G. D., Ritzwoller, M. H., Barmin, M. P., Levshin, A. L., Lin, F., Moschetti, M. P., et al. (2007). Processing seismic ambient noise data to obtain reliable broad-band surface wave dispersion measurements. *Geophysical journal international*, *169*(3), 1239-1260. doi:10.1111/j.1365-246X.2007.03374.x

Berberian, M. (1981). Active faulting and tectonics of Iran, *Zagros Hindu Kush Himalaya Geodynamic Evolution*, *3*, 33–69. doi:10.1029/GD003p0033

Berberian, M. (1983). The southern Caspian: a compressional depression

floored by a trapped, modified oceanic crust, *Canadian Journal of Earth Sciences*, *20*(2), 163–183. doi:10.1139/e83-015

Berberian, M., & King, G. (1981). Towards a paleogeography and tectonic evolution of Iran, *Canadian journal of earth sciences*, *18*(2), 210–265. doi:10.1139/e81-019

Berberian, M., & Yeats, R. S. (1999). Patterns of historical earthquake rupture in the Iranian Plateau, *Bulletin of the Seismological society of America*, *89*(1), 120–139. doi:10.1785/BSSA0890010120

Berberian, M., Jackson, J. A., Qorashi, M., Khatib, M. M., Priestley, K., Talebian, M., & Ghafuri-Ashtiani, M. (1999). The 1997 May 10 Zirkuh (Qa'enat) earthquake (M w 7.2): faulting along the Sistan suture zone of eastern Iran. *Geophysical Journal International*, *136*(3), 671-694. doi:10.1046/j.1365-246x.1999.00762.x

Berberian, M., Qorashi, M., Jackson, J. A., Priestley, K., & Wallace, T. (1992). The Rudbar-Tarom earthquake of 20 June 1990 in NW Persia: preliminary field and seismological observations, and its tectonic significance. *Bulletin of the Seismological Society of America*, *82*(4), 1726-1755. doi:10.1785/BSSA0820041726

Besse, J., Torcq, F., Gallet, Y., Ricou, L. E., Krystyn, L., & Saidi, A. (1998). Late Permian to Late Triassic palaeomagnetic data from Iran: constraints on the migration of the Iranian block through the Tethyan Ocean and initial destruction of Pangaea. *Geophysical Journal International*, *135*(1), 77-92. doi:10.1046/j.1365-246X.1998.00603.x

Blanc, E. P., Allen, M. B., Inger, S., & Hassani, H. (2003). Structural styles in the Zagros simple folded zone, Iran. *Journal of the Geological Society*, *160*(3), 401-412. doi:10.1144/0016-764902-110

Brunet, M. F., Korotaev, M. V., Ershov, A. V., & Nikishin, A. M. (2003). The South Caspian Basin: a review of its evolution from subsidence modelling. *Sedimentary geology*, *156*(1-4), 119-148. doi:10.1016/S0037-0738(02)00285-3

Burdick, L. J., & Langston, C. A. (1977). Modeling crustal structure through the use of converted phases in teleseismic body-wave forms. *Bulletin of the Seismological Society of America*, *67*(3), 677-691. doi:10.1785/BSSA0670030677

Burg, J. (2018). Geology of the onshore Makran accretionary wedge: Synthesis and tectonic interpretation, *Earth-Science Reviews*, *185*, 1210-1231. doi:10.1016/j.earscirev.2018.09.011

Byrne, D. E., Sykes, L. R., & Davis, D. M. (1992). Great thrust earthquakes and aseismic slip along the plate boundary of the Makran subduction zone. *Journal of Geophysical Research: Solid Earth*, *97*(B1), 449-478. doi:10.1029/91JB02165

Chai, C., Ammon, C. J., Maceira, M., & Herrmann, R. B. (2015). Inverting interpolated receiver functions with surface wave dispersion and gravity:

Application to the western US and adjacent Canada and Mexico. *Geophysical Research Letters*, *42*(11), 4359-4366. doi:10.1002/2015GL063733

Cochran, J. R. (2005). Northern Red Sea: Nucleation of an oceanic spreading center within a continental rift, *Geochemistry, Geophysics, Geosystems*, *6*(3). doi:10.1029/2004GC000826

Colman-Sadd, S. P. (1978). Fold Development in Zagros Simply Folded Belt, Southwest Iran. *AAPG. Bulletin*, *62*, 984-1003. doi:10.1306/C1EA4F81-16C9-11D7-8645000102C1865D

Dashti, F., Lucente, F. P., Motaghi, K., Bianchi, I., Najafi, M., Govoni, A., & Shabanian, E. (2020). Crustal Scale Imaging of the Arabia-Central Iran Collision Boundary Across the Zagros Suture Zone, West of Iran. *Geophysical Research Letters*, *47*(8), e2019GL085921. doi:10.1029/2019GL085921

Debayle, E., & Sambridge, M. (2004). Inversion of massive surface wave data sets: Model construction and resolution assessment. *Journal of Geophysical Research: Solid Earth*, *109*(B2). doi:10.1029/2003JB002652

Dehghani, G. A., & Makris, J. (1984). The gravity field and crustal structure of Iran. *Neues Jahrbuch für Geologie und Paläontologie-Abhandlungen*, 215-229. doi:10.1127/njgpa/168/1984/215

DeMets, C., Gordon, R. G., Argus, D. F., & Stein, S. (1990). Current plate motions. *Geophysical journal international*, *101*(2), 425-478. doi:10.1111/j.1365-246X.1990.tb06579.x

Dewey, J. W., & Grantz, A. (1973). The Ghir earthquake of April 10, 1972 in the Zagros Mountains of southern Iran: seismotectonic aspects and some results of a field reconnaissance. *Bulletin of the Seismological Society of America*, *63*(6-1), 2071-2090. doi:10.1785/BSSA0636-12071

Djamour, Y., Vernant, P., Bayer, R., Nankali, H. R., Ritz, J. F., Hinderer, J., et al. (2010). GPS and gravity constraints on continental deformation in the Alborz mountain range, Iran. *Geophysical Journal International*, *183*(3), 1287-1301. doi:10.1111/j.1365-246X.2010.04811.x

Dziewonski, A., Bloch, S., & Landisman, M. (1969). A technique for the analysis of transient seismic signals. *Bulletin of the seismological Society of America*, *59*(1), 427-444. doi:10.1785/BSSA0590010427

Emami, H., Vergés, J., Nalpas, T., Gillespie, P., Sharp, I., Karpuz, R., Blanc, E. P., & Goodarzi, M. G. H. (2010). Structure of the Mountain Front Flexure along the Anaran anticline in the Pusht-e Kuh Arc (NW Zagros, Iran): insights from sand box models. *Geological Society, London, Special Publications*, *330*(1), 155-178. doi:10.1144/SP330.9

Engdahl, E. R., Jackson, J. A., Myers, S. C., Bergman, E. A., & Priestley, K. (2006). Relocation and assessment of seismicity in the Iran region. *Geophysical Journal International*, *167*(2), 761-778. doi:10.1111/j.1365-246X.2006.03127.x

Entezar-Saadat, V., Motavalli-Anbaran, S. H., & Zeyen, H. (2017). Lithospheric structure of the Eastern Iranian plateau from integrated geophysical modeling: a transect from Makran to the Turan platform. *Journal of Asian Earth Sciences*, *138*, 357-366. doi:10.1016/j.jseaes.2017.02.024

Eshagh, M., Tenzer, R., & Eshagh, M. (2020). Elastic thickness of the Iranian lithosphere from gravity and seismic data. *Tectonophysics*, *774*, 228186. doi:10.1016/j.tecto.2019.228186

Falcon, N. (1961). Major earth-flexuring in the Zagros Mountains of southwest Iran, *Quarterly Journal of the Geological Society*, *117*(1-4), 367–376. doi:10.1144/gsjgs.117.1.0367

Falcon, N. (1967). The geology of the north-east margin of the Arabian basement shield, *Advancement of Science*, *24*, 31–42.

Farhoudi, G., & Karig, D. E. (1977). Makran of Iran and Pakistan as an active arc system. *Geology*, *5*(11), 664-668. doi:10.1130/0091-7613(1977)5%3C664:MOIAPA%3E2.0.CO;2

Fotoohi Rad, G. R., Droop, G. T., Amini, S., & Moazzen, M. (2005). Eclogites and blueschists of the Sistan Suture Zone, eastern Iran: a comparison of P–T histories from a subduction mélange. *Lithos*, *84*(1-2), 1-24. doi:10.1016/j.lithos.2005.01.007

Gao, Y., Chen, L., Talebian, M., Wu, Z., Wang, X., Lan, H., et al. (2022). Nature and structural heterogeneities of the lithosphere control the continental deformation in the northeastern and eastern Iranian plateau as revealed by shear-wave splitting observations. *Earth and Planetary Science Letters*, *578*, 117284. doi:10.1016/j.epsl.2021.117284

Gholamzadeh, A., Yamini-Fard, F., Hessami, K., & Tatar, M. (2009). The February 28, 2006 Tiab earthquake, Mw 6.0: implications for tectonics of the transition between the Zagros continental collision and the Makran subduction zone. *Journal of Geodynamics*, *47*(5), 280-287. doi:10.1016/j.jog.2009.01.005

Gilligan, A., & Priestley, K. (2018). Lateral variations in the crustal structure of the Indo–Eurasian collision zone, *Geophysical Journal International*, *214*(2), 975–989. doi:10.1093/gji/ggy172

Goldstein, P., Dodge, D., Firpo, M., Minner, L., Lee, W. H. K., Kanamori, H., Jennings, P. C., & Kisslinger, C. (2003). SAC2000: Signal processing and analysis tools for seismologists and engineers. *The IASPEI international handbook of earthquake and engineering seismology*, *81*, 1613-1620.

Gök, R., Mahdi, H., Al-Shukri, H., & Rodgers, A. J. (2008). Crustal structure of Iraq from receiver functions and surface wave dispersion: implications for understanding the deformation history of the Arabian–Eurasian collision. *Geophysical Journal International*, *172*(3), 1179-1187. doi:10.1111/j.1365-246X.2007.03670.x

Guest, B., Stockli, D. F., Grove, M., Axen, G. J., Lam, P. S., & Hassanzadeh, J. (2006). Thermal histories from the central Alborz Mountains, northern Iran: implications for the spatial and temporal distribution of deformation in northern Iran. *Geological Society of America Bulletin*, *118*(11-12), 1507-1521. doi:10.1130/B25819.1

Haberland, C., Mokhtari, M., Babaei, H. A., Ryberg, T., Masoodi, M., Partabian, A., & Lauterjung, J. (2021). Anatomy of a crustal-scale accretionary complex: Insights from deep seismic sounding of the onshore western Makran subduction zone, Iran. *Geology*, *49*(1), 3-7. doi:10.1130/G47700.1

Hatzfeld, D., Tatar, M., Priestley, K., & Ghafory-Ashtiany, M. (2003). Seismological constraints on the crustal structure beneath the Zagros Mountain belt (Iran). *Geophysical Journal International*, *155*(2), 403-410. doi:10.1046/j.1365-246X.2003.02045.x

Herrmann, R. B. (2013). Computer programs in seismology: An evolving tool for instruction and research, *Seismological Research Letters*, *84*(6), 1081–1088. doi:10.1785/0220110096

Hessami, K., Pantosti, D., Tabassi, H., Shabanian, E., Abbassi, M. R., Feghhi, K., & Solaymani, S. (2003). Paleoearthquakes and slip rates of the North Tabriz Fault, NW Iran: preliminary results. *Annals of Geophysics*, *46*(5).

Hollingsworth, J., Jackson, J., Walker, R., Reza Gheitanchi, M., & Javad Bolourchi, M. (2006). Strike-slip faulting, rotation, and along-strike elongation in the Kopeh Dagh mountains, NE Iran. *Geophysical Journal International*, *166*(3), 1161-1177. doi:10.1111/j.1365-246X.2006.02983.x

Hollingsworth, J., Jackson, J., Walker, R., & Nazari, H. (2008). Extrusion tectonics and subduction in the eastern South Caspian region since 10 Ma. *Geology*, *36*(10), 763-766. doi:10.1130/G25008A.1

Hollingsworth, J., Nazari, H., Ritz, J. F., Salamati, R., Talebian, M., Bahroudi, A., et al. (2010a). Active tectonics of the east Alborz mountains, NE Iran: Rupture of the left-lateral Astaneh fault system during the great 856 AD Qumis earthquake. *Journal of Geophysical Research: Solid Earth*, *115*(B12). doi:10.1029/2009JB007185

Hollingsworth, J., Fattahi, M., Walker, R., Talebian, M., Bahroudi, A., Bolourchi, M. J., et al. (2010b). Oroclinal bending, distributed thrust and strike-slip faulting, and the accommodation of Arabia–Eurasia convergence in NE Iran since the Oligocene. *Geophysical Journal International*, *181*(3), 1214-1246. doi:10.1111/j.1365-246X.2010.04591.x

Horton, B. K., Hassanzadeh, J., Stockli, D. F., Axen, G. J., Gillis, R. J., Guest, B., et al. (2008). Detrital zircon provenance of Neoproterozoic to Cenozoic deposits in Iran: Implications for chronostratigraphy and collisional tectonics. *Tectonophysics*, *451*(1-4), 97-122. doi:10.1016/j.tecto.2007.11.063

Irandoust, M. A., Sobouti, F., & Rahimi, H. (2016). Lateral and depth variations of coda Q in the Zagros region of Iran. *Journal of Seismology*, *20*(1), 197-211. doi:10.1007/s10950-015-9520-1

Jackson, J. (1980). Errors in focal depth determination and the depth of seismicity in Iran and Turkey. *Geophysical Journal International*, *61*(2), 285-301. doi:10.1111/j.1365-246X.1980.tb04318.x

Jackson, J., & Fitch, T. (1981). Basement faulting and the focal depths of the larger earthquakes in the Zagros mountains (Iran), *Geophysical Journal International*, *64*(3), 561–586. doi:10.1111/j.1365-246X.1981.tb02685.x

Jackson, J., & McKenzie, D. (1984). Active tectonics of the Alpine—Himalayan Belt between western Turkey and Pakistan, *Geophysical Journal International*, *77*(1), 185–264. doi:10.1111/j.1365-246X.1984.tb01931.x

Jackson, J., & McKenzie, D. (1988). The relationship between plate motions and seismic moment tensors, and the rates of active deformation in the Mediterranean and Middle East, *Geophysical Journal International*, *93*(1), 45–73. doi:10.1111/j.1365-246X.1988.tb01387.x

Jackson, J., Haines, J., & Holt, W. (1995). The accommodation of Arabia-Eurasia plate convergence in Iran. *Journal of Geophysical Research: Solid Earth*, *100*(B8), 15205-15219. doi:10.1029/95JB01294

Jackson, J., Priestley, K., Allen, M., & Berberian, M. (2002). Active tectonics of the south Caspian basin. *Geophysical Journal International*, *148*(2), 214-245. doi:10.1046/j.1365-246X.2002.01588.x

Jentzer, M., Fournier, M., Agard, P., Omrani, J., Khatib, M. M., & Whitechurch, H. (2017). Neogene to Present paleostress field in Eastern Iran (Sistan belt) and implications for regional geodynamics. *Tectonics*, *36*(2), 321-339. doi:10.1002/2016TC004275

Karasözen, E., Nissen, E., Bergman, E. A., & Ghods, A. (2019). Seismotectonics of the Zagros (Iran) from orogen-wide, calibrated earthquake relocations. *Journal of Geophysical Research: Solid Earth*, *124*(8), 9109-9129. doi:10.1029/2019JB017336

Kaviani, A., Hatzfeld, D., Paul, A., Tatar, M., & Priestley, K. (2009). Shear-wave splitting, lithospheric anisotropy, and mantle deformation beneath the Arabia–Eurasia collision zone in Iran. *Earth and Planetary Science Letters*, *286*(3-4), 371-378. doi:10.1016/j.epsl.2009.07.003

Kaviani, A., Paul, A., Moradi, A., Mai, P. M., Pilia, S., Boschi, L., et al. (2020). Crustal and uppermost mantle shear wave velocity structure beneath the Middle East from surface wave tomography. *Geophysical Journal International*, *221*(2), 1349-1365. doi:10.1093/gji/ggaa075

Kaviani, A., Mahmoodabadi, M., Rümpker, G., Pilia, S., Tatar, M., Nilfouroushan, F., et al. (2021). Mantle-flow diversion beneath the Iranian

plateau induced by Zagros' lithospheric keel. *Scientific reports*, *11*(1), 1-12. doi:10.1038/s41598-021-81541-9

Kennett, B. L., Engdahl, E. R., & Buland, R. (1995). Constraints on seismic velocities in the Earth from traveltimes. *Geophysical Journal International*, *122*(1), 108-124. doi:10.1111/j.1365-246X.1995.tb03540.x

Khorrami, F., Vernant, P., Masson, F., Nilfouroushan, F., Mousavi, Z., Nankali, H., et al. (2019). An up-to-date crustal deformation map of Iran using integrated campaign-mode and permanent GPS velocities. *Geophysical Journal International*, *217*(2), 832-843. doi:10.1093/gji/ggz045

Kopp, C., Fruehn, J., Flueh, E. R., Reichert, C., Kukowski, N., Bialas, J., & Klaeschen, D. (2000). Structure of the Makran subduction zone from wide-angle and reflection seismic data. *Tectonophysics*, *329*(1-4), 171-191. doi:10.1016/S0040-1951(00)00195-5

Koulakov, I. (2011). High-frequency P and S velocity anomalies in the upper mantle beneath Asia from inversion of worldwide traveltime data. *Journal of Geophysical Research: Solid Earth*, *116*(B4). doi:10.1029/2010JB007938

Kreemer, C., Blewitt, G., & Klein, E. C. (2014). A geodetic plate motion and Global Strain Rate Model. *Geochemistry, Geophysics, Geosystems*, *15*(10), 3849-3889. doi:10.1002/2014GC005407

Langston, C. A. (1977). The effect of planar dipping structure on source and receiver responses for constant ray parameter. *Bulletin of the Seismological Society of America*, *67*(4), 1029-1050. doi:10.1785/BSSA0670041029

Laske, G., Masters, G., Ma, Z., & Pasyanos, M. (2013, April). Update on CRUST1. 0—A 1-degree global model of Earth's crust. In *Geophysical research abstracts* (Vol. 15, No. 15, p. 2658). Vienna, Austria: EGU General Assembly.

Ligorría, J. P., & Ammon, C. J. (1999). Iterative deconvolution and receiver-function estimation. *Bulletin of the seismological Society of America*, *89*(5), 1395-1400. doi:10.1785/BSSA0890051395

Lü, Y., Liu, B., Pei, S., Sun, Y., Toksöz, M. N., & Zeng, X. (2012). Pn tomographic velocity and anisotropy beneath the Iran region. *Bulletin of the Seismological Society of America*, *102*(1), 426-435. doi:10.1785/0120100141

Lyberis, N., Manby, G., Poli, J. T., Kalougin, V., Yousouphocaev, H., & Ashirov, T. (1998). Post-Triassic evolution of the southern margin of the Turan plate. *Comptes Rendus de l'Académie des Sciences-Series IIA-Earth and Planetary Science*, *326*(2), 137-143. doi:10.1016/S1251-8050(97)87458-7

Lyberis, N., & Manby, G. (1999). Oblique to orthogonal convergence across the Turan block in the post-Miocene. *AAPG bulletin*, *83*(7), 1135-1160. doi:10.1306/E4FD2E97-1732-11D7-8645000102C1865D

Maggi, A., & Priestley, K. (2005). Surface waveform tomography of the Turkish–Iranian plateau, *Geophysical Journal International*, *160*(3), 1068–1080.

doi:10.1111/j.1365-246X.2005.02505.x

Maggi, A., Jackson, J. A., Priestley, K., & Baker, C. (2000). A re-assessment of focal depth distributions in southern Iran, the Tien Shan and northern India: Do earthquakes really occur in the continental mantle?. *Geophysical Journal International*, *143*(3), 629-661. doi:10.1046/j.1365-246X.2000.00254.x

Mahmoodabadi, M., Yaminifard, F., Tatar, M., Kaviani, A., & Motaghi, K. (2019). Upper-mantle velocity structure beneath the Zagros collision zone, Central Iran and Alborz from nonlinear teleseismic tomography. *Geophysical Journal International*, *218*(1), 414-428. doi:10.1093/gji/ggz160

Mahmoodabadi, M., Yaminifard, F., Tatar, M., & Kaviani, A. (2020). Shear wave velocity structure of the upper-mantle beneath the northern Zagros collision zone revealed by nonlinear teleseismic tomography and Bayesian Monte-Carlo joint inversion of surface wave dispersion and teleseismic P-wave coda. *Physics of the Earth and Planetary Interiors*, *300*, 106444. doi:10.1016/j.pepi.2020.106444

Martinez, F., & Cochran, J. R. (1988). Structure and tectonics of the northern Red Sea: catching a continental margin between rifting and drifting, *Tectonophysics*, *150*(1-2), 1–31. doi:10.1016/0040-1951(88)90293-4

Masson, F., Anvari, M., Djamour, Y., Walpersdorf, A., Tavakoli, F., Daignieres, M., et al. (2007). Large-scale velocity field and strain tensor in Iran inferred from GPS measurements: new insight for the present-day deformation pattern within NE Iran. *Geophysical Journal International*, *170*(1), 436-440. doi:10.1111/j.1365-246X.2007.03477.x

Masson, F., Chéry, J., Hatzfeld, D., Martinod, J., Vernant, P., Tavakoli, F., & Ghafory-Ashtiani, M. (2005). Seismic versus aseismic deformation in Iran inferred from earthquakes and geodetic data. *Geophysical Journal International*, *160*(1), 217-226. doi:10.1111/j.1365-246X.2004.02465.x

Masson, F., Djamour, Y., Van Gorp, S., Chéry, J., Tatar, M., Tavakoli, F., et al. (2006). Extension in NW Iran driven by the motion of the South Caspian Basin. *Earth and Planetary Science Letters*, *252*(1-2), 180-188. doi:10.1016/j.epsl.2006.09.038

Mattei, M., Cifelli, F., Alimohammadian, H., Rashid, H., Winkler, A., & Sagnotti, L. (2017). Oroclinal bending in the Alborz Mountains (Northern Iran): New constraints on the age of South Caspian subduction and extrusion tectonics. *Gondwana Research*, *42*, 13-28. doi:10.1016/j.gr.2016.10.003

Mattei, M., Cifelli, F., Muttoni, G., Zanchi, A., Berra, F., Mossavvari, F., & Eshraghi, S. A. (2012). Neogene block rotation in central Iran: Evidence from paleomagnetic data. *Bulletin*, *124*(5-6), 943-956. doi:10.1130/B30479.1

McCall, G. J. H. (1997). The geotectonic history of the Makran and adjacent areas of southern Iran. *Journal of Asian Earth Sciences*, *15*(6), 517-531. doi:10.1016/S0743-9547(97)00032-9

McCall, G. J. H., & Kidd, R. G. W. (1982). The Makran, Southeastern Iran: the anatomy of a convergent plate margin active from Cretaceous to Present. *Geological Society, London, Special Publications*, *10*(1), 387-397. doi:10.1144/GSL.SP.1982.010.01.26

McElhinny, M. W., Embleton, B. J. J., Ma, X. H., & Zhang, Z. K. (1981). Fragmentation of Asia in the Permian. *Nature*, *293*(5829), 212-216. doi:10.1038/293212a0

McQuarrie, N., Stock, J. M., Verdel, C., & Wernicke, B. P. (2003). Cenozoic evolution of Neotethys and implications for the causes of plate motions. *Geophysical research letters*, *30*(20). doi:10.1029/2003GL017992

McQuarrie, N., & van Hinsbergen, D. J. (2013). Retrodeforming the Arabia-Eurasia collision zone: Age of collision versus magnitude of continental subduction. *Geology*, *41*(3), 315-318. doi:10.1130/G33591.1

Mohajjel, M., Fergusson, C. L., & Sahandi, M. R. (2003). Cretaceous–Tertiary convergence and continental collision, Sanandaj–Sirjan zone, western Iran. *Journal of Asian Earth Sciences*, *21*(4), 397-412. doi:10.1016/S1367-9120(02)00035-4

Mohammadi, E., Sodoudi, F., Kind, R., & Rezapour, M. (2013a). Presence of a layered lithosphere beneath the Zagros collision zone. *Tectonophysics*, *608*, 366-375. doi:10.1016/j.tecto.2013.09.017

Mohammadi, N., Sodoudi, F., Mohammadi, E., & Sadidkhouy, A. (2013b). New constraints on lithospheric thickness of the Iranian plateau using converted waves. *Journal of seismology*, *17*(3), 883-895. doi:10.1007/s10950-013-9359-2

Molinaro, M., Guezou, J. C., Leturmy, P., Eshraghi, S. A., & de Lamotte, D. F. (2004). The origin of changes in structural style across the Bandar Abbas syntaxis, SE Zagros (Iran). *Marine and Petroleum Geology*, *21*(6), 735-752. doi:10.1016/j.marpetgeo.2004.04.001

Monsef, I., Monsef, R., Mata, J., Zhang, Z., Pirouz, M., Rezaeian, M., et al. (2018). Evidence for an early-MORB to fore-arc evolution within the Zagros suture zone: Constraints from zircon U-Pb geochronology and geochemistry of the Neyriz ophiolite (South Iran). *Gondwana Research*, *62*, 287-305. doi:10.1016/j.gr.2018.03.002

Monsef, I., Rahgoshay, M., Pirouz, M., Chiaradia, M., Grégoire, M., & Ceuleneer, G. (2019). The Eastern Makran Ophiolite (SE Iran): evidence for a Late Cretaceous fore-arc oceanic crust. *International Geology Review*, *61*(11), 1313-1339. doi:10.1080/00206814.2018.1507764

Montagner, J. P. (1986). Regional three-dimensional structures using long-period surface waves. *Ann. Geophys*, *4*(B3), 283-294.

Morley, C. K., Kongwung, B., Julapour, A. A., Abdolghafourian, M., Hajian, M., Waples, D., et al. (2009). Structural development of a major late Cenozoic

basin and transpressional belt in central Iran: The Central Basin in the Qom-Saveh area. *Geosphere*, *5*(4), 325-362. doi:10.1130/GES00223.1

Mortezanejad, G., Rahimi, H., Romanelli, F., & Panza, G. F. (2019). Lateral variation of crust and upper mantle structures in NW Iran derived from surface wave analysis. *Journal of Seismology*, *23*(1), 77-108. doi:10.1007/s10950-018-9794-1

Motaghi, K., Tatar, M., & Priestley, K. (2012). Crustal thickness variation across the northeast Iran continental collision zone from teleseismic converted waves. *Journal of Seismology*, *16*(2), 253-260. doi:10.1007/s10950-011-9267-2

Motaghi, K., Tatar, M., Priestley, K., Romanelli, F., Doglioni, C., & Panza, G. F. (2015). The deep structure of the Iranian Plateau, *Gondwana Research, 28*(1), 407–418. doi:10.1016/j.gr.2014.04.009

Motaghi, K., Shabanian, E., & Kalvandi, F. (2017). Underplating along the northern portion of the Zagros suture zone, Iran. *Geophysical Journal International*, *210*(1), 375-389. doi:10.1093/gji/ggx168

Motaghi, K., Ghods, A., Sobouti, F., Shabanian, E., Mahmoudabadi, M., & Priestley, K. (2018). Lithospheric seismic structure of the West Alborz–Talesh ranges, Iran. *Geophysical Journal International*, *215*(3), 1766-1780. doi:10.1093/gji/ggy372

Motaghi, K., Shabanian, E., & Nozad-Khalil, T. (2020). Deep structure of the western coast of the Makran subduction zone, SE Iran. *Tectonophysics*, *776*, 228314. doi:10.1016/j.tecto.2019.228314

Mousavi, N., & Ebbing, J. (2018). Basement characterization and crustal structure beneath the Arabia–Eurasia collision (Iran): a combined gravity and magnetic study. *Tectonophysics*, *731*, 155-171. doi:10.1016/j.tecto.2018.03.018

Mousavi, Z., Walpersdorf, A., Walker, R. T., Tavakoli, F., Pathier, E., Nankali, H. R. E. A., et al. (2013). Global Positioning System constraints on the active tectonics of NE Iran and the South Caspian region. *Earth and Planetary Science Letters*, *377*, 287-298. doi:10.1016/j.epsl.2013.07.007

Mouthereau, F., Tensi, J., Bellahsen, N., Lacombe, O., De Boisgrollier, T., & Kargar, S. (2007). Tertiary sequence of deformation in a thin-skinned/thick-skinned collision belt: The Zagros Folded Belt (Fars, Iran). *Tectonics*, *26*(5). doi:10.1029/2007TC002098

Nemati, M., Hatzfeld, D., Gheitanchi, M. R., Sadidkhouy, A., & Mirzaei, N. (2011). Microseismicity and seismotectonics of the Firuzkuh and Astaneh faults (East Alborz, Iran). *Tectonophysics*, *506*(1-4), 11-21. doi:10.1016/j.tecto.2011.04.007

Niazi, M., Shimamura, H., & Matsu'ura, M. (1980). Microearthquakes and crustal structure off the Makran coast of Iran. *Geophysical Research Letters*, *7*(5), 297-300. doi:10.1029/GL007i005p00297

Nissen, E., Tatar, M., Jackson, J. A., & Allen, M. B. (2011). New views on earthquake faulting in the Zagros fold-and-thrust belt of Iran. *Geophysical Journal International*, *186*(3), 928-944. doi:10.1111/j.1365-246X.2011.05119.x

Nissen, E., Jackson, J., Jahani, S., & Tatar, M. (2014). Zagros "phantom earthquakes" reassessed—The interplay of seismicity and deep salt flow in the Simply Folded Belt?. *Journal of Geophysical Research: Solid Earth*, *119*(4), 3561-3583. doi:10.1002/2013JB010796

Omar, G. I., & Steckler, M. S. (1995). Fission track evidence on the initial rifting of the Red Sea: two pulses, no propagation, *Science*, *270*(5240), 1341–1344. doi:10.1126/science.270.5240.1341

Paul, A., Kaviani, A., Hatzfeld, D., Vergne, J., & Mokhtari, M. (2006). Seismological evidence for crustal-scale thrusting in the Zagros mountain belt (Iran). *Geophysical Journal International*, *166*(1), 227-237. doi:10.1111/j.1365-246X.2006.02920.x

Paul, A., Hatzfeld, D., Kaviani, A., Tatar, M., & Péquegnat, C. (2010). Seismic imaging of the lithospheric structure of the Zagros mountain belt (Iran). *Geological Society, London, Special Publications*, *330*(1), 5-18. doi:10.1144/SP330.2

Penney, C., Tavakoli, F., Saadat, A., Nankali, H. R., Sedighi, M., Khorrami, F., et al. (2017). Megathrust and accretionary wedge properties and behaviour in the Makran subduction zone. *Geophysical Journal International*, *209*(3), 1800-1830. doi:10.1093/gji/ggx126

Phinney, R. A. (1964). Structure of the Earth's crust from spectral behavior of long-period body waves. *Journal of Geophysical Research*, *69*(14), 2997-3017. doi:10.1029/JZ069i014p02997

Pirouz, M., Avouac, J. P., Hassanzadeh, J., Kirschvink, J. L., & Bahroudi, A. (2017). Early Neogene foreland of the Zagros, implications for the initial closure of the Neo-Tethys and kinematics of crustal shortening. *Earth and Planetary Science Letters*, *477*, 168-182. doi:10.1016/j.epsl.2017.07.046

Priestley, K., Baker, C., & Jackson, J. (1994). Implications of earthquake focal mechanism data for the active tectonics of the South Caspian Basin and surrounding regions. *Geophysical Journal International*, *118*(1), 111-141. doi:10.1111/j.1365-246X.1994.tb04679.x

Priestley, K., McKenzie, D., Barron, J., Tatar, M., & Debayle, E. (2012). The Zagros core: deformation of the continental lithospheric mantle. *Geochemistry, Geophysics, Geosystems*, *13*(11). doi:10.1029/2012GC004435

Priestley, K., Sobouti, F., Mokhtarzadeh, R., A Irandoust, M., Ghods, R., Motaghi, K., & Ho, T. (2022). New Constraints for the On-Shore Makran Subduction Zone Crustal Structure. *Journal of Geophysical Research: Solid Earth*, *127*(1), e2021JB022942. doi:10.1029/2021JB022942

Radjaee, A., Rham, D., Mokhtari, M., Tatar, M., Priestley, K., & Hatzfeld,

D. (2010). Variation of Moho depth in the central part of the Alborz Mountains, northern Iran. *Geophysical Journal International*, *181*(1), 173-184. doi:10.1111/j.1365-246X.2010.04518.x

Rahimi, H., Hamzehloo, H., Vaccari, F., & Panza, G. F. (2014). Shear-Wave Velocity Tomography of the Lithosphere–Asthenosphere System beneath the Iranian PlateauShear-Wave Velocity Tomography of Lithosphere–Asthenosphere System. *Bulletin of the Seismological Society of America*, *104*(6), 2782-2798. doi:10.1785/0120130319

Rahmani, M., Motaghi, K., Ghods, A., Sobouti, F., Talebian, M., Ai, Y., & Chen, L. (2019). Deep velocity image of the north Zagros collision zone (Iran) from regional and teleseismic tomography. *Geophysical Journal International*, *219*(3), 1729-1740. doi:10.1093/gji/ggz393

Rastgoo, M., Rahimi, H., Motaghi, K., Shabanian, E., Romanelli, F., & Panza, G. F. (2018). Deep structure of the Alborz Mountains by joint inversion of P receiver functions and dispersion curves. *Physics of the Earth and Planetary Interiors*, *277*, 70-80. doi:10.1016/j.pepi.2018.01.011

Regard, V., Bellier, O., Thomas, J. C., Abbassi, M. R., Mercier, J., Shabanian, E., et al. (2004). Accommodation of Arabia-Eurasia convergence in the Zagros-Makran transfer zone, SE Iran: A transition between collision and subduction through a young deforming system. *Tectonics*, *23*(4). doi:10.1029/2003TC001599

Reilinger, R., McClusky, S., Vernant, P., Lawrence, S., Ergintav, S., Cakmak, R., et al. (2006). GPS constraints on continental deformation in the Africa-Arabia-Eurasia continental collision zone and implications for the dynamics of plate interactions. *Journal of Geophysical Research: Solid Earth*, *111*(B5). doi:10.1029/2005JB004051

Robert, A. M., Letouzey, J., Kavoosi, M. A., Sherkati, S., Müller, C., Vergés, J., & Aghababaei, A. (2014). Structural evolution of the Kopeh Dagh fold-and-thrust belt (NE Iran) and interactions with the South Caspian Sea Basin and Amu Darya Basin. *Marine and Petroleum Geology*, *57*, 68-87. doi:10.1016/j.marpetgeo.2014.05.002

Robertson, A. H. (2000). Mesozoic-Tertiary tectonic-sedimentary evolution of a south Tethyan oceanic basin and its margins in southern Turkey. *Geological Society, London, Special Publications*, *173*(1), 97-138. doi:10.1144/GSL.SP.2000.173.01.05

Sadeghi-Bagherabadi, A., Sobouti, F., Ghods, A., Motaghi, K., Talebian, M., Chen, L., et al. (2018). Upper mantle anisotropy and deformation beneath the major thrust-and-fold belts of Zagros and Alborz and the Iranian Plateau. *Geophysical Journal International*, *214*(3), 1913-1918. doi:10.1093/gji/ggy233

Salaün, G., Pedersen, H. A., Paul, A., Farra, V., Karabulut, H., Hatzfeld, D., et al. (2012). High-resolution surface wave tomography beneath the Aegean-

Anatolia region: constraints on upper-mantle structure. *Geophysical Journal International*, *190*(1), 406-420. doi:10.1111/j.1365-246X.2012.05483.x

Sandvol, E., Seber, D., Barazangi, M., Vernon, F., Mellors, R., & Al-Amri, A. (1998). Lithospheric seismic velocity discontinuities beneath the Arabian Shield. *Geophysical Research Letters*, *25*(15), 2873-2876. doi:10.1029/98GL02214

Sattarzadeh, Y., Cosgrove, J. W., & Vita-Finzi, C. (1999). The interplay of faulting and folding during the evolution of the Zagros deformation belt. *Geological Society, London, Special Publications*, *169*(1), 187-196. doi:10.1144/GSL.SP.2000.169.01.14

Şengör, A. M. C., & Kidd, W. S. F. (1979). Post-collisional tectonics of the Turkish-Iranian plateau and a comparison with Tibet. *Tectonophysics*, *55*(3-4), 361-376.

Şengör, A. M. C., Yılmaz, Y., & Sungurlu, O. (1984). Tectonics of the Mediterranean Cimmerides: nature and evolution of the western termination of Palaeo-Tethys. *Geological Society, London, Special Publications*, *17*(1), 77-112. doi:10.1144/GSL.SP.1984.017.01.04

Shabanian, E., Bellier, O., Siame, L., Arnaud, N., Abbassi, M. R., & Cochemé, J. J. (2009). New tectonic configuration in NE Iran: Active strike-slip faulting between the Kopeh Dagh and Binalud mountains. *Tectonics*, *28*(5). doi:10.1029/2008TC002444

Shabanian, E., Bellier, O., Siame, L., Abbassi, M. R., Bourlès, D., Braucher, R., & Farbod, Y. (2012). The Binalud Mountains: A key piece for the geodynamic puzzle of NE Iran. *Tectonics*, *31*(6). doi:10.1029/2012TC003183

Shad Manaman, N., & Shomali, H. (2010). Upper mantle S-velocity structure and Moho depth variations across Zagros belt, Arabian–Eurasian plate boundary. *Physics of the Earth and Planetary Interiors*, *180*(1-2), 92-103. doi:10.1016/j.pepi.2010.01.011

Shad Manaman, N., Shomali, H., & Koyi, H. (2011). New constraints on upper-mantle S-velocity structure and crustal thickness of the Iranian plateau using partitioned waveform inversion. *Geophysical Journal International*, *184*(1), 247-267. doi:10.1111/j.1365-246X.2010.04822.x

Shahabpour, J. (2010). Tectonic implications of the geochemical data from the Makran igneous rocks in Iran. *Island Arc*, *19*(4), 676-689. doi:10.1111/j.1440-1738.2010.00723.x

Sherkati, S., Letouzey, J., & Frizon de Lamotte, D. (2006). Central Zagros fold-thrust belt (Iran): New insights from seismic data, field observation, and sandbox modeling. *Tectonics*, *25*(4). doi:10.1029/2004TC001766

Shoja-Taheri, J., & Niazi, M. (1981). Seismicity of the Iranian plateau and

bordering regions. *Bulletin of the Seismological Society of America*, *71*(2), 477-489. doi:10.1785/BSSA0710020477

Smith, M. L., & Dahlen, F. A. (1973). The azimuthal dependence of Love and Rayleigh wave propagation in a slightly anisotropic medium. *Journal of Geophysical Research*, *78*(17), 3321-3333. doi:10.1029/JB078i017p03321

Snyder, D. B., & Barazangi, M. (1986). Deep crustal structure and flexure of the Arabian plate beneath the Zagros collisional mountain belt as inferred from gravity observations. *Tectonics*, *5*(3), 361-373. doi:10.1029/TC005i003p00361

Sodoudi, F., Yuan, X., Kind, R., Heit, B., & Sadidkhouy, A. (2009). Evidence for a missing crustal root and a thin lithosphere beneath the Central Alborz by receiver function studies. *Geophysical Journal International*, *177*(2), 733-742. doi:10.1111/j.1365-246X.2009.04115.x

Soffel, H. C., & Förster, H. G. (1984). Polar wander path of the Central-East-Iran Microplate including new results. *Neues Jahrbuch für Geologie und Paläontologie-Abhandlungen*, 165-172. doi:10.1127/njgpa/168/1984/165

Stöcklin, J. (1968). Structural history and tectonics of Iran: a review, *AAPG bulletin*, *52*(7), 1229–1258. doi:10.1306/5D25C4A5-16C1-11D7-8645000102C1865D

Stöcklin, J. (1974). Possible ancient continental margins in Iran. In *The geology of continental margins* (pp. 873-887). Springer, Berlin, Heidelberg. doi:10.1007/978-3-662-01141-6_64

Stoneley, R. (1990). The Arabian continental margin in Iran during the Late Cretaceous. *Geological Society, London, Special Publications*, *49*(1), 787-795. doi:10.1144/GSL.SP.1992.049.01.48

Taghizadeh-Farahmand, F., Sodoudi, F., Afsari, N., & Ghassemi, M. R. (2010). Lithospheric structure of NW Iran from P and S receiver functions. *Journal of seismology*, *14*(4), 823-836. doi:10.1007/s10950-010-9199-2

Talebi, A., Koulakov, I., Moradi, A., Rahimi, H., & Gerya, T. (2020). Ongoing formation of felsic lower crustal channel by relamination in Zagros collision zone revealed from regional tomography. *Scientific reports*, *10*(1), 1-7. doi:10.1038/s41598-020-64946-w

Talebian, M., & Jackson, J. (2004). A reappraisal of earthquake focal mechanisms and active shortening in the Zagros mountains of Iran. *Geophysical Journal International*, *156*(3), 506-526. doi:10.1111/j.1365-246X.2004.02092.x

Tatar, M., & D. Hatzfeld (2009). Microseismic evidence of slip partitioning for the Rudbar-Tarom earthquake (Ms 7.7) of 1990 June 20 in NW Iran, *Geophysical Journal International*, *176*(2), 529–541. doi:10.1111/j.1365-246X.2008.03976.x

Tatar, M., Hatzfeld, D., Martinod, J., Walpersdorf, A., Ghafori-Ashtiany, M., & Chéry, J. (2002). The present-day deformation of the central Za-

gros from GPS measurements. *Geophysical research letters*, *29*(19), 33-1. doi:10.1029/2002GL015427

Tatar, M., Hatzfeld, D., & Ghafory-Ashtiany, M. (2004). Tectonics of the Central Zagros (Iran) deduced from microearthquake seismicity. *Geophysical Journal International*, *156*(2), 255-266. doi:10.1111/j.1365-246X.2003.02145.x

Tatar, M., Jackson, J., Hatzfeld, D., & Bergman, E. (2007). The 2004 May 28 Baladeh earthquake (M w 6.2) in the Alborz, Iran: overthrusting the South Caspian Basin margin, partitioning of oblique convergence and the seismic hazard of Tehran. *Geophysical Journal International*, *170*(1), 249-261. doi:10.1111/j.1365-246X.2007.03386.x

Tchalenko, J. S. (1975). Seismicity and structure of the Kopet Dagh (Iran, USSR). *Philosophical Transactions of the Royal Society of London. Series A, Mathematical and Physical Sciences*, *278*(1275), 1-28. doi:10.1098/rsta.1975.0019

Teknik, V., & Ghods, A. (2017). Depth of magnetic basement in Iran based on fractal spectral analysis of aeromagnetic data. *Geophysical Journal International*, *209*(3), 1878-1891. doi:10.1093/gji/ggx132

Tirrul, R., Bell, I. R., Griffis, R. J., & Camp, V. E. (1983). The Sistan suture zone of eastern Iran. *Geological Society of America Bulletin*, *94*(1), 134-150. doi:10.1130/0016-7606(1983)94%3C134:TSSZOE%3E2.0.CO;2

Van Avendonk, H. J., Holbrook, W. S., Lizarralde, D., & Denyer, P. (2011). Structure and serpentinization of the subducting Cocos plate offshore Nicaragua and Costa Rica. *Geochemistry, Geophysics, Geosystems*, *12*(6). doi:10.1029/2011gc003592

Veisi, M., Sobouti, F., Chevrot, S., Abbasi, M., & Shabanian, E. (2021). Upper mantle structure under the Zagros collision zone; insights from 3D teleseismic P-wave tomography. *Tectonophysics*, *819*, 229106. doi:10.1016/j.tecto.2021.229106

Vergés, J., Saura, E., Casciello, E., Fernandez, M., Villaseñor, A., Jimenez-Munt, I., & García-Castellanos, D. (2011). Crustal-scale cross-sections across the NW Zagros belt: implications for the Arabian margin reconstruction. *Geological Magazine*, *148*(5-6), 739-761. doi:10.1017/S0016756811000331

Vernant, P., Nilforoushan, F., Hatzfeld, D., Abbassi, M. R., Vigny, C., Masson, F., et al. (2004a). Present-day crustal deformation and plate kinematics in the Middle East constrained by GPS measurements in Iran and northern Oman. *Geophysical Journal International*, *157*(1), 381-398. doi:10.1111/j.1365-246X.2004.02222.x

Vernant, P., Nilforoushan, F., Chery, J., Bayer, R., Djamour, Y., Masson, F., et al. (2004b). Deciphering oblique shortening of central Alborz in Iran using geodetic data. *Earth and planetary science letters*, *223*(1-2), 177-185. doi:10.1016/j.epsl.2004.04.017

Walker, R., Jackson, J., & Baker, C. (2003). Surface expression of thrust faulting in eastern Iran: source parameters and surface deformation of the 1978 Tabas and 1968 Ferdows earthquake sequences. *Geophysical Journal International*, *152*(3), 749-765. doi:10.1046/j.1365-246X.2003.01886.x

Walker, R., Jackson, J., & Baker, C. (2004). Active faulting and seismicity of the Dasht-e-Bayaz region, eastern Iran. *Geophysical Journal International*, *157*(1), 265-282. doi:10.1111/j.1365-2966.2004.02179.x

Walpersdorf, A., Hatzfeld, D., Nankali, H., Tavakoli, F., Nilforoushan, F., Tatar, M., et al. (2006). Difference in the GPS deformation pattern of North and Central Zagros (Iran). *Geophysical Journal International*, *167*(3), 1077-1088. doi:10.1111/j.1365-246X.2006.03147.x

Walpersdorf, A., Manighetti, I., Mousavi, Z., Tavakoli, F., Vergnolle, M., Jadidi, A., et al. (2014). Present-day kinematics and fault slip rates in eastern Iran, derived from 11 years of GPS data. *Journal of Geophysical Research: Solid Earth*, *119*(2), 1359-1383. doi:10.1002/2013JB010620

Walters, R. J., Elliott, J. R., Li, Z., & Parsons, B. (2013). Rapid strain accumulation on the Ashkabad fault (Turkmenistan) from atmosphere-corrected InSAR. *Journal of Geophysical Research: Solid Earth*, *118*(7), 3674-3690. doi:10.1002/jgrb.50236

Wessel, P., Luis, J. F., Uieda, L., Scharroo, R., Wobbe, F., Smith, W. H., & Tian, D. (2019). The generic mapping tools version 6. *Geochemistry, Geophysics, Geosystems*, *20*(11), 5556-5564. doi:10.1029/2019gc008515

White, R. S., Louden, K. E. (1982). The Makran Continental Margin: Structure of a Thickly Sedimented Convergent Plate Boundary, *Studies in Continental Margin Geology, Watkinsand, J.S., Drake, C.L. (Eds.). Mem. Am. Ass. Petrol. Geol. 34*, 499–518.

Wimpenny, S., & Watson, C. S. (2021). gWFM: A Global Catalog of Moderate-Magnitude Earthquakes Studied Using Teleseismic Body Waves. *Seismological Research Letters*, *92*(1), 212-226. doi:10.1785/0220200218

Wu, Z., Chen, L., Talebian, M., Wang, X., Jiang, M., Ai, Y., et al. (2021). Lateral Structural Variation of the Lithosphere-Asthenosphere System in the Northeastern to Eastern Iranian Plateau and Its Tectonic Implications. *Journal of Geophysical Research: Solid Earth*, *126*(1), e2020JB020256. doi:10.1029/2020JB020256

Yamini-Fard, F., Hatzfeld, D., Farahbod, A. M., Paul, A., & Mokhtari, M. (2007). The diffuse transition between the Zagros continental collision and the Makran oceanic subduction (Iran): microearthquake seismicity and crustal structure. *Geophysical Journal International*, *170*(1), 182-194. doi:10.1002/jgrb.50236

Yamini-Fard, F., & Hatzfeld, D. (2008). Seismic structure beneath Zagros-Makran transition zone (Iran) from teleseismic study: seismological evidence for

underthrusting and buckling of the Arabian plate beneath central Iran. *Journal of Seismology and Earthquake Engineering*, *10*(1), 11-24.

Zingerle, P., Pail, R., Gruber, T., & Oikonomidou, X. (2020). The combined global gravity field model XGM2019e. *Journal of Geodesy*, *94*(7), 1-12. doi:10.1007/s00190-020-01398-0